

Novel type of biomedical titanium-manganese-niobium alloy fabricated by arc melting and metal injection moulding

Von der Fakultät für Maschinenbau, Elektro- und Energiesysteme
der Brandenburgischen Technischen Universität Cottbus–Senftenberg
zur Erlangung des akademischen Grades eines
Doktors der Ingenieurwissenschaften

genehmigte Dissertation

vorgelegt von

Haoyin Zhang

Geboren am 29. April 1989 in Henan, China

Vorsitzende: Prof. Dr. Markus Bambach

Gutachter: Prof. Dr. Florian Pyczak

Gutachter: Prof. Dr. Sabine Weiß

Tag der mündlichen Prüfung: 29. 01. 2020

Abstract

Titanium and its alloys have been widely used as implant biomaterials due to their suitable combination of mechanical properties and biological compatibilities. At present, about 70-80% of implants are made of metallic biomaterials. Compared with magnesium alloys, stainless steel and cobalt alloys, titanium alloys have a higher specific strength, high corrosion resistance, and excellent biocompatibility. With research, Ti-Nb biomedical titanium alloys have been constantly developed. In the Ti-Nb alloy, the amount of Nb is usually from 16% to 42% (wt.%) which is about 10% to 30% (at.%). As reported, Mn as a trace element to the human body has the potential to be used in bio-materials, moreover, the cost of Mn is much lower than Nb. Therefore, this study aims at the partial replacement of Nb by Mn to reduce the costs, without deteriorating the mechanical properties. Moreover, it must be ensured good biocompatibility and corrosion resistance. This is the first investigated on Ti-Mn-Nb ternary alloys.

In this work, the various compositions are prepared by arc melting for raw alloys production. Hereafter, to determine of the Ti-Mn-Nb phase equilibria at 900 °C. According to β single-phase field, Ti-xMn-yNb (x=4, 10, 16; y=2, 8, 14, at.%) alloys (arc-melted) after solution treatment (900 °C) have been fabricated. The Ti-Mn-Nb alloys are investigated by optical microscopy (OM), X-ray diffraction (XRD), hardness test, transmission electron microscopy (TEM) and mechanical testing. By screening study on alloy, Ti-10Mn-14Nb (at.%) (Ti-10Mn-23.7Nb (wt.%)) is the optimal alloy with tensile strength (760 MPa) and elongation (10.5%). After that, the Metal Injection Moulding (MIM) is used to prepare Ti-Mn-Nb alloys. Due to its net-shape advantage, the MIM method can greatly reduce the processing cost. MIM Ti-xMn-yNb (x=3, 4, 6; y=1, 2, 4, at.%), Ti-4Mn-14Nb and Ti-10Mn-14Nb alloys are fabricated. Among them, a very good combination of mechanical properties is achieved for MIM processed Ti-4Mn-2Nb (at.%) (Ti-4.5Mn-3.8Nb (wt.%)), namely a YS of 642 MPa, UTS of 725 MPa and high ductility of 16% elongation to fracture. With further investigations, when the yttrium content is 0.1% (at.%), the tensile strength of Ti-4Mn-2Nb-0.1Y (at.%) (Ti-4.5Mn-3.8Nb-0.18Y (wt.%)) is increased to 785 MPa while maintaining an elongation of 12.9%. These mechanical properties already exceed Ti-6Al-4V (ASTM F2885 Grade 5 undensified). Compared with the Ti-10Mn-14Nb alloy produced by arc melted, Ti-4Mn-2Nb-0.1Y (at.%) is greatly decreased the content of Mn and Nb.

In the in vitro evaluation, in comparison with MIM pure titanium, human osteoblasts MG63 adhered as well and proliferated on the surface of MIM Ti-Mn-Nb specimens. In the supernatant after cell culture, the Ti-Mn-Nb alloy shows similar osmolality and pH value results as MIM pure titanium. By LDH assay and DNA isolation, the MIM Ti-Mn-Nb alloys are not found to be toxic to MG63 cells.

In the study of corrosion resistance in Hanks' balanced salt solution (HBSS) at 37 °C, the corrosion current densities as well as the impedance of MIM Ti-Mn-Nb alloys are all better than those of MIM pure titanium and even better than those of MIM Ti-6Al-4V alloy.

Zusammenfassung

Titan und seine Legierungen werden aufgrund ihrer geeigneten Kombination von mechanischen Eigenschaften und biologischen Verträglichkeiten in großem Umfang als Implantat-Biomaterialien verwendet. Derzeit bestehen ca. 70-80% der Implantate aus metallischen Biomaterialien. Titanlegierungen haben im Vergleich zu Magnesiumlegierungen, Edelstahl- und Kobaltlegierungen eine höhere spezifische Festigkeit, eine hohe Korrosionsbeständigkeit und eine hervorragende Biokompatibilität. Im Laufe der Forschung wurden biomedizinische Ti-Nb-Legierungen laufend weiterentwickelt. Bei Ti-Nb-Legierungen beträgt der Anteil an Niob üblicherweise 16 bis 42 wt.%, was etwa 10 bis 30 at.% entspricht. Wie berichtet, ist Mangan ein wichtiges Spurenelement für den menschlichen Körper und eignet sich daher zu Verwendung in Biomaterialien. Darüber hinaus sind die Kosten für Mangan viel niedriger als für Niob. Daher zielt diese Studie auf den teilweisen Ersatz von Niob durch Mangan ab, um die Kosten zu senken, ohne die mechanischen Eigenschaften zu verschlechtern. Außerdem muss eine gute Biokompatibilität und Korrosionsbeständigkeit gewährleistet sein. Dies ist die erste Untersuchung an ternären Ti-Mn-Nb-Legierungen.

In dieser Arbeit werden die verschiedenen Zusammensetzungen durch Lichtbogenschmelzen hergestellt. Anschließend wird das Ti-Mn-Nb-Phasengleichgewicht bei 900 °C bestimmt. Gemäß β -Einphasenfeld wurden Ti-xMn-yNb ($x = 4, 10, 16$; $y = 2, 8, 14$ at.%) -Legierungen durch Erschmelzen im Lichtbogenofen und anschließendes Lösungsglühen (900 °C) hergestellt. Die Ti-Mn-Nb-Legierungen werden durch Lichtmikroskopie (OM), Röntgendiffraktometrie (XRD), Härteprüfung, Transmissionselektronenmikroskopie (TEM) und mechanische Prüfung (Zugversuch) untersucht. Durch Screening-Untersuchungen an einer Legierung wurde Ti-10Mn-14Nb (at.%) (Ti-10Mn-23.7Nb (wt.)) als optimale Legierung mit einer Zugfestigkeit von 760 MPa und einer Bruchdehnung von 10.5% ausgewählt. Anschließend werden im Metallpulverspritzguss (Metal Injection Molding, MIM) Proben aus Ti-Mn-Nb-Legierungen hergestellt. Da MIM ein endkonturnahes Fertigungsverfahren ist, kann das MIM-Verfahren die Verarbeitungskosten erheblich reduzieren. MIM-Ti-xMn-yNb ($x = 3, 4, 6$; $y = 1, 2, 4$ at%), Ti-4Mn-14Nb und Ti-10Mn-14Nb-Legierungen werden hergestellt. Die MIM-verarbeitete Legierung Ti-4Mn-2Nb (at.%) (Ti-4,5Mn-3,8Nb (wt.)) erreicht eine sehr gute Kombination der mechanischen Eigenschaften, nämlich eine Dehngrenze von 642 MPa, eine Zugfestigkeit von 725 MPa und eine Bruchdehnung von 16%. Durch Zugabe von 0,1% (at.%) Yttrium entsteht die Legierung Ti-4Mn-2Nb-0,1Y (at.%) (Ti-4,5Mn-3,8Nb-0,18Y (wt.)). Hierbei wird die Zugfestigkeit auf 785 MPa erhöht, während eine Bruchdehnung von 12,9% beibehalten wird. Diese mechanischen Eigenschaften übersteigen bereits die Mindestanforderungen für Ti-6Al-4V nach ASTM F2885 (Grade 5 unverdichtet). Verglichen mit der durch Lichtbogenschmelzen hergestellten Ti-10Mn-14Nb-Legierung ist der Gehalt an Mn und Nb bei Ti-4Mn-2Nb-0,1Y (at.%) stark verringert.

In der In-vitro-Evaluation hafteten im Vergleich zu MIM-Reintitan auch humane Osteoblasten MG63 an und vermehrten sich auf der Oberfläche von MIM-Ti-Mn-Nb-Proben. Im Überstand nach der Zellkultur zeigt die Ti-Mn-Nb-Legierung ähnliche Osmolalitäts- und pH-Werte wie MIM-Reintitan. Durch LDH-Tests und DNA-Isolierung wurde festgestellt, dass die MIM-Ti-Mn-Nb-Legierungen für MG63-Zellen nicht toxisch sind.

Bei der Untersuchung der Korrosionsbeständigkeit in Salzlösung nach Hanks (HBSS) bei 37 °C sind sowohl die Selbstkorrosionsstromdichte als auch die Impedanz von MIM-Ti-Mn-Nb-Legierungen besser als die von MIM-Reintitan und sogar besser als die der MIM Ti-6Al-4V-Legierung.

1. Introduction	1
2. State of the art	4
2.1 Ti and Ti alloys.....	4
2.1.1 Medical application of titanium alloy	5
2.1.2 Ti-Nb alloys.....	6
2.1.3 Ti-Mn alloys.....	7
2.2 Arc-melting method.....	9
2.3 Metal injection-moulding method.....	10
2.4 MIM Ti alloy for biomedical application	13
3. Motivation and objectives	16
4. Materials and Methods	17
4.1 Ti-Mn-Nb alloy produced by arc-melting.....	17
4.1.1 Selection of alloy composition	17
4.1.2 Feedstock of Ti-Mn-Nb alloy by arc melting	19
4.1.3 Material preparation by arc-melting and used facilities.....	20
4.2 Ti-Mn-Nb alloy processed by MIM.....	22
4.2.1 Feedstock of Ti-Mn-Nb alloy by MIM	22
4.2.2 Preparing materials by MIM	23
4.3 Characterization of the samples	25
4.3.1 Phase diagram determination	25
4.3.2 Heat-treatment process of arc-melting Ti-Mn-Nb samples.....	26
4.3.3 Metallography preparation.....	26
4.3.4 Impurity levels and relative density.....	27
4.3.5 OM analysis.....	27
4.3.6 SEM analysis.....	27
4.3.7 X-ray Diffraction	27
4.3.8 Young's modulus measurements.....	28
4.3.9 Vickers hardness measurement.....	29
4.3.10 Tension tests	29
4.3.10 TEM analysis.....	30
4.3.11 Cell biology assessment	31
4.3.12 Corrosion measurement	34
5. Results	35
5.1 Ti-Mn-Nb experimental ternary phase diagram	35
5.2 Characterization of Ti-Mn-Nb alloys	38

Contents

5.2.1 Microstructure	38
5.2.2 α/β phase fraction and average grain size of Ti-Mn-Nb alloys	43
5.2.3 Density and Young's modulus of Ti-Mn-Nb alloy processed by MIM	44
5.3 X-ray diffraction	45
5.4 Mechanical properties	48
5.4.1 Hardness	48
5.4.2 Tensile properties of samples fabricated by arc-melting	50
5.4.3 Tensile properties of samples fabricated by MIM	51
5.5 Fracture	54
5.6 Transmission electron microscopy	59
5.7 Cell biology assessment	62
5.7.1 Live/Dead staining	63
5.7.2 Osmolality and pH value	65
5.7.3 DNA isolation and LDH release	66
5.8 Corrosion behavior	68
5.8.1 Potentiodynamic polarization	68
5.8.2 Electrochemical impedance spectroscopy	72
6. Discussion	76
6.1 Determine suitable Ti-Mn-Nb alloy compositions by arc melting	76
6.2 Analysis of sintered alloys	82
6.2.1 Density	82
6.2.2 Young's modulus	83
6.3 The influence of Mn and Nb content on microstructure and mechanical properties of Ti-Mn-Nb alloys	84
6.3.1 The influence on α/β phase and average grain size	84
6.3.2 The influence of interstitial elements on MIM Ti-Mn-Nb alloys	86
6.3.3 TEM analysis	88
6.4 Enhancement of mechanical properties with Y element addition	88
6.5 Biocompatibility of Ti-Mn-Nb alloy fabricated by MIM	91
6.6 Corrosion behavior of samples fabricated by MIM	94
7. Summary and conclusions	97
References:	99
Abbreviations	112
Acknowledgement	114

1. Introduction

Titanium is a chemical element with the symbol Ti and atomic number 22. It is a lustrous transition metal with a silver color [1]. Titanium was discovered by British pastor William Gregor in 1791 and was later named by a German chemist Martin Heinrich Klaproth [2]. Titanium and its alloys have been widely used as implant biomaterials due to their suitable combination of mechanical properties and biological compatibilities. Owing to their excellent mechanical properties, biomedical metals have been extensively used in the clinic for hundreds of years [3]. At present, about 70-80 % of implants are made of metallic biomaterials [4]. Compared with stainless steel and cobalt chromium alloys, titanium alloys have higher specific strength (strength to density ratio), high corrosion resistance, and excellent biocompatibility [5]. Typical actual applications of titanium alloy in human body are shown below (Fig. 1-1).



Fig. 1-1. Application of titanium implants in the human body, (a) titanium mandible, (b) titanium dental implant, (c) titanium alloy one joint, (d) the 3D printed titanium alloy skull.

((a) www.3dnatives.com/en/best-3d-printed-implants-230720195/, (b) pureprotho.com/zirconia-dental-implants-or-titanium-implants-houston-prosthodontist-weighs-in/, (c) www.tsquality.it/it/progettazione-ed-engineering/, (d) www.machiningnews.com/2017/06/renishaw-presents-implant-technology-for-oral-and-maxillofacial-surgeons/)

1. Introduction

The first attempt to use Ti as an implant material dates back to late 1930s [4]. Among titanium alloys, pure Ti and Ti-6Al-4V (Ti64) were first investigated in view of their biocompatibility. However, the mechanical strength of pure Ti is not satisfying. Conversely, Ti64 has good mechanical properties, but in some studies Al ions and V ions which can be set free from the Ti64 alloy were found to have detrimental effects on the human body. However, the utilization of this alloy has been limited due to high raw material and manufacturing costs [6-8]. Thus, in view of the release of toxic Al and V ions [9], a new type of Ti alloy needs to be developed.

Hereafter, Ti-Nb-Ta and Ti-Nb-Ta-Zr alloys have been developed. They exhibit a young's modulus around 60 GPa and, simultaneously, a good balance between tensile strength and elongation [5]. Niobium, tantalum and zirconium exhibit great biocompatibility [10]. Nb and Ta elements are critical materials in terms of the limited amounts of their natural deposits. Thus, they may be difficult to acquire in the future [11-13].

Accordingly, the costs for Nb and Ta containing alloys will probably become very high making those alloys unsuitable for large scale use as medical materials. Thus, it is very important to develop a cheaper biomedical titanium alloy with good mechanical properties. One way is to add new, less expensive β -stabilizing elements replacing some amount of expensive Nb. This new β -stabilizing element must be also non-toxic to the human body.

Manganese is a eutectoid β -stabilizing element for titanium but it was reported that the eutectoid reaction is very sluggish in Mn containing alloys and can be considered as not taking place under normal processing conditions [14, 15]. It is highly available and of low cost. Furthermore, according to biological reports Mn plays a key role in osteogenesis and bone resorption mechanisms [16]. However, no research has focused on Ti-Mn-Nb ternary alloy, yet. In this study, Mn will partly replace the more expensive niobium.

A conventional method of preparing alloys is vacuum arc-melting. Because it is both time-consuming and expensive, a majority of commercial alloys do not employ the process. However, Nickel, titanium, and cobalt are materials most often processed with this method [17]. The melting point of pure titanium is 1668°C; meanwhile, titanium has high chemical activity and can react violently with oxygen and nitrogen at high temperatures [18]. Therefore, vacuum arc melting is one of the main preparation methods of titanium alloys. Because it is both time consuming and expensive [17], this leads to an increase in the processing cost of the titanium alloy. To investigate a more cost-effective method of titanium alloy production Metal injection moulding was used to prepare the titanium alloy.

Metal injection moulding (MIM) offers a net-shape or near net-shape fabrication for making complex shaped parts in large volumes [19]. The injection moulding process, well known from the processing of plastics, is exploited to form components with a very high degree of freedom with regard to geometry, without strongly influencing the production costs. Thus, bearing in mind medical implants, optimal functionality, e.g., by anatomical shape can be provided. Because of the need of a rather expensive mould an economic benefit is gained typically at a total number of parts around some thousands. Thus, implants like bone screws, bone plates, or dental implants could be good candidates for MIM manufacturing [20]. With the research and development continuing in the process of utilizing MIM, a new 3D printing preparation method is derived: fused filament fabrication (FFF). FFF has become an essential tool for the rapid fabrication of custom parts via additive manufacturing. Although there are numerous advantages of this technique, including ease of use, cost and flexibility, improving the strength of printed parts to rival that of traditionally-manufactured parts remains an underlying issue [21, 22].

2. State of the art

2. State of the art

2.1 Ti and Ti alloys

Titanium is a chemical element with the symbol Ti and atomic number 22 [1]. Titanium atom radius is 0.132 nm. Titanium was discovered by William Gregor in 1791 in Cornwall, Great Britain, and was named by Titans of Greek mythology. The element occurs within a number of mineral deposits, principally rutile and ilmenite, which are widely distributed in the Earth's crust and lithosphere, and it is found in almost all living things, water bodies, rocks, and soils [1, 2].

Titanium is a transition metal with atomic structure $1s^2, 2s^2, 2p^6, 3s^2, 3p^6, 3d^2,$ and $4s^2$. The $3d^2$ and $4s^2$ electrons are highly reactive and thus Titanium is a highly reactive element, causing a low standard electrode potential of $-1.63\text{ V}, \text{Ti} \rightarrow \text{Ti}^{2+} + 2e^-$ [23]. Oxygen has the highest affinity for titanium and reacts spontaneously with it at room temperature, creating an oxidized surface. Since this oxide layer is very dense at room temperature, further progress of the reaction is prevented, and therefore, titanium generally exhibits very stable oxidation properties.

The metallurgy of titanium is dominated by the crystallographic transformation, which means it has allotropism: the hexagonal close-packed (hcp) structure (α -phase) and body-centered cubic (bcc) structure (β -phase). The lattice constants of hcp α -phase are: $a=0.295\text{ nm}, c=0.468\text{ nm}, c/a=1.587$, and the one of bcc β -phase: $a=0.332\text{ nm}$. The crystal structures are shown in Fig. 2.1-1.

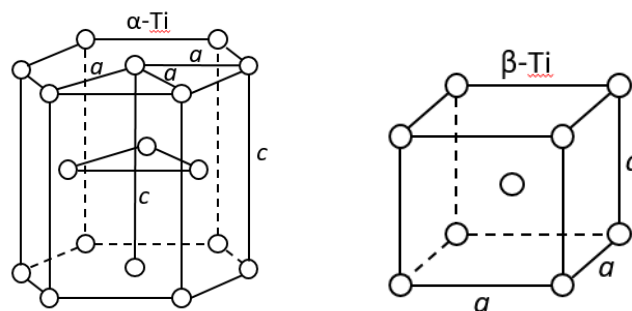


Fig. 2.1-1. Hexagonal close-packed (HCP) structure (α -phase) and body-centered cubic (BCC) structure (β -phase)

With temperature rising above $882\text{ }^\circ\text{C}$ which is the β transus temperature, titanium transforms into a body-centered cubic (b.c.c) structure (β -phase) [24]. With the addition of alloying elements, the properties of pure titanium can be changed to obtain a titanium alloy that meets the requirements. According to the influence of the element on the β transformation temperature, the elements in the

titanium alloy can be classified into neutral elements, α -stabilizing elements, and β -stabilizing elements. The α stabilizing element extends the α phase region to a higher temperature range, while the beta phase stabilizing element moves the beta phase region towards a lower temperature. The β -stabilizing element can be subdivided into β -isomorphs and β -eutectoid. Neutral elements have little effect on the beta transition temperature. Therefore, Ti alloys are classified into α , near α , $\alpha + \beta$, and near β or β according to their room temperature phase composition [25].

Fig. 2.1-2 shows typical phase diagrams influenced by alloying element. Examples for typical neutral elements are Sn and Zr. In addition to extending the α phase region to a higher temperature, the α -stabilizing element forms an $\alpha+\beta$ phase region. Al is an important α -stabilizing element. The interstitial elements oxygen, nitrogen, and carbon also belong to the α -stabilizing elements. The β -isomorphs elements have very high solubility in beta-titanium, such as Nb, Mo, V, and Ta. On the other hand, an intermetallic compound can be formed even if a very small amount of a β -eutectoid element is present. For example elements such as Mn, Fe, Cr, Co, Ni, Cu, and H, etc. are considered as β -eutectoid elements.

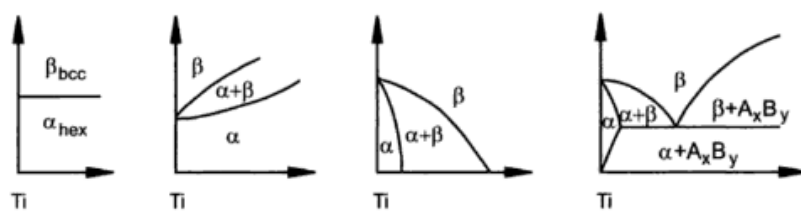


Fig. 2.1-2. Schematic phase diagrams showing the influence of alloying elements on phase constitution of Ti alloys [18], (From left to right: neutral element, α -stabilizing element, β -isomorphs element and β -eutectoid element)

2.1.1 Medical application of titanium alloy

In the early 1970s, commercially pure titanium opened new possibilities within clinical dentistry. Brånemark et al reported [26], on their clinical experiences with dental implants built upon fixtures of commercially pure titanium. The reason for this success stemmed from one property of titanium: its reactivity with oxygen, which makes it covered with an oxide layer that promotes tissue compatibility [26, 27]. The titanium alloys currently used most commercially are still pure titanium, Ti-Al-4V and also Ti-6Al-7Nb [28-30]. With the study of different alloying elements of titanium alloys, Nb, Ta and Zr are

2. State of the art

selected as the safest alloying elements [31-33]. In addition to those elements, Mn and Mo are selected as safer elements for human body [34, 35].

The titanium alloys reported recently as biomaterials are Ti-Ta-Zr system, Ti-Nb-Hf system, Ti-Nb-Zr system, Ti-Nb-Sn system, Ti-Nb-Ta-Zr system, Ti-Ta-Fe system, Ti-Mo-Zr-Sn system, Ti-Mo-Nb-Si system, Ti-Sn-Nb-Ta system [36-42]. Many of these alloys contain a fairly large amount of Nb, Ta, Zr, Mo and/or Sn. Meanwhile, a small amount of Mn was also considered to be a non-toxic element and has been added to develop biological titanium alloy [14, 34, 43-45].

2.1.2 Ti-Nb alloys

The English chemist Charles Hatchett reported a new element similar to tantalum in 1801 and named it columbium. The German chemist Heinrich Rose determined in 1846 that tantalum ores contain a second element, which he named niobium. Niobium, formerly known as columbium, is a chemical element with the symbol Nb (formerly Cb) and atomic number 41. Niobium's atom radius is 0.134 nm and it is a light grey transition metal. Pure Niobium has a similar hardness to that of pure titanium [46]. Nb has good biocompatibility and osteoconductivity [47]. The addition of Nb in Ti alloys also does not show a toxic effect on the cells [48-50]. Nb acts as an important β -phase stabilizer in Ti alloys. Fig. 2.1-3 presents the Ti-Nb binary phase diagram [51]. It can be found from the phase diagram that Nb belongs to the β -isomorphous element, which can be infinitely dissolved in β -Ti.

It has been reported that [52, 53], in reducing the elastic modulus, Nb added is more effective than the other β stabilizing element. With the continuous research, Ti-Nb-based biomedical titanium alloys have been constantly developed as Ti-Nb-Zr system, Ti-Nb-Ta-Zr system, Ti-Sn-Nb-Ta system and so on [54-56]. In the Ti-Nb-based alloy, the amount of Nb is usually from 16% to 42% (wt.%) which is about 10% to 30% (at.%). For instance, biomedical TNTZ alloy which is Ti-35Nb-5Ta-7Zr (wt.%) has been developed. After annealing, it exhibits UTS: 590MPa, YS:530 [57].

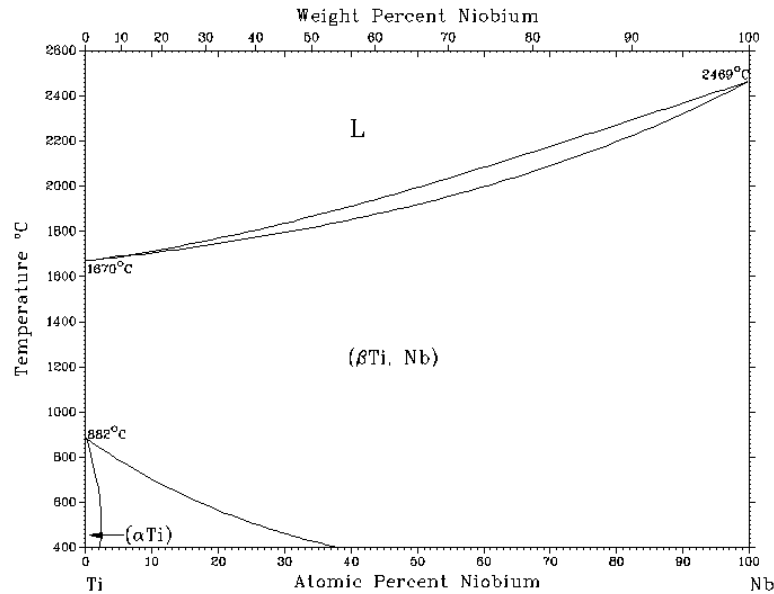


Fig. 2.1-3. Titanium-niobium phase diagram [51]

2.1.3 Ti-Mn alloys

Manganese is a chemical element with the symbol Mn and atomic number 25. Manganese atomic radius is 0.117 nm and it is not found as a free element in nature; it is often found in minerals in combination with iron. Manganese is a transition metal that is silvery-gray in color and resembles iron. It is hard and very brittle, but easy to oxidize [58]. Historically, manganese is named for pyrolusite and other black minerals from the region of Magnesia in Greece, which also gave its name to magnesium and the iron ore magnetite. By the mid-18th century, Swedish-German chemist Carl Wilhelm Scheele had used pyrolusite to produce chlorine. Johan Gottlieb Gahn was the first to isolate an impure sample of manganese metal in 1774 [59].

In biology, manganese ions function as cofactors for a large variety of enzymes with many functions [60]. Mn is an essential trace element in the human body [61], which plays an important role in the metabolic cycle of e.g. lipids, amino acids, and carbohydrates. It influences the immune system, bone growth, blood clotting, cellular energy regulation, and neurotransmitter synthesis [61]. It is also the scavenger of free radicals in the manganese superoxide dismutase [62]. The concentration of Mn should be <0.8 μg/L in blood serum [63]. The high concentrations may induce neurotoxicity [64]. The poisonous effect of Mn from Mg alloys on cell viability and proliferation has been observed.

2. State of the art

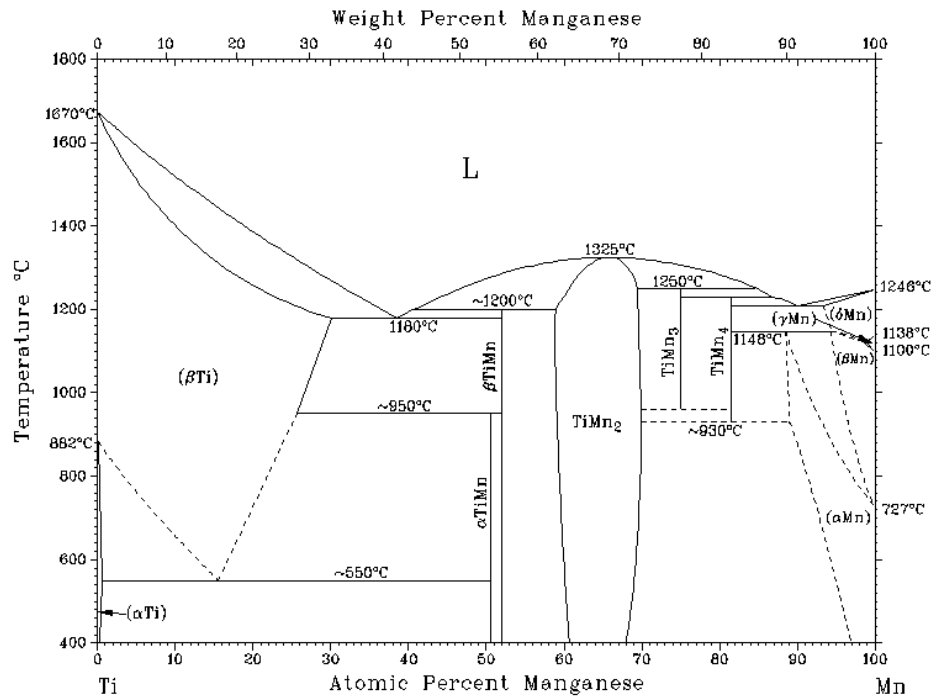


Fig. 2.1-4. Titanium-manganese phase diagram [65]

Mn acts as a β -eutectoid element of Ti alloy, as is obvious from the phase diagram [65] shown as Fig.2.1-4. A Ti-Mn binary alloy was developed as biomaterial. There was no significant bio toxicity found by preliminary in vitro tests. According to the report [44], biocompatibility of low-cost β -type Ti - (6% - 18%) Mn (wt.%) alloys were obtained after solution treatment by cold crucible levitation melting (CCLM). Ti-9Mn exhibits the best combination of tensile strength and elongation. Young's modulus of 94 GPa, UTS of 1048 MPa and elongation of 19% were achieved. Its performance is comparable or superior to those of Ti-6Al-4V ELI (Ti-64 ELI) in terms of every parameter evaluated.

There have been no reports on the Ti-Mn-Nb ternary alloy system. However, there are many kinds of research on the Ti-Nb binary alloys and Ti-Mn binary alloys. It reports the addition of Nb and Mn to Ti alloys as a strengthening element [66, 67]. The Ti alloys can be applied for structural materials or biomaterials. Each of these two elements has its own performances, as shown in Table 2.1-1.

Table 2.1-1. Performances of Mn and Nb element

Performance	Alloy element	
	Mn	Nb
Stability (20 °C)	-	++
Low melting point	++	-
Strength improvement (Ti alloy)	++	+
Biocompatibility	-/+*	+
Low-cost	++	--

* Depending on the different situation

As a more active metal element, Mn can react with oxygen in the air at room temperature and form MnO [68]. The melting point of Mn element is low. The Nb element as a high melting point element is relatively stable at room temperature. Both Mn and Nb belong to the β -stabilizing elements of Ti alloys. They can significantly increase the strength. Nb is known as non-toxic element that can be applied to biological materials. Usually, Mn is non-toxic and a trace element required by the human body, but the high-valence Mn is toxic, so it needs to be biologically evaluated. However, Nb (42,280 \$/ton) is more expensive than Mn (2,060 \$/ton) according to 2018 network data [69]. One of the advantages of Ti-Mn-Nb alloy is the use of Mn to reduce the Nb content and achieve cost reduction.

2.2 Arc-melting method

Arc melting is generally performed in a vacuum environment. Once initiated, a vacuum arc can persist, since the freed particles gain kinetic energy from the electric field, heating the metal surfaces through high-speed particle collisions. This process can create an incandescent cathode spot, which frees more particles, thereby sustaining the arc, producing a great amount of heat to melt metal. The schematic setup of an arc melting device is shown in the Fig. 2.2-1.

2. State of the art

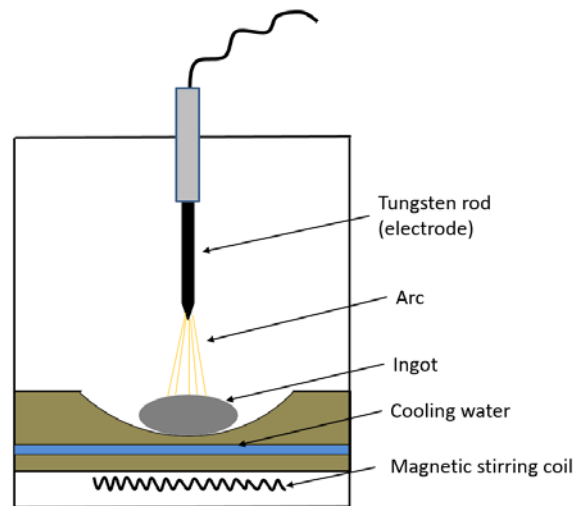


Fig. 2.2-1. Schematic of arc melting

Vacuum arc melting is used most frequently in high-value applications. Because it is both time-consuming and expensive, a majority of commercial alloys do not employ the process. Nickel, titanium, and specialty steels are materials most often processed with this method. Use of this technique over traditional methods presents several advantages:

1. Since it is melted in a closed environment, the alloy composition in the electric arc furnace is less influenced by evaporation of some elements, and the heating process is relatively easy to control.
2. Some high melting point metals can be melted, and the alloy composition is homogenized and segregation is eliminated, by electromagnetic stirring when the metal is liquefied.
3. The gases dissolved in liquid metal during melting metals in open furnaces, such as nitrogen, oxygen, chlorine and hydrogen are considered detrimental to the majority of titanium and other alloys. Under vacuum conditions, these gases escape from the liquid metal to the vacuum chamber.
4. Certain metals and alloys, such as Ti, cannot be melted in open-air furnaces.

2.3 Metal injection-moulding method

Attempts to use injection-moulding date back to the 1920s in the production of ceramic components. However, until 1979, the method had not received significant attention. Since the 1980s, this method has been applied to metal forming and is therefore called Metal Injection Moulding (MIM). MIM is considered as net-shape technology. It successfully combines the advantages of powder metallurgy and injection moulding.

However, even though the MIM process has been applied to Ti in numerous fields since the late 1980s, the production of Ti and Ti alloys by MIM is still a specialty in the field of MIM processing [70]. In addition, the high sensitivity of titanium alloys to O is a problem in the MIM process, which may result in highly brittle products [60]. With the continuous improvement of the powder process, the problem of high oxygen content has also been gradually solved. There are five key factors due to which MIM is advantageous for any application [71]:

1. Industrialized mass production with good repeatability and performance
2. The cost can be greatly reduced
3. Highly customized geometry
4. Flexible material components, even hard and brittle materials can be prepared.
5. Tight tolerances.

The MIM process requires four steps: mixing the raw materials, injection moulding, debinding and sintering. The process flow diagram is shown in Fig. 2.3-1.

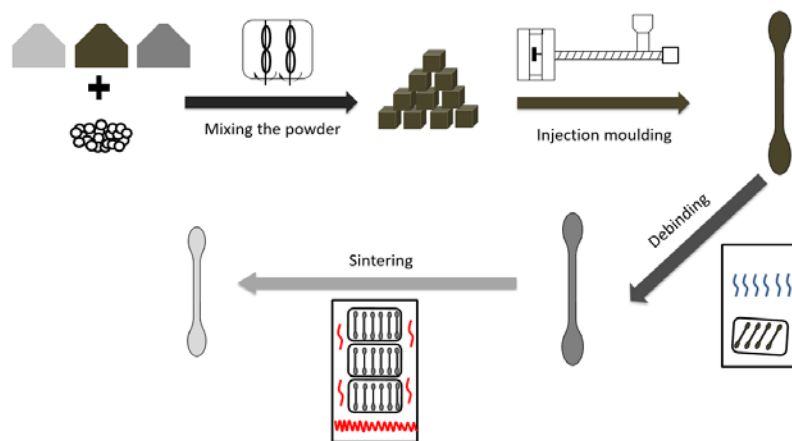


Fig. 2.3-1. Schematic diagram of the MIM processing steps

Mixing the powder

Feedstock in MIM method is metal powder and binder. Initial powder morphology and size have a strong influence on the final MIM product. In general, the spherical powder is advantageous for the

2. State of the art

fluidity of the raw material, increasing the packing density in the injection step. The smaller the particle size of the powder, the more likely it is to achieve ideal dense sintering [72].

The binder becomes a liquid after raising the temperature during the mixing process and has a certain fluidity so that the powder can be uniformly packaged at the time of compounding, and the desired size and shape can be obtained during the moulding process until the start of sintering. Before sintering, oxidation of the metal powder is well prevented by the presence of binder covering the surface of metal powder. In addition, adhesive compositions and debinding technology are the focus of many patents in the MIM process [73]. The binder usually consists of backbone and surfactant. Backbone phase providing strength is a filler polymer which can be easily removed in the first step of debinding (solvent debinding), and a surfactant, which is also a lubricant, to bridge between the binder and powder. The binders for MIM production are generally categorized into five types: thermoplastic compounds, thermosetting compounds, water-based systems, gelation systems and inorganics [74, 75].

Mixing at a temperature slightly higher than the melting point of the backbone polymer helps the binder to wrap on the powder. After mixing metal powder and binder, the feedstock has been prepared. The key features of an ideal feedstock include a low viscosity, no voids or pores, a high elasticity and high mixture homogeneity [76].

Injection moulding

The injection-moulded specimens are called “green specimens”. Injection moulding is usually carried out in conventional injection moulding machines. In metal injection processing, wear resistance, screw geometry, and injection control need to be considered. The rheological properties and the homogeneity of feedstock plays a key role during injection moulding [77]. The injection moulding parameters need to be adjusted to achieve the optimum moulding process: nozzle temperature, screw speed, injection volume, injection pressure, mould temperature, holding time and holding pressure [78].

Debinding

After the injection moulding process, the binder of “green specimens” should be removed by a series of physical and chemical processes, usually including chemical and thermal debinding. The chemical debinding is generally solvent debinding. Solvent debinding involves immersing the compact into a solvent to dissolve and remove at least one component of the binder system, leading to a structure

with open pores. These pores are equivalent in their shape to channels and are crucial for the subsequent thermal debinding. It is desired to completely remove the binder in solvent debinding. This would cause internal cracks and deformation, resulting in moulding failure [79]. The residual binder will be eliminated in the subsequent thermal degreasing.

The key aim of thermal debinding is to remove the residual binder under argon protective atmosphere. During thermal debinding, the evaporated or decomposed binder phases are transported to the surface through the “channels” which left at solvent debinding process.

Sintering

In MIM processing, sintering is the final step after debinding, which causes the inconsistent metal powder to become a dense metal [80]. On the microscopic scale, fine pores are eliminated during the sintering process. As the sintering temperature increases, solid-phase diffusion or solid-liquid diffusion occurs between the metal particles powders, and even liquid phase diffusion can occur, depending on the sintering temperature.

Through the study of the mechanism of the sintering process [81-83], it is considered that the driving force of sintering is the reduction of the free energy in the system, which occurs by mass flow leading to a decrease of the surface curvatures and reduction of the surface area until the state of the lowest energy is reached [84].

Due to the difficulty in processing titanium alloys, the net forming technology based on powder metallurgy is particularly attractive. Therefore, MIM titanium alloys have been growing over the past decade, especially in the field of medical implant materials. By the process of the titanium alloys prepared by the melting process, in the finished product (especially in the case of complex shapes), about 80% of the melting alloy is consumed (due to the cutting process) [85]. Also, due to the difficult processability of the titanium alloy [86], this greatly increases the cost of the alloy. The advantages of using the MIM method are obvious. If the shape requirements of complex products are taken into account, MIM can bring huge economic benefits.

2.4 MIM Ti alloy for biomedical application

According to the previous introduction, the advantages (+ +) and disadvantages (- -) of the arc melting method and the MIM method are shown in the following table, which can directly display the comparison between them.

2. State of the art

Table 2.4-1. Comparison characteristics (final products by MIM and melting process)

Characteristics	Fabricate method	
	Arc-melting	MIM
Industrial production efficiency	+	++
Material homogeneity	--	++
Complex shape	-	++
Product Size	++	-
High melting point metal	++	+
Net shape	--	++
Fabrication	++	-

The two preparation methods have their own advantages and disadvantages. The biggest disadvantages of final products fabricated by melting method are the tendency to material inhomogeneity, difficulties to realize complex shape and almost no net-forming ability. These are very serious drawbacks for biological materials, especially implant materials. However, for the MIM method, its disadvantages are that the product size cannot be too large (due to sintering shrinkage, debinding, etc.) and the complex fabrication process. In the field of bio-implant materials, there is no need for a particularly large size (for the most situation), so the MIM method for preparing bio implant materials has obvious advantages. With further research, more and more activity is focused on the preparation of bio-titanium alloys by MIM.

With increasing research on the preparation of bio-titanium alloys by MIM method, more and more Ti-Nb and Ti-Mn series alloys have been studied. Table 2.4-2 shows the mechanical properties of Ti-Nb alloys and Ti-Mn alloys fabricated by different methods. It can be seen from Table 2.4-2, how much research has concentrated on the Ti-Nb series alloys. The content of Nb is mostly above 20% (wt.%), which is around 12.5% (at.%). If Ti-Nb alloys have sound elongation (about 10%), the ultimate tensile strength is usually less than 700 MPa. If the Ti-Mn binary alloy and Ti-Mn-Mo ternary alloy are prepared by the MIM method, the strength of the alloys is generally high (UTS: around 900-1000 MPa), but the elongation is very low (elongation: 4%).

Table 2.4-2. Mechanical properties of Ti-Mn and Ti-Nb alloys (fabricated by powder metallurgy and arc-melting)

Alloy (wt.%)	Yield strength (MPa)	Ultimate tensile strength (MPa)	Elongation (%)
MIM Ti-16Nb (1500) [87]	566 ± 9.0	667 ± 15	3.45 ± 0.44
Arc-melted Ti-14Nb [88]	~610	~700	~11
MIM Ti-10Nb [50]	552±19	638±12	10.5±1.9
MIM Ti-22Nb [50]	649±31	754±7.0	1.43±0.51
As-HIPed Ti-22Nb [50]	687±34	838±14	1.30±0.41
MIM Ti-24Nb-4Zr-8Sn [89]	636 ± 9	656 ± 6	9.2 ± 3.1
MIMTi-29Nb-13Ta-4.6Zr [90]	~576	~650	~3
MIM Ti-13Mn [43]	827 ± 19	888 ± 3	0.9 ± 0.1
MIM Ti-9Mn [34]	~932	~993	~2.6
MIM Ti-6Mn-3Mo [91]	~1042	~1145	~4

3. Motivation and objectives

As shown before, medical implants made from Ti-Nb are very promising. However, costs for Nb are rather high, it hindering the widespread application of this type of alloys [4, 49]. Therefore, this study aims at the partial replacement of Nb by Mn to reduce the costs, without deteriorating the mechanical properties.

If the bio-material is produced by arc melting, this will inevitably lead to further processing (such as cutting and formed), which will also consume a large number of raw materials and increase the cost. However, it is a convenience to prepare raw material. The different compositions are prepared by arc melting for raw alloys production. Hereafter, to determinate of the phase diagram and screening studies on alloys. For further investigations, Metal Injection Moulding is chosen, because it presents possibilities for cost reduction of the final implant (advantages of net-shape). Furthermore, homogenization treatments needed for arc melting can be avoided.

Objectives:

1. To determine and optimize suitable Ti-Mn-Nb alloy compositions by a screening study using arc melting.
2. To obtain better Ti-Mn-Nb alloys by MIM.
3. To determine the influence of interstitials (O, N, C) on MIM processed Ti-Mn-Nb.
4. To understand the strengthening mechanism of the sintered Ti-Mn-Nb alloy with the best mechanical performance.
5. To determine if Y-addition can enhance the mechanical properties further. If yes, to understand the underlying mechanism. The goal is at least the typical properties of Ti-6Al-4V.
6. To assess the biocompatibility of the selected Ti-Mn-Nb alloy by osteoblast MG63 in vitro test in comparison to Ti-6Al-4V.
7. To assess the corrosion behavior of the selected Ti-Mn-Nb alloy in comparison to Ti-6Al-4V.

4. Materials and Methods

4.1 Ti-Mn-Nb alloy produced by arc-melting

4.1.1 Selection of alloy composition

In the study of phase diagram determination, it is customary to use the atomic ratio (at.%) to describe the composition of the alloy. Therefore, the atomic ratio (at.%) is used to indicate the composition of the alloys, rather than the weight ratio (wt.%) in this thesis. However, since the weight ratio is more common as a description in engineering, the relative weight ratio is listed in Table 4.1-1. In the present study, for the convenience of description, all of the alloys will be described as atomic ratios.

This is the first attempt to replace the Nb element with the addition of Mn. Therefore, for the choice of alloy compositions, the experimental phase diagram of Ti-Mn-Nb (Fig. 5.1-2) is used as a guide. Through the investigation of the experimental phase diagram of the Ti-Mn-Nb alloy, the alloys to be produced by arc-melting for this study will be selected in the β single-phase field (using solid solution strengthening by Mn and Nb in Ti matrix), thereby ensuring good tensile strength and elongation. The choice of alloys is shown in Fig. 4.1-1 below. Alloy compositions are listed in Table 4.1-1.

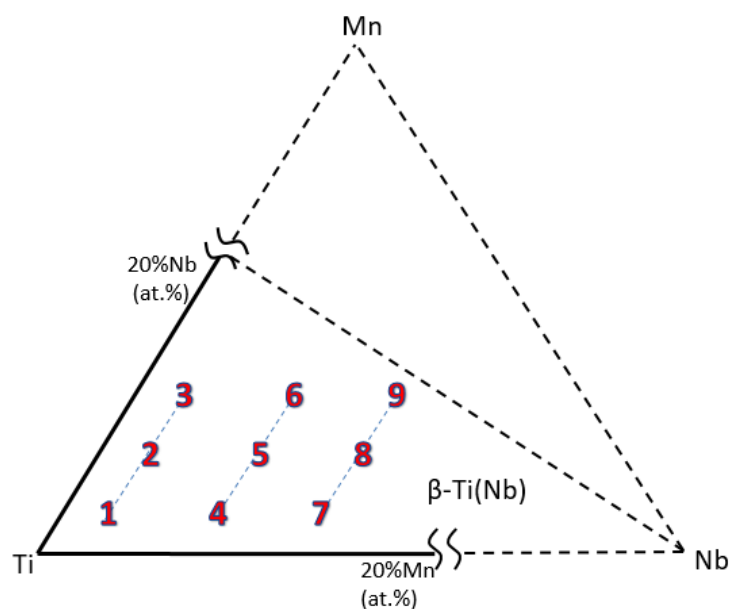


Fig. 4.1-1. Alloy composition selection in Ti-rich region of the Ti-Mn-Nb ternary system

4. Materials and Methods

Table 4.1-1. Ti-Mn-Nb alloy composition by arc-melting

No.	Atomic ratio (at.%)	Weight ratio (wt.%)
1	Ti-4Mn-2Nb	Ti-4.5Mn-3.8Nb
2	Ti-4Mn-8Nb	Ti-4.2Mn-14.2Nb
3	Ti-4Mn-14Nb	Ti-4.0Mn-23.7Nb
4	Ti-10Mn-2Nb	Ti-11.1Mn-3.8 Nb
5	Ti-10Mn-8Nb	Ti-10.5Mn-14.2Nb
6	Ti-10Mn-14Nb	Ti-10Mn-23.7Nb
7	Ti-16Mn-2Nb	Ti-17.6Mn-3.8Nb
8	Ti-16Mn-8Nb	Ti-16.7Mn-14.2Nb
9	Ti-16Mn-14Nb	Ti-15.9Mn-23.7Nb

In general, in a titanium alloy, whether a high-temperature β phase can be retained to room temperature without being decomposed into α phase is measured by the Mo equivalent which was proposed by Bania. According to Bania's description, alloys with $Mo_{eq} > 6\%$ (at.%) which is (10%, wt.%) could form a single β phase [92]. Here is a commonly used classic formula for calculating Mo equivalents [92]. The $(Mo_{eq}) Q$ reflects the simple fact that the β -Ti stability is enhanced when the β phase zone is enlarged by a β -Ti stabilizer. It is expressed as $(Mo_{eq}) Q = 1.0 Mo + 0.74 V + 1.01 W + 0.23 Nb + 0.30 Ta + 1.23 Fe + 1.10 Cr + 1.09 Cu + 1.67 Ni + 1.81 Co + 1.42 Mn + 0.38 Sn + 0.34 Zr + 0.99 Si - 0.57 Al$ (at.%). The Mo-equivalent of Mn is 1.42, which is 6 times higher than the Mo-equivalent of Nb. This indicates that Mn is a strong beta-stabilizing element.

Table 4.1-2. Mo equivalent conversion of Ti-Mn-Nb alloy by arc melting in this study

No.	Alloy (at.%)	Mo equivalent (at.%)
1	Ti-4Mn-2Nb	6.14
2	Ti-4Mn-8Nb	7.49
3	Ti-4Mn-14Nb	8.9
4	Ti-10Mn-2Nb	14.66
5	Ti-10Mn-8Nb	16.04
6	Ti-10Mn-14Nb	17.42
7	Ti-16Mn-2Nb	23.18
8	Ti-16Mn-8Nb	24.56
9	Ti-16Mn-14Nb	25.94

The Mo equivalent is only empirical based on binary systems, and the related mechanism is not known. Due to the complex interactions between multi-elements, in the ternary alloy, the α/β phase field may not strictly observe the Mo equivalent theory. However, it can be used as a reference. Table 4.1-2 shows the Mo equivalents of the different Ti-Mn-Nb alloys produced by arc melting. As can be seen from the data in Table 4.1-2 all the No.1-9 alloys can retain the β phase to room temperature.

4.1.2 Feedstock of Ti-Mn-Nb alloy by arc melting

The pure metals used for this experiment are shown in Table 4.1-3. The morphology of pure metals are shown in Fig. 4.1-2. The metal Ti has a sponge-like structure due to being produced by a metal thermal reduction method. Therefore, before alloying, it must be pre-melted to eliminate the impurity gas in the sponge-Ti [93, 94]. Pure manganese is washed with dilute hydrochloric acid to remove oxides and deposits from the surface [95]. The surface of the Nb element is polished and cut into small pieces for use.

Table 4.1-3. Metals used in this arc-melting method

Element	Purity (at.%)	Status	Supplier
Titanium	99.9	Solid	General Research Institute for Nonferrous Metals, Beijing, China
Manganese	99.7	Solid	
Niobium	99.9	Solid	



Fig. 4.1-2. Morphology of pure titanium, manganese and niobium

The above-mentioned treated feedstock is placed in acetone, ultrasonically cleaned for 10 minutes with water, and the residual liquid on the surface of the feedstock is removed and dried. The above-mentioned processed raw materials are weighed by an electronic precision balance according to Table 4.1-4, with a precision of at least 10 mg for each element.

4. Materials and Methods

Table 4.1-4. Ti-Mn-Nb alloy composition by arc-melting

No.	Atomic ratio (at.%)	Weight ratio (wt.%)	Weight of each elements in 30g ingot		
			Ti (g)	Mn (g)	Nb (g)
1	Ti-4Mn-2Nb	Ti-4.5Mn-3.8Nb	27.52	1.34	1.14
2	Ti-4Mn-8Nb	Ti-4.2Mn-14.2Nb	24.42	1.27	4.31
3	Ti-4Mn-14Nb	Ti-4.0Mn-23.7Nb	21.62	1.21	7.17
4	Ti-10Mn-2Nb	Ti-11.1Mn-3.8 Nb	25.54	3.33	1.13
5	Ti-10Mn-8Nb	Ti-10.5Mn-14.2Nb	22.57	3.16	4.27
6	Ti-10Mn-14Nb	Ti-10Mn-23.7Nb	1.89	3.00	7.11
7	Ti-16Mn-2Nb	Ti-17.6Mn-3.8Nb	23.60	5.28	1.12
8	Ti-16Mn-8Nb	Ti-16.7Mn-14.2Nb	20.75	5.01	4.24
9	Ti-16Mn-14Nb	Ti-15.9Mn-23.7Nb	18.18	4.77	7.06

4.1.3 Material preparation by arc-melting and used facilities

It is important to place the feedstock in the order of Nb, Ti, and Mn from top to bottom as shown in Fig. 4.1-2 in the crucible of arc-melting furnace (Electrode non-consumable arc furnace WS-4). Since the melting point of Nb is much higher than that of Mn, when the arc first contacts the feedstock, the Nb element needs to be melted in the first time, and the next is Ti. It can be seen from the Ti-Nb binary phase diagram (Fig. 2.1-3) that the melting point of the Ti (Nb) alloy is lower than pure Nb. At the last process step, Mn is wrapped by the molten metal liquid to reduce the volatilization of Mn (due to the low vapor pressure of Mn) and melted.

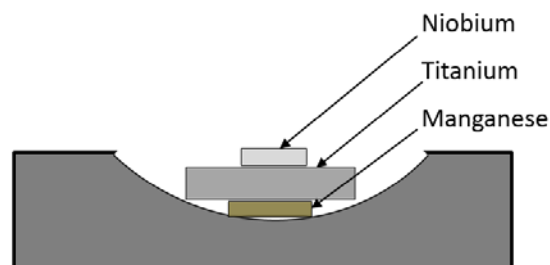


Fig. 4.1-2. The order of feedstock before arc melting

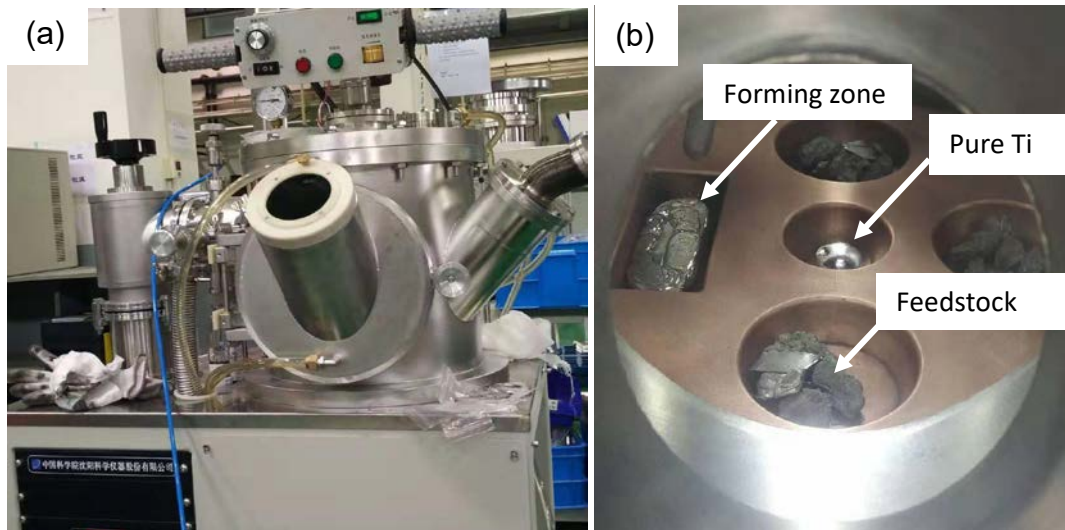


Fig. 4.1-3. Arc melting furnace

In the process of arc melting, the vacuum in the arc melting furnace chamber is first pumped to 5 Pa by a mechanical pump, and then the chamber is purged with argon gas to initially remove air and moisture therein. The air washed twice and vacuumed again to 5 Pa. Thereafter, the vacuum in the chamber is pumped to 6.6×10^{-3} Pa or less by means of a molecular pump, and then argon gas is charged to about 50 kPa, so that the melting is performed under argon gas protection. The arc is first used to melt pure titanium in the copper crucible in the cavity which is smelted for 1 to 2 minutes, which could completely remove the residual oxygen in the cavity. The raw materials placed in the remaining crucibles are then smelted, and the current should be controlled between 150 A and 450 A. It should be noted that after the raw material is turned into a liquid state, the magnetic stirring switch is turned on so that the feedstock is uniformly mixed. At the same time, after the feedstock is melted into an ingot, and subsequently cooled, the manipulator is turned over and the ingot smelted again, and the process is repeated at least 5-6 times. After the smelting is completed, the alloy ingot is taken out, and it was found that the mass loss of the sample during the smelting process is substantially less than 1%. According to the requirements, only 30 g of the ingot can be smelted at a time. Therefore, after melting three ingots, the alloy is placed in the forming zone for moulding and melting. After melting, the Ti-Mn-Nb sample as shown in Fig. 4.1-4. This part of Ti-Mn-Nb alloy preparation by arc melting is carried out at Xiamen University, China.

4. Materials and Methods

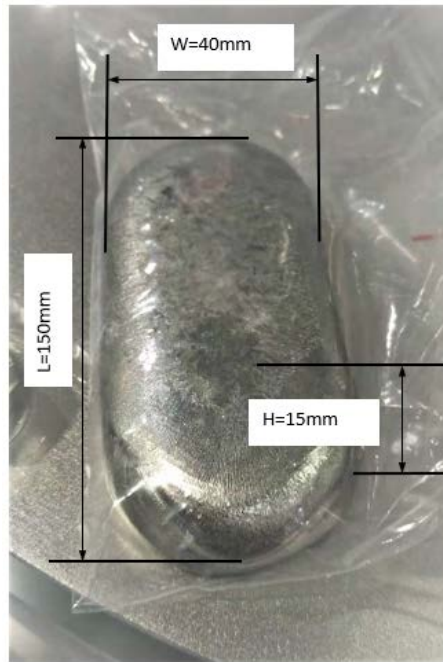


Fig. 4.1-4 Ti-Mn-Nb alloy fabricated by arc melting

4.2 Ti-Mn-Nb alloy processed by MIM

4.2.1 Feedstock of Ti-Mn-Nb alloy by MIM

The preparation of Ti-Mn-Nb alloy by metal injection moulding is carried out at the Helmholtz-Zentrum Geesthacht in Germany. The powder used is listed in the Table 4.2-1 below.

Table 4.2-1 Metallic powders in this study

Element	Shape	Size	Supplier
Titanium	spherical	< 45 μm	AP&C GmbH
Manganese	angular	< 10 μm	Alfa Aesar
Niobium	spherical	< 45 μm	H.C.Starck
Yttrium	angular	< 45 μm	Edgetech

In this paper, nine different alloy composition Ti-Mn-Nb samples are prepared by the MIM method. For each alloy composition 450 g is produced, and the composition and element weights are listed in the following Table 4.2-2.

Table 4.2-2. Ti-Mn-Nb alloy composition by MIM

No.	Atomic ratio (at.%)	Weight ratio (wt.%)	Weight of each elements in 450 g			
			Ti (g)	Mn (g)	Nb (g)	Y (g)
1	Ti-3Mn-1Nb	Ti-3.4Mn-1.9Nb	426.10	15.28	8.61	---
2	Ti-4Mn-2Nb	Ti-4.5Mn-3.8Nb	412.79	20.16	17.05	---
3	Ti-4Mn-4Nb	Ti-4.4Mn-7.4Nb	396.72	19.80	33.48	---
4	Ti-6Mn-2Nb	Ti-6.7Mn-3.8 Nb	402.85	30.15	17.00	---
5	Ti-6Mn-4Nb	Ti-6.6Mn-7.4Nb	387.00	29.61	33.38	---
6	Ti-4Mn-2Nb-0.1Y	Ti-4.5Mn-3.8Nb-0.18Y	412.00	20.14	17.03	0.81
7	Ti-4Mn-2Nb-0.5Y	Ti-4.5Mn-3.8Nb-0.92Y	408.89	20.08	16.98	4.06
8	Ti-4Mn-14Nb	Ti-4.0Mn-23.9Nb	324.36	18.16	107.48	---
9	Ti-10Mn-14Nb	Ti-10Mn-23.7Nb	298.30	45.05	106.65	---

4.2.2 Preparing materials by MIM

Mixing powder

The data of the metallic powders adopted is indicated in Table 4.2-2. The metallic powders were mixed in a double-blades mixer at 120 °C for 4 h under protective argon atmosphere. In addition, the feedstock mixture includes 10 wt.% binder, which contains 60 wt.% paraffin wax, 35 wt.% polyethylene vinyl acetate and 5 wt.% stearic acid.

Injection moulding.

For tensile tests, standard MIM specimens according to ISO 2740 were injection moulded, using a two-cavity mould on a conventional injection-moulding machine (320 S 500-60, Arburg, Germany as shown in Fig. 4.2-1). An injection pressure of 800 bar, an injection rate of 35 cm³/s, an injection temperature of 112 °C and a mould temperature of 43 °C turned out to be adequate parameters for the injection process.

4. Materials and Methods

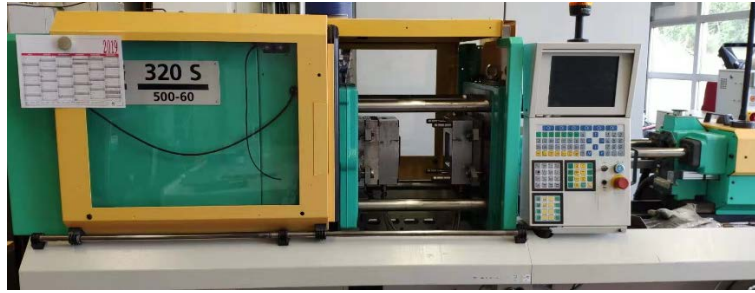


Fig. 4.2-1. Injection-moulding machine

Debinding

The binder system employed here needs a two-step debinding process: Solvent debinding to extract the paraffin wax component and thermal debinding to crack and vaporise the remaining polyethylene. Solvent debinding was performed in a debinding machine (Lömi, Germany as shown in Fig. 4.2-2), using hexane at 40 °C for 1200 min. Thermal debinding and sintering were performed in subsequent steps, using a cold-wall furnace (XVac, Xerion, Germany) with molybdenum heating elements and molybdenum shield packs. The thermal debinding took place under a slight argon flow of 150 l/h at 5 mbar in a temperature range between 250 °C and 400 °C.



Fig. 4.2-2. Debinding machine

Sintering

Sintering took place at 1500 °C for 4 h (XVac, Xerion, Germany as shown in Fig. 4.2-3) under high vacuum (about 10^{-2} Pa) with subsequent cooling to room temperature (10 K/min).



Fig. 4.2-3. Vacuum sintering furnace

The production of Ti-Mn-Nb alloys by metal injection moulding is carried out at Helmholtz-Zentrum Geesthacht, Germany.

4.3 Characterization of the samples

4.3.1 Phase diagram determination

The phase diagram of the titanium-rich region (Nb) was determined by investigating equilibrated alloys, which were prepared by arc melting and subjected to heat treatment at 900 °C. Alloys were sealed in a quartz tube with argon to prevent oxidation. In addition, pure Ti filings were filled into the quartz tube to prevent oxidation. Each alloy was kept for at least 1200 hours at temperature, and then subjected to ice water quenching. Back-scattered electron (BSE) images of equilibrium phases and compositions of the constituent phases were analyzed by using electron probe microanalysis (EPMA) (JXA-8800R, JEOL, Japan). The compositions of each constituent phase given in this study were the average values of three measurements.

4. Materials and Methods

4.3.2 Heat-treatment process of arc-melting Ti-Mn-Nb samples

After the Ti-Mn-Nb alloys are prepared by arc-melting, since the alloy is rapidly cooled from high temperature, the formed microstructure is unstable. The heat treatment is required to eliminate the dendritic segregation, thereby achieving better mechanical properties [96, 97]. According to the phase diagram of the Ti-Mn-Nb ternary alloy at 900 °C, samples were kept at 900 °C for 1 hour and then quenched to room temperature rapidly, in order to preserve the β single-phase structure and prevent the grain growth from affecting the mechanical properties. Due to the activity of the Ti alloy, it can react with O and N at a high temperature, therefore, the sample is sealed in a quartz tube and protected with argon. Pure titanium is placed at the bottom of the quartz tube to consume residual O and N. It is ensured that pure titanium is not in contact with the Ti-Mn-Nb alloy sample to prevent interdiffusion from affecting the microstructure. The schematic are shown in Fig. 4.3-1 below.

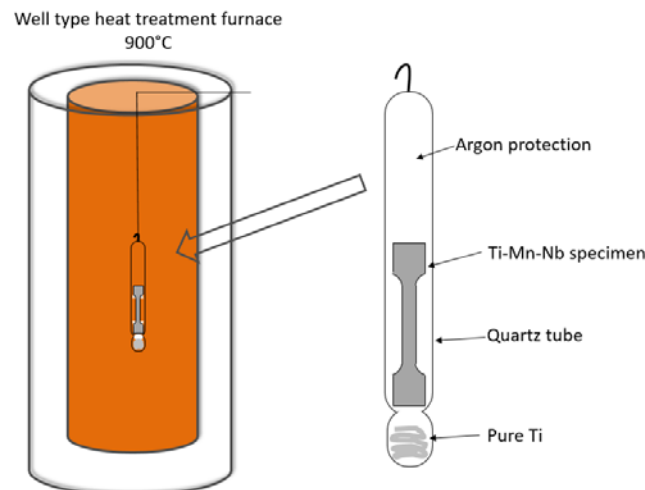


Fig. 4.3-1. Schematic of heat-treatment of arc melted Ti-Mn-Nb alloy

4.3.3 Metallography preparation

The heat treated alloy (sintered sample is the same process) is inlaid into a block by a curing agent and a resin inlay. After the inlay is completed, the sample is ground with sandpaper (from 600 to 2000). Then polishing is carried out on a hard leather polishing cloth using a 30 nm silica polishing liquid. Finally, the alloy sample is etched with a Kroll etchant (Water 92.82%, Nitric Acid 6.11%, and Hydrofluoric Acid 1.07%) until the grain boundaries on the sample surface are visible. The residual etching solution is washed off and the sample is dried.

4.3.4 Impurity levels and relative density

In order to investigate the mechanical properties of sintered Ti-Mn-Nb alloys, the impurity levels including carbon, oxygen, hydrogen and nitrogen are determined using a conventional LECO melt extraction system. The CS-444 equipment is used to measure the carbon level. The TC-436AR is applied to analyze oxygen and nitrogen contents. At least three samples are examined. Therefore, the impurity level values as given in the results section are averaged from these three samples.

The relative density of the sintered Ti-Mn-Nb samples are determined by the immersion method (Archimedes's principle) outlined in ASTM B311.

4.3.5 OM analysis

Optical microscopes Leica DMI 5000M and Olympus PMG3 are used for microstructural examination analysis of Ti-Mn-Nb alloys. Meanwhile, the quantification of average grain size and α/β phase fraction are obtained via ImageJ software (version 1.46r, Wayne Rasband, National Institute of Health, USA) by calculating the area ratio in OM images.

4.3.6 SEM analysis

After the sintered alloy was polished, the sample was washed in distilled water and then washed with pure ethanol. After drying, they adhered to a small conductive platform coated with N650 planar carbon (Plano GmbH, Wetzlar, Germany). After completely drying the N650 plate carbon, the sample was placed in a scanning electron microscope (SEM, TESCAN vega 3 SBU, Brno, Czech Republic). If the fracture surface needs to be analyzed, it could be analyzed by SE mode of SEM directly without covering the N650.

The fracture surfaces of arc-melting samples are observed by SE mode of Electron probe micro analyzer (JXA-8100, Japan) in Xiamen University of China.

4.3.7 X-ray Diffraction

The measurements covering both arc-melting samples and sintering samples, are performed on a Bruker D8-A25 equipped with an Eulerian cradle in Bragg-Brentano geometry using Cu K α radiation (Cu tube with 1.5418 Å). The 2θ angles have been varied stepwise between 20° and 90° with an

4. Materials and Methods

increment of 0.010147° and time of 2 s. Data analysis is performed with common analysis software (BrukerEVA and PDF+4 2014).

4.3.8 Young's modulus measurements

In Helmholtz-Zentrum Geesthacht, Young's modulus of sintered Ti-Mn-Na alloys is measured by the resonant ultrasound spectroscopy (RUS) technique. RUS method is employed because of the non-destructive nature of the measurement, simple operating procedures and simple specimen geometries.

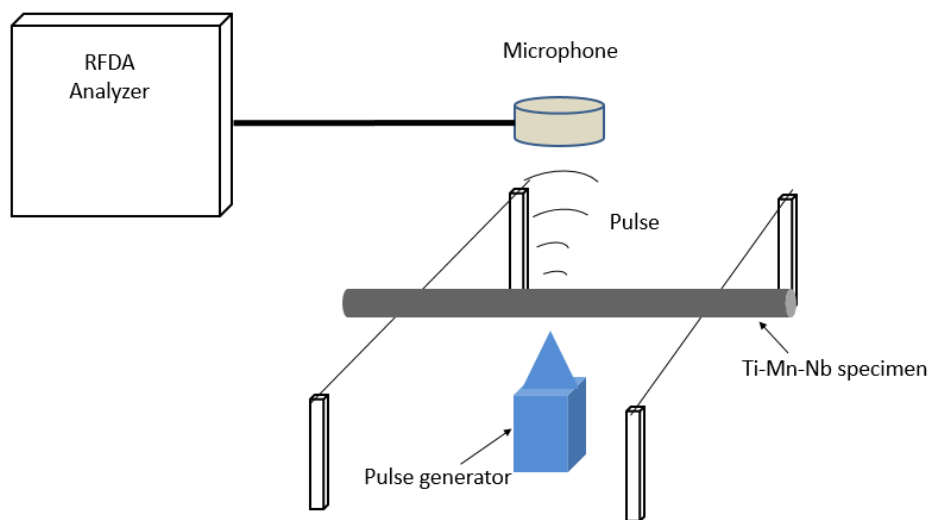


Fig. 4.3-2. Schematic of Young's modulus test of Ti-Mn-Nb specimen

A schematic diagram of the Young's modulus test is shown in Fig. 4.3-2. According to the requirement of ASTM E 1259, to prevent any influence on the vibration by the supports, the specimen is supported by two thin wires located at the fundamental nodes of the test specimen - a distance of $0.224 \times l$ from each end, where l is the length of the specimen [98].

An impulse is produced in the specimen by striking lightly at the center of the specimen. A non-contacting microphone placed above the specimen is used to collect the vibration. The RUS tests were performed using an IMCE resonant frequency damping analyzer (RFDA professional). The RFDA was used to obtain frequency spectra and identify between 6 and 10 overtones for each specimen.

4.3.9 Vickers hardness measurement

The hardness of the sintered samples are measured by a micro-hardness tester (Emcotest Prüfmaschinen, Kuchl, Austria), while the arc-melting samples were measured by a Shimatsu HMV-2T. All of them are ground on sandpapers from P320 to P2500, in order to remove the deformation layers caused by cutting and to ensure flatness. Both types of hardness measurements are carried out in HV5 mode with a diamond indenter, in the form of a right pyramid with a square base and an angle of 136 degrees between opposite faces subjected to a load of 49.03 N. The full load is applied for 10 seconds. The two diagonals of the indentation left in the surface of the material after removal of the load are measured using a microscope and their average is calculated. The schematic of Vickers hardness test in this study is shown in Fig. 4.3-3. At least ten points of each sample are measured to obtain a mean value.

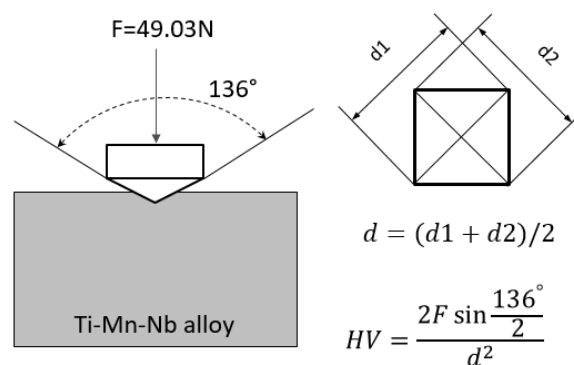


Fig. 4.3-3. Schematic of Vickers hardness test in this study

4.3.10 Tension tests

Tension tests of arc melting samples are performed at room temperature (20 °C) by Instron 5569 testing machine (100 kN tensile test machine). Tension tests are done under a 0.2mm/min strain rate and at least three specimens are tested for each alloy composition. An extensometer (Sansi 50 series, Shenzhen, China) is applied to measure the strain during the tests. The size of tensile test specimens (Fig.4.3-4) of arc-melted Ti-Mn-Nb alloy is chosen according to metallic material room temperature tensile test method (GB/T228-2002 standard) [99].

4. Materials and Methods

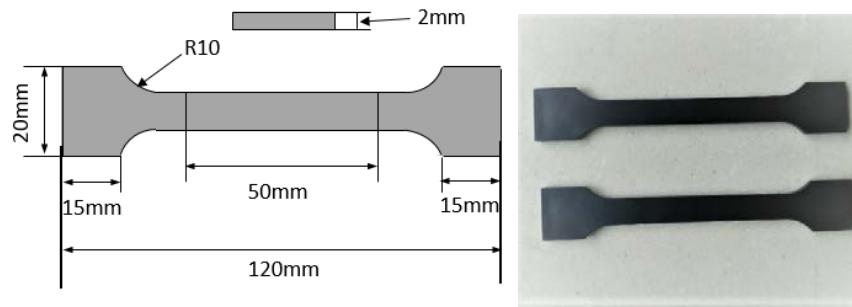


Fig. 4.3-4. Geometry of arc-melted Ti-Mn-Nb samples

Tension tests of sintered samples are performed at room temperature (20 °C) using a Zwick 050 testing machine (Zwick GmbH & Co., KG, Ulm, Germany). Fig. 4.3-5 shows the geometry of samples used for the tensile experiments. All sintered samples (after sintering, slow cooled) can be directly used in the tensile tests without any preparation. Tension tests are done under a 0.2mm/min strain rate and at least three specimens are tested for each alloy composition. An extensometer (BZ2-EXC55000A/AMR) is applied to measure the distance (gauge 25mm) during the tensile tests. The maximum force loading of the Zwick 050 testing machine is 5 kN.

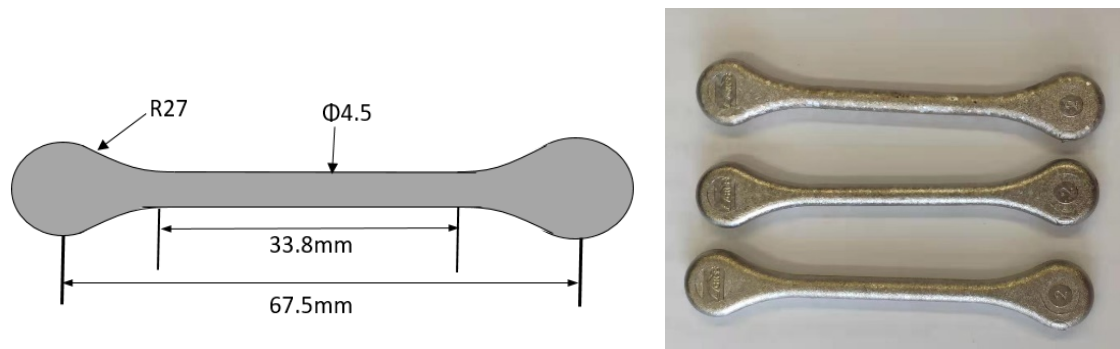


Fig. 4.3-5. Geometry of as-sintered Ti-Mn-Nb samples

4.3.10 TEM analysis

The alloy sample was cut into a sheet having a thickness of 1 mm or less, adhered to a flat stainless steel block, sanded to about 200 μm or less, and then bubbled in an acetone solution to remove the sheet. After cleaning, punching out a small disc with a diameter of 3 mm with a punch, and then grinding it to a thickness of 50 μm or less on a 2000 sandpaper with a special grinder, it is thinned by an ion thinning system GATAN PIPS II 695 (Gatan, Inc. USA) with an initial angle of 8 degrees and a voltage of 6 keV. After the small hole appeared, it is reduced to 4 degrees, 3KeV, respectively, to correct the thin area of the sample. The sample was then placed in a transmission electron microscope

for observation. In this experiment, two transmission microscopes were used: FEI Talos F200 (for arc melting samples in China) and JEOL JEM-2100 (for MIM samples in Germany).

4.3.11 Cell biology assessment

Titanium specimen washing

The alloys used in the experiments of cell biology assessment are all sintered Ti-Mn-Nb alloys produced by the MIM method. The shape of the specimens is a cylinder with a diameter of 4.5 mm and a height of 2 mm. The procedure is as described in the following:

1. Add 2% Hellmanex- Solution to the Ti-Mn-Nb alloy (submerge the alloys). 20 min in the ultrasonic bath
2. Remove the Hellmanex-Solution. Rinse twice with ddH₂O. Submerge the plates with chloroform (remove lipids) 20 min Ultrasonic bath.
3. Remove Chloroform. Add 100% Ethanol (remove proteins and cells debris). Submerge the alloys with ethanol.
4. Remove Ethanol. Submerge the alloys with ddH₂O and repeat again.
5. Remove the Water. Let the plates dry under the fume hood for 30.
6. Placed in an autoclave for sterilization.

Cell culture

Human osteoblast cells (MG-63) are cultured on the surface of Ti-Mn-Nb alloys with DMEM (Invitrogen, USA) supplemented with 10% FBS (foetal bovine serum). Initially, the density of cells cultured on the surface of the alloy is 3000/cm². All cells are incubated at 37 °C in a humidified atmosphere of 5% CO₂. The cells are cultured for 5 days. During this time, the medium is not changed.

Live/Dead staining

The cells are cultured for a total of 5 days. The supernatant is taken out for osmolality test, pH test and LDH assay (see below). The cells are washed with fresh medium without FBS and then 500 µl staining solution (5 mL culture medium without FBS+ 2µl Calcein AM+5µl Ethidiumhomodimer-1) is added. The cells are incubated for 20min. The samples are observed for the live/dead staining immediately by confocal microscope. Meanwhile, the quantification of the fraction of live/dead cells

4. Materials and Methods

is obtained via ImageJ software (version 1.46r, Wayne Rasband, National Institute of Health, USA) by calculating the area ratio of them in the images.

Osmolality and pH

During the 5 days of cell culture, as the cell is metabolized, proliferation, and degradation of the alloy, the supernatant will change. By analyzing the osmolality and pH, one can understand the growth situation of the cells and verify the biocompatibility of the alloy. The osmolality is measured using an osmometer (Osmomat 030, Gonotec, Berlin, Germany). In the test, a new culture medium and a fresh medium incubated 5 days without cells and alloys are set as control groups. The pH test for all supernatants is tested by a Sentron® MiniFET probe. All osmolality and pH measurements are tested 5 times.

DNA isolation

After 5 days culture on Ti-Mn-Nb alloy, osteoblasts (MG63) grown on the surface of Ti-Mn-Nb alloys are used for DNA isolation tests, so that the number of cells can be quantitatively evaluated. The process is the following:

- Aspirate the medium and wash with PBS
- Add 200 µl Lysis-Buffer (25 mM NaOH, 0.2 mM EDTA) per well in a 24-well plate and incubate for 5 min at 37 °C.
- Incubate (98 °C) the solution for 1 h in a thermosphere with 1000 rpm (as blank use only the buffer without cells).
- Add 200 µl Neutralization-Buffer (40mM Tris/HCl pH 5.5) and centrifuge 13.000 rpm for 1 min.
- In 96-well plates (Roche Diagnostic GmbH, Mannheim, Germany), dilute the samples 1:1 in DNA dilution buffer (100 µL sample + 400 µL DNA dilution buffer) and add 50 µL of the diluted sample to the 96-well (triplicate).
- Pipette 50 µL of DNA working buffer in each well.
- Add 50 µL of bisbenzimidazole solution. Incubate for 15 min in the dark.
- Measure fluorometrically (excitation: 355 nm, emission: 460 nm).

Lactate Dehydrogenase (LDH) assay

For osteoblast (MG63) culture on Ti-Mn-Nb alloys experiment, LDH assay is performed by assessing LDH released into the media as a marker of dead cells. LDH is an oxidative enzyme which extensively

exists in cell membranes and cytoplasm. As it is released during tissue damage [100], usually, this means cell death. Determination of serum LDH activity is frequently considered as a good indicator of cellular damage for cytotoxicity studies [101].

In this study, the cell culture supernatants (3 wells per sample) are harvested at 5 days of culture. The LDH assay via an LDH cytotoxicity detection kit (Roche Diagnostic GmbH, Mannheim, Germany) is conducted according to the manufacturer's instructions. Briefly, 100 μ L aliquot of LDH substrate buffer was added into 100 μ L cell supernatant followed by incubation in dark at RT for 20 min. The absorbance was measured with a spectrophotometric microplate reader at 490 nm with 600 nm as a reference (Berthold Technologies GmbH, Bad Herrenalb, Germany). The main equipments used in biological experiments are shown in the Table 4.3-1.

Table 4.3-1. Equipment used in this study of biological assessment

Name	Abbreviation	Supplier
Human osteoblast cells	MG63	Roche Diagnostics, Mannheim, Germany
2% Hellmanex-Solution in ddH ₂ O	Hellmanex- Solution	Hellma, Müllheim
Gibco Culture medium	DMEM GlutaMAX	Fisher Scientific GmbH, Schwerte, Germany
Foetal bovine serum	FBS	PAA Laboratories GmbH, Linz, Austria
Confocal microscope	Microscope	Leica TCS sp8, Germany
Trypsin-EDTA (0.05%), phenol red	Trypsin	Thermo Fisher, Germany
Corning® Costar® TC-treated multiple-well plates	24-well plate	Sigma-Aldrich, Germany
Osmomat 030	Osmometer	Gonotec, Berlin, Germany
Sentron® MiniFET probe	pH test	Sentron®, Germany
LIVE/DEAD viability/cytotoxicity kit	Calcein AM/ Ethidiumhomodimer-1	Thermo Fisher, Germany
LDH cytotoxicity detection kit	96-well plate	Roche Diagnostic GmbH, Mannheim, Germany

4. Materials and Methods

4.3.12 Corrosion measurement

The electrochemical corrosion behavior of the samples is evaluated using a typical three-electrode cell as shown in Fig. 4.3-6. To evaluate the performance of Ti-Mn-Nb alloy in biomedical applications, both EIS and polarization tests are performed in Hanks' balanced salt solution (HBSS) with a given chemical composition. These analyses are performed using a special cell with a sample exposure area of 0.5 cm^2 and an external container that allow the flux of water to regulate the solution temperature. A thermostat is connected to this cell and the temperature is held at $37 \text{ }^\circ\text{C}$.

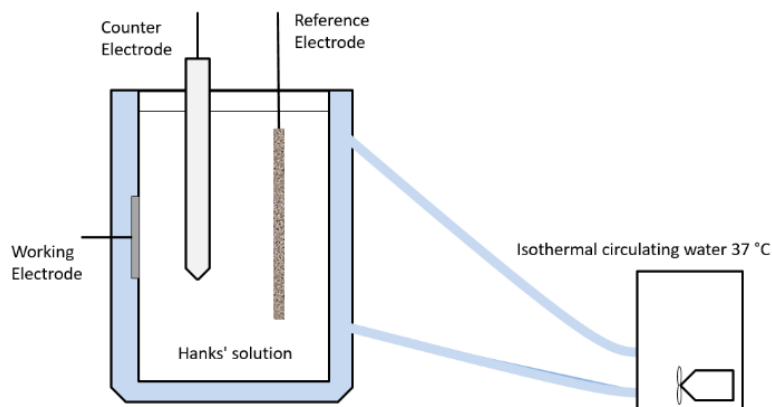


Fig. 4.3-6. Schematic of setup for electrochemical measurement in this study

In this cell, the sample is the working electrode (exposure area of 0.5 cm^2), platinum meshes the counter electrode and an Ag/AgCl electrode is the reference. The cell is connected to a potentiostat Gill AC from ACM instruments for the electrochemical measurements. For regular analyses, the corrosive solution is Hanks' balanced salt solution (HBSS). Before the impedance test, the open circuit potential (OCP) is measured for 2 hours to let the potential stabilize. Then the impedance test is carried out at an amplitude of 10 mV for Ti-Mn-Nb at frequencies ranging from 30000 to 0.01 Hz. The impedance spectra of all the samples are simulated using the software Zview2 from Scribner associates to get more information on the corrosion mechanism.

After the impedance test is finished, the polarization analyses were performed. A potential sweep was applied at a constant scan rate of 12 mV/min, starting 150 mV below OCP and finishing at 2000 mV. Three measurements were carried out for each treatment condition as well as for the untreated sample.

5. Results

5.1 Ti-Mn-Nb experimental ternary phase diagram

This is the first attempt to replace the element Nb with the addition of Mn. Therefore, for the choice of alloy composition, we need to study the phase diagram as a guide. Since the Ti-Mn-Nb ternary alloy has never been reported before, there is no thermodynamic data of the Ti-Mn-Nb ternary system. Thereby, this study needs to determine the Ti-Mn-Nb ternary phase diagram. The element Mn may cause brittleness [44], and we need to reduce the content of the element Nb to reduce the cost which can only be done if the phase equilibria at 900 °C is reliably known. Therefore, the experimental phase diagram at 900 °C (1173 K) for the titanium-rich region was determined. Back-scattered electron (BSE) images of typical equilibrium phases of Ti-Mn-Nb alloys are presented in Fig. 5.1-1.

As is illustrated in the BSE image in Fig. 5.1-1 (a), a single-phase is present. Combining the EPMA result (Table 5.1-1), Ti-10Mn-10Nb can be confirmed to consist of β -Ti (Nb, Mn) phase.

BSE images of the alloys (Ti-35Mn-5Nb, Ti-48Mn-2Nb and Ti-50Mn-8Nb) are presented in Fig. 5.1-1 (b), (d) and (e). In conjunction with the EPMA result (Table 5.1-1) it can be deduced that both of them consist of two phases which are indicated in the figure. Among them, since β -TiMn and α -TiMn (shown in Fig. 5.1-1 (d)) only differ in the content of Mn, they can be distinguished by component analysis (No. 10 in Table 5.1-1).

Fig. 5.1-1 (c) and (e) present constituent phases in Ti-30Mn-25Nb and Ti-45Mn-10Nb, respectively. The EPMA results (Table 5.1-1) indicated that the alloys consist of three phases.

5. Results

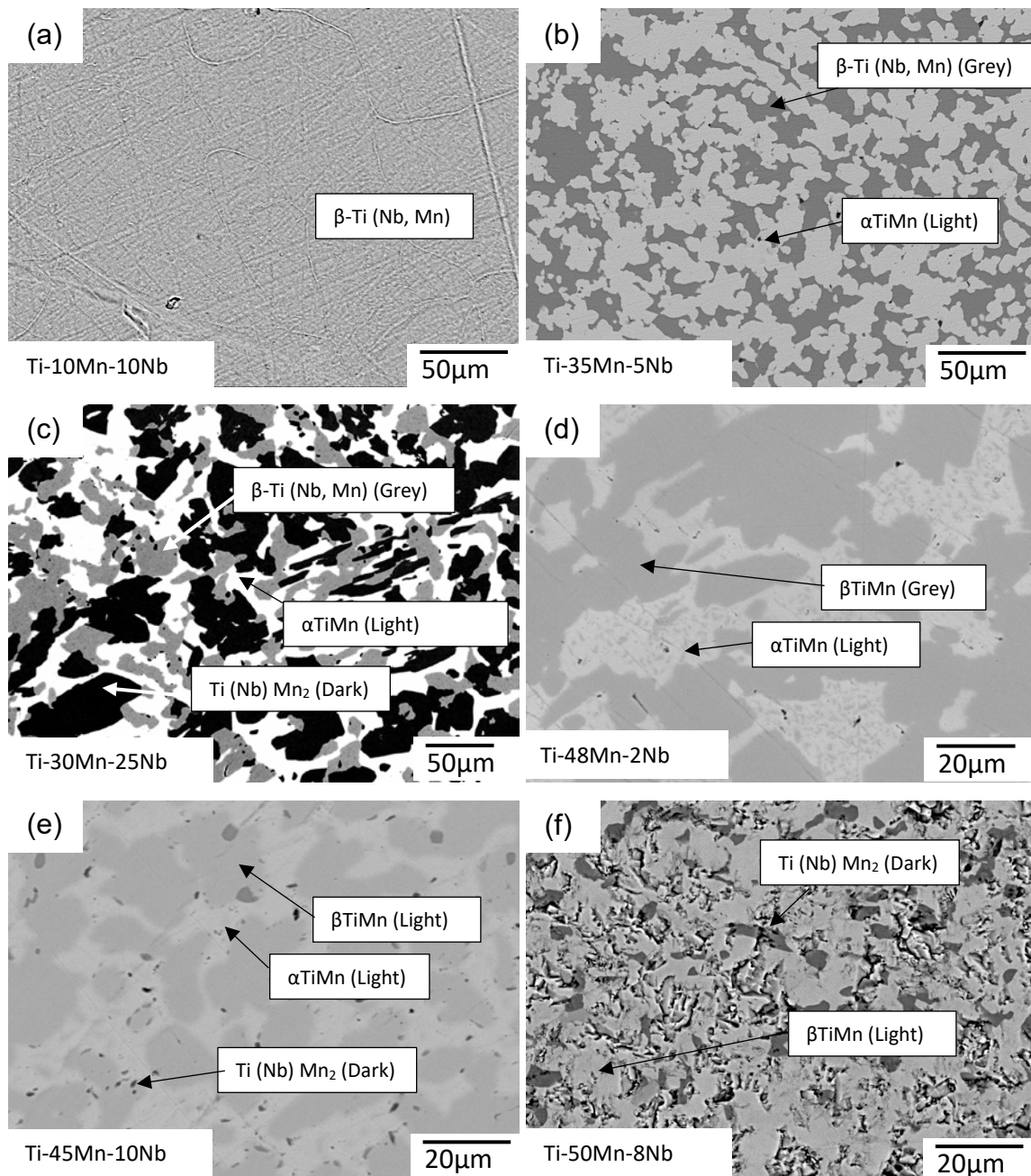


Fig. 5.1-1. Back-scattered electron (BSE) images: typical phases in Ti-Mn-Nb alloys annealed for 1200 hours at 900 °C, (a)-(f) refer to field (1) - (6) in Fig. 5.1-2, respectively.

Table 5.1-1. Determined equilibrium phase composition of the Ti-Mn-Nb ternary system at 900 °C

No.	Nominal composition (at.%)	Composition of phases (at.%)			Real phase equilibria
		Ti	Mn	Nb	
1	Ti-10Mn-10Nb	80.27	9.72	10.01	β -Ti (Nb, Mn)
2	Ti-10Mn-20Nb	70.36	9.61	20.03	β -Ti (Nb, Mn)
3	Ti-10Mn-40Nb	49.67	9.13	41.20	β -Ti (Nb, Mn)
4	Ti-20Mn-10Nb	70.04	19.94	10.02	β -Ti (Nb, Mn)
5	Ti-25Mn-15Nb	65.52	19.27	15.21	β -Ti (Nb, Mn) + α TiMn
		50.02	45.86	4.12	
6	Ti-25Mn-20Nb	54.98	18.21	26.81	β -Ti (Nb, Mn) + α TiMn
		48.90	46.26	4.84	
7	Ti-30Mn-25Nb	49.14	15.02	35.84	β -Ti (Nb, Mn) + α TiMn + Ti (Nb)Mn ₂
		50.21	42.84	6.95	
		34.24	50.64	15.12	
8	Ti-35Mn-5Nb	69.41	22.64	7.95	β -Ti (Nb, Mn) + α TiMn
		49.38	47.54	3.08	
9	Ti-45Mn-10Nb	50.22	42.83	6.95	α TiMn + β TiMn [102] + Ti (Nb)Mn ₂
		47.64	46.24	6.12	
		34.23	50.66	15.11	
10	Ti-48Mn-2Nb	50.77	47.25	1.98	α TiMn + β TiMn
		49.96	50.02	0.02	
11	Ti-50Mn-8Nb	48.20	47.95	3.85	β TiMn + Ti (Nb)Mn ₂
		38.84	52.57	8.59	
12	Ti-57Mn-5Nb	49.50	49.24	1.26	β TiMn + Ti (Nb)Mn ₂
		39.15	56.25	4.6	
13	Ti-65Mn-7Nb	27.87	62.01	10.12	Ti (Nb)Mn ₂

Based on the phase constitutions listed in Table 5.1-1, the isothermal section of the Ti-Mn-Nb ternary system (Ti-rich region) at 900 °C was obtained (Fig. 5.1-2). As can be seen from the Ti-Mn-Nb phase diagram, the solid lines are the phase boundaries based on the experiment, and the dotted line is the estimated phase boundary.

5. Results

In the Ti-rich region (1), a single-phase field of β -Ti (Nb, Mn) is found. In the region (2), the two-phase field β -Ti + α TiMn [103] appears. In the region (3) the three-phase field β -Ti (Nb) + α TiMn + Ti (Nb) Mn_2 [102] is found. Considering the cost, the content of the expensive element Nb should be reduced in the alloy. In parallel the mechanical properties have to be taken into account and the precipitation of brittle phases has to be avoided. Thus, the designed alloy should lie in the β single-phase region.

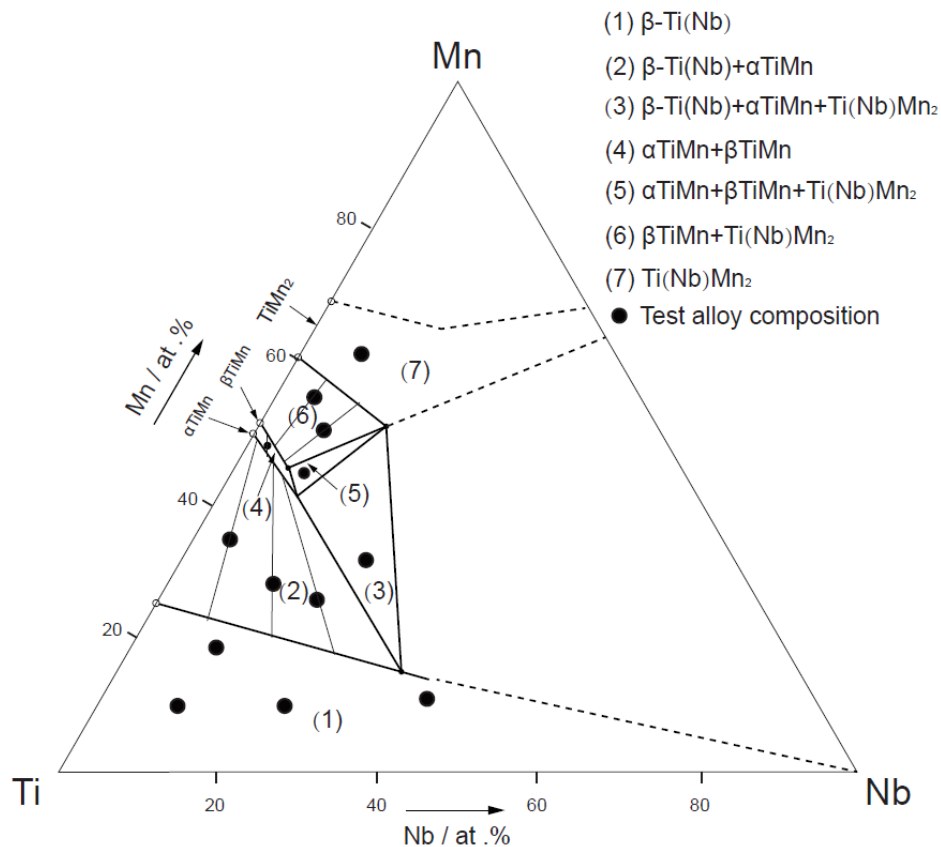


Fig. 5.1-2. Experimental ternary phase diagram (Ti-rich region) of the Ti-Mn-Nb system at 900°C

5.2 Characterization of Ti-Mn-Nb alloys

5.2.1 Microstructure

Fabricated by arc melting

After the Ti-Mn-Nb alloy was prepared by arc-melting, since the alloy was rapidly cooled from high temperature, the formed microstructure is unstable. After 900 °C solution treatment (1 hour kept at 900 °C and then water quenched to room temperature), a single-phase structure was obtained as shown in Fig. 5.2-1 after etching treatment.

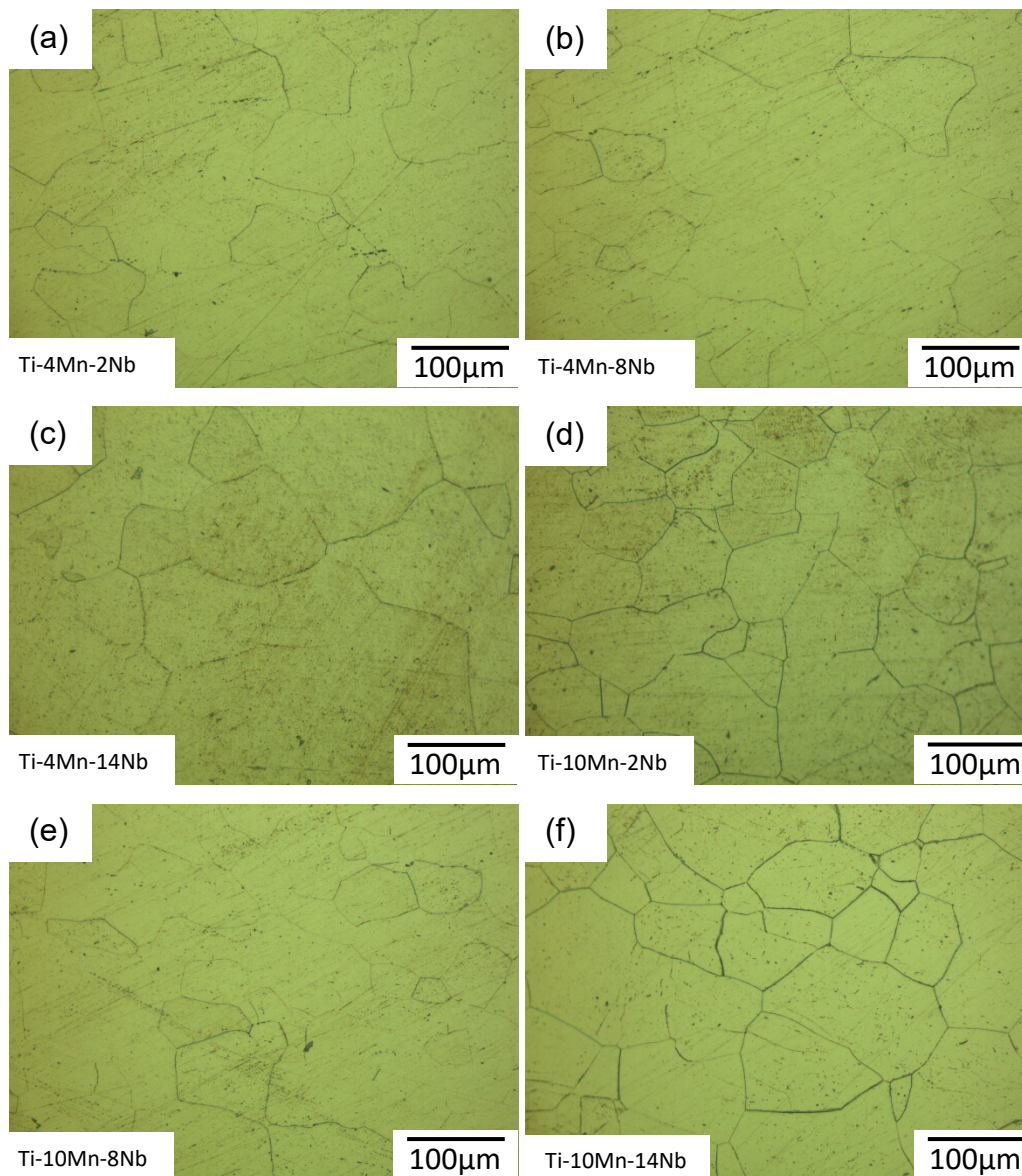


Fig. 5.2-1. Optical microscopy: Microstructure of Ti-xMn-yNb ($x=4, 10$; $y=2, 8, 14$) alloys (arc-melted) after solution treatment. (a) - (f) are respectively Ti-4Mn-2Nb, Ti-4Mn-8Nb, Ti-4Mn-14Nb, Ti-10Mn-2Nb, Ti-10Mn-8Nb and Ti-10Mn-14Nb.

As visible in the Fig. 5.2-1, the microstructures of arc-melted Ti-xMn-yNb ($x=4, 10$; $y=2, 8, 14$) alloys after 900 °C solution treatment consist of a single phase. There is no second phase to precipitate. The average grain size (AGS) is between 100 μm and 200 μm . It can be seen from the experimental Ti-Mn-Nb ternary phase diagram in the isothermal section at 900 °C (Fig. 5.1-2), that these alloys are in β -Ti single phase field. After 900 °C solution treatment and subsequent water quenching, Mn and Nb atoms were dissolved in the Ti-matrix and a single phase is formed.

When the content of the element Mn is increased to 16% (at.%), since the Mn and Nb elements are not completely dissolved in the matrix after only 1 hour of solution treatment at 900 °C, black

5. Results

precipitates were found by optical microscopy after polishing. Although, as seen from the ternary Ti-Mn-Nb experimental phase diagram (Fig. 5.1-2), these three alloys should still be in the β single-phase field at 900 °C. However, the Mn and Nb atoms are not sufficiently distributed after only 1 hour at 900° and the alloy does not have enough time to form a single-phase, thus causing black precipitates in the samples. The precipitates are observed clearly and are indicated in Fig. 5.2-2. The black second phase precipitated at grain boundaries as well as inside the grains. It is foreseeable that this second phase has an effect on the mechanical properties of Ti-Mn-Nb alloys. The phase composition of the alloy needs to be qualitatively analyzed by XRD.

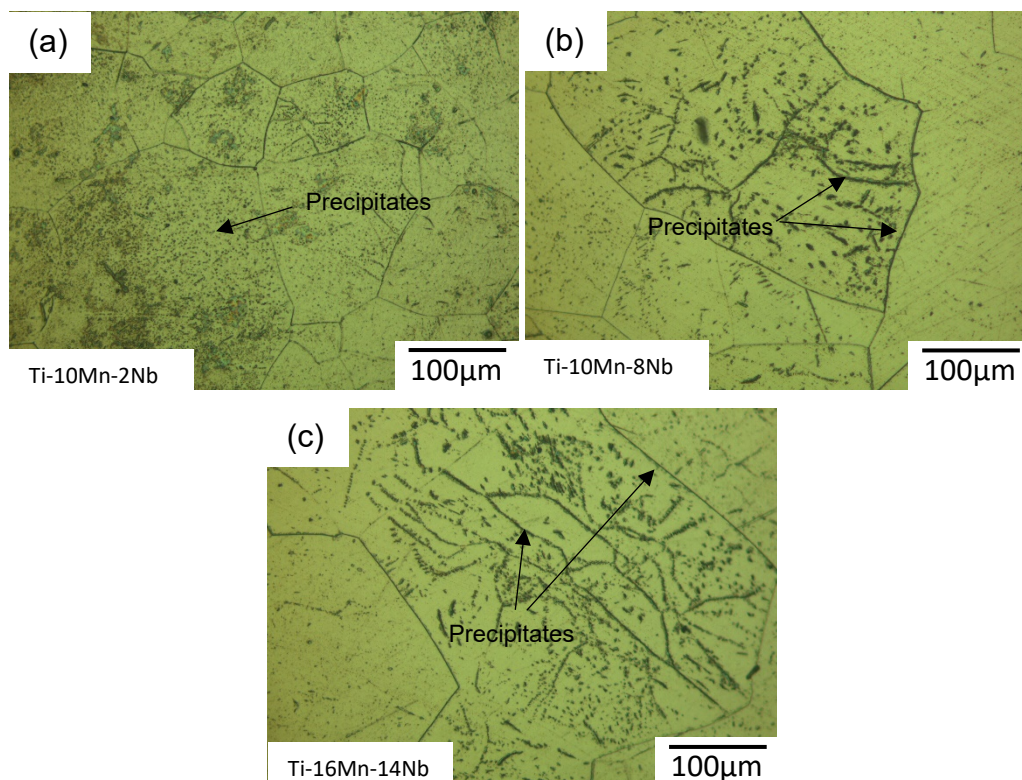


Fig. 5.2-2. Optical microscopy: Microstructure of Ti-16Mn- γ Nb($\gamma=2, 8, 14$) alloy (arc-melting) after solution treatment. (a) - (c) are respectively Ti-16Mn-2Nb, Ti-16Mn-8Nb and Ti-16Mn-14Nb.

Fabricated by MIM

Fig. 5.2-3 shows SEM images (BSE mode) of sintered specimens of Ti-10Mn-14Nb, Ti-4Mn-14Nb and Ti-4Mn-2Nb. These three as-sintered alloys are identical in composition to the alloys prepared by the arc melting process. After sintering, the alloys were cooled down slowly (10 K/min) from high temperature to room temperature. Since there are pores in the microstructure which are indicated by the white arrows in Fig. 5.2-3, the density of Ti-4Mn-2Nb, Ti-10Mn-14Nb and Ti-4Mn-14Nb is about 95% to 97% (shown below in Fig. 5.2-7).

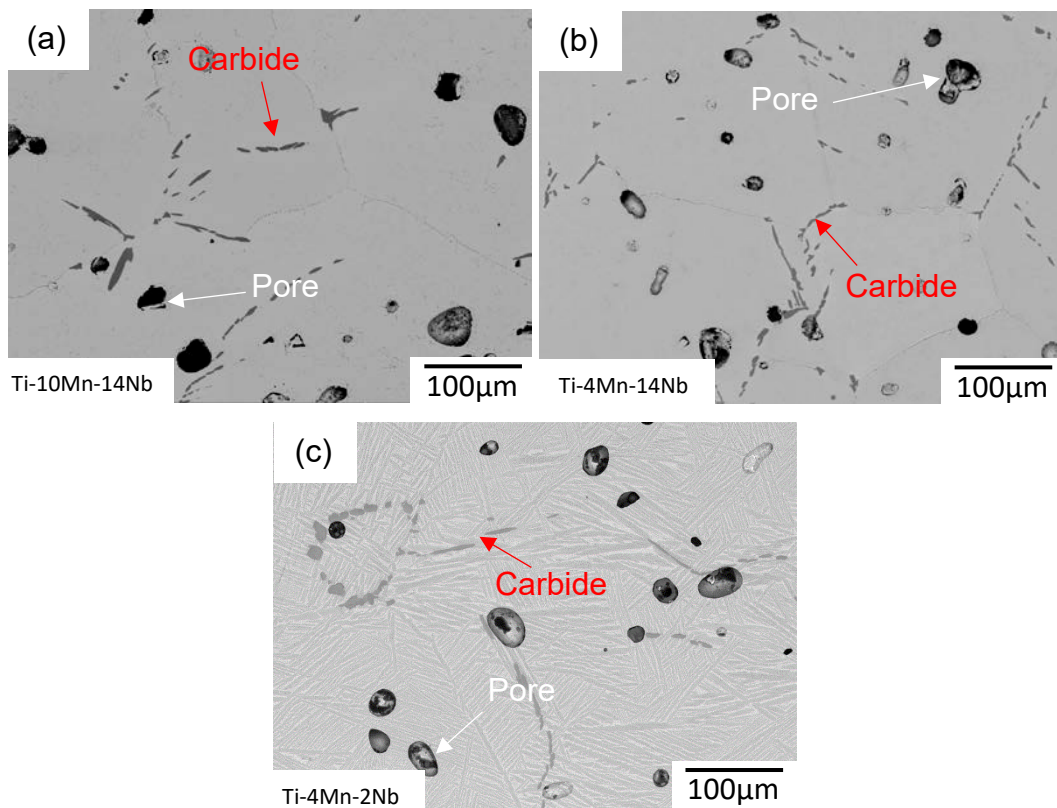


Fig. 5.2-3. SEM images (BSE mode): Microstructure of the different Ti-Mn-Nb alloy. (a) - (c) represent: Ti-10Mn-14Nb, Ti-4Mn-14Nb and Ti-4Mn-2Nb, respectively, produced by MIM.

As visible in Fig. 5.2-3 (a) and (b), it seems that these specimens mainly consist of a single phase, besides the pores and gray carbides (red arrows). The microstructure of Ti-4Mn-2Nb consists of lamellar α and β phase (Fig. 5.2-3 (c)), and numerous pores are visible. The α -lamellae appear light grey while the β -lamellae appear white. However, one can also discern carbides beside α and β indicated by red arrows, that appear darker in the images than the α -phase. Ti-4Mn-2Nb has a completely different microstructure compared to Ti-10Mn-14Nb and Ti-4Mn-14Nb. This can lead to differences in the mechanical properties, which will be shown in section 5.4.

The chemical composition of these three as-sintered alloys is identical to that of arc melted specimens, but due to the different cooling processes, different microstructures are exhibited. It can be expected that the mechanical properties are also different.

Fig. 5.2-4 shows the SEM images (BSE mode) of sintered specimens of Ti-xMn-yNb ($x=3, 4, 6$; $y=1, 2, 4$) alloys. Some obvious pores can be observed which are indicated by white arrows. The microstructure of all Ti-xMn-yNb ($x=3, 4, 6$; $y=1, 2, 4$) alloys consists of lamellar α and β phase. However, as indicated

5. Results

by the red arrows, there is also a third slim phase, which is identified as the Ti_2C phase in the next sections. The addition of different amounts of the elements Mn and Nb in Ti-xMn-yNb ($x=3, 4, 6$; $y=1, 2, 4$) only changes the phase volume fraction of α and β , and also the grain size. The results are indicated in section 5.2.2 (Fig. 5.2-6).

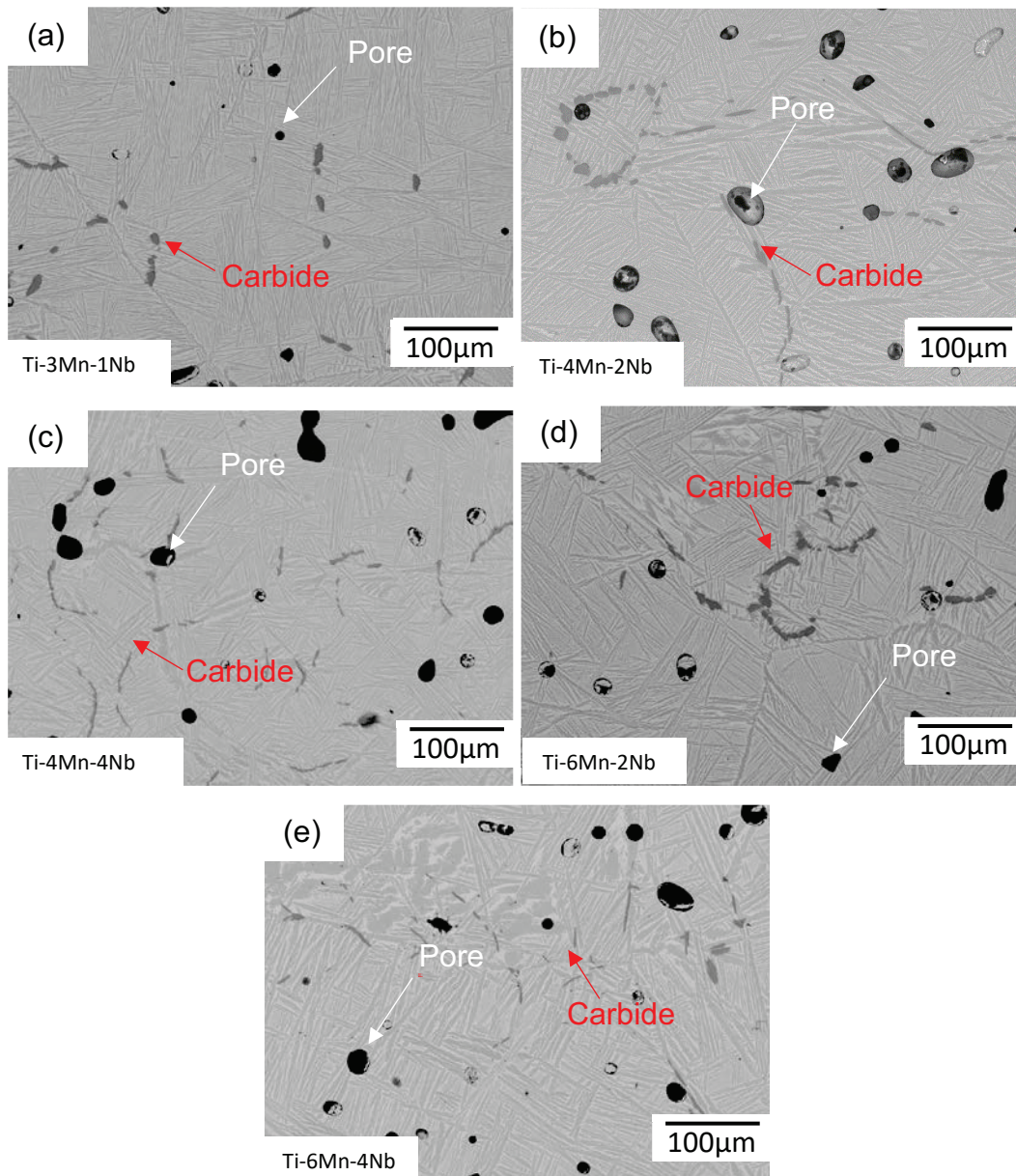


Fig. 5.2-4. SEM images (BSE mode): Microstructure of the different Ti-Mn-Nb alloys. (a) - (e) represent: Ti-3Mn-1Nb; Ti-4Mn-2Nb; Ti-4Mn-4Nb; Ti-6Mn-2Nb and Ti-6Mn-4Nb, respectively.

There is no obvious regularity of the positions where carbides precipitated. They form at grain boundaries as well as inside the grains. This is of interest as carbides are known to have a possible

adverse effect on the mechanical properties of Ti-alloys [104]. Thus, it can be expected that they affect also the mechanical properties of the Ti-Mn-Nb alloys investigated here, accordingly.

Fig. 5.2-5 shows the microstructures of the Ti-4Mn-2Nb alloy with 0%, 0.1% and 0.5% (at.%) yttrium addition. It can be found in Fig. 5.2-5 that all show a typical lamellar α and β phase microstructure. However, in Figs. 5.2-5 (b) and (c) a white spheroidal precipitate phase appeared which is indicated by black arrows. This phase was identified as Y_2O_3 (see section 5.3).

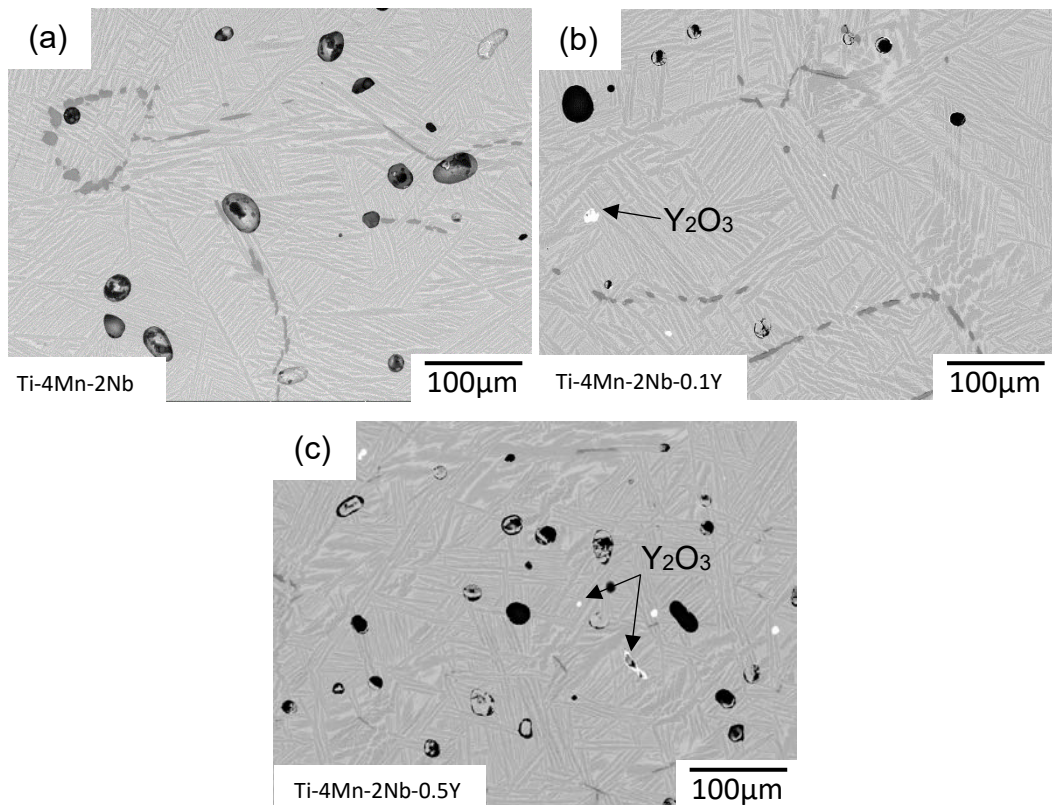


Fig. 5.2-5. SEM images (BSE mode): Microstructure of the Ti-Mn-Nb alloy with a trace yttrium element addition. (a) - (c) represent: Ti-4Mn-2Nb, Ti-4Mn-2Nb-0.1Y, Ti-4Mn-2Nb-0.5Y, respectively.

5.2.2 α/β phase fraction and average grain size of Ti-Mn-Nb alloys

The α/β phase fractions of as-sintered Ti-Mn-Nb alloys are determined and shown in Fig. 5.2-6. Except for the alloys Ti-4Mn-14Nb and Ti-10Mn-14Nb, all other as-sintered Ti-Mn-Nb alloys exhibit $\alpha+\beta$ phase structures. However, the volume fractions of α and β phase are different. X marks the volume fraction of the α/β phase. A higher α/β phase fraction represents a relatively higher fraction of α phase relative to β phase fraction. In Ti-xMn-yNb ($x=3, 4, 6$; $y=1, 2, 4$) alloys, it can be clearly seen that the ratio is gradually decreasing. This is due to the addition of β stabilizing elements (Mn and Nb) which could

5. Results

decrease the transition temperature of α/β , thereby causing more of the β -phase to remain at room temperature [105]. The ratio of α -phase in Ti-3Mn-1Nb is the highest, and that in Ti-6Mn-4Nb is the lowest. With the addition of Y (0.1% and 0.5%), the ratio of α/β is increased, compared with the alloy Ti-4Mn-2Nb. This indicates that Y has the characteristics of α stabilizing element, which can promote the expansion of the α -phase region, thus retaining more α -phase at room temperature. Ti-4Mn-14Nb and Ti-10Mn-14Nb exhibit single β -phase, which is why the ratio is zero.

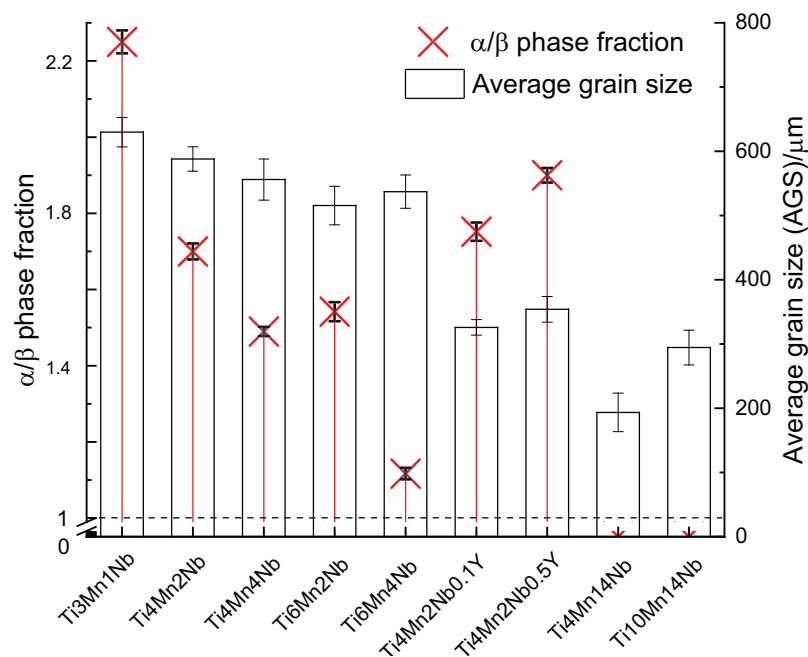


Fig. 5.2-6. α/β phase fraction and average grain size of Ti-Mn-Nb alloys by MIM

5.2.3 Density and Young's modulus of Ti-Mn-Nb alloy processed by MIM

Density is important for sintered alloys and it relates to the success of alloy sintering [106]. The densities of sintered Ti-Mn-Nb alloys are shown in Fig. 5.2-7. The porosities were determined by the Archimedes's principle test. It can be seen in Fig. 5.2-7, that a density between 94% and 97% could be achieved for all sintered Ti-Mn-Nb alloys.

The Young's modulus of Ti-Mn-Nb alloys is measured by the resonant ultrasound spectroscopy technique and results are shown in Fig. 5.2-7. Seen from the results, Young's modulus decreased with

an increase in Mn and Nb content. The sintered Ti-Mn-Nb alloys exhibit a Young's modulus between 70 and 100 GPa.

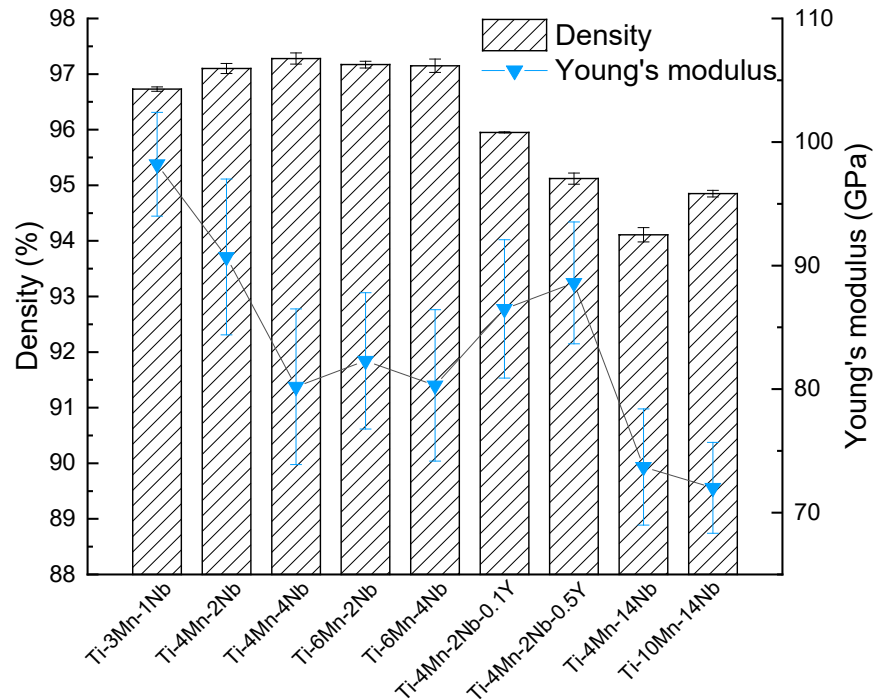


Fig. 5.2-7. Density and Young's modulus of MIM Ti-Mn-Nb alloy

5.3 X-ray diffraction

Samples fabricated by arc-melting

The XRD spectra of Ti- x Mn- y Nb ($x=4, 10$; $y=2, 8, 14$) alloys (arc-melted and subsequently annealed at 900 °C for 1 h, WQ) are displayed in Fig. 5.3-1. It can be found that all these alloys contain β -Ti and the corresponding peaks are marked in the figure.

In the XRD results, there is a slight deviation (around 0.8°) of 2θ angle of the XRD diffraction peaks, which is due to lattice distortion caused by the addition of alloying elements. Different contents of Mn and Nb which are dissolved in the Ti-matrix, replaced the Ti atoms in the unit cell accordingly changing the lattice constant, resulting in a slight angular change in the XRD peak.

5. Results

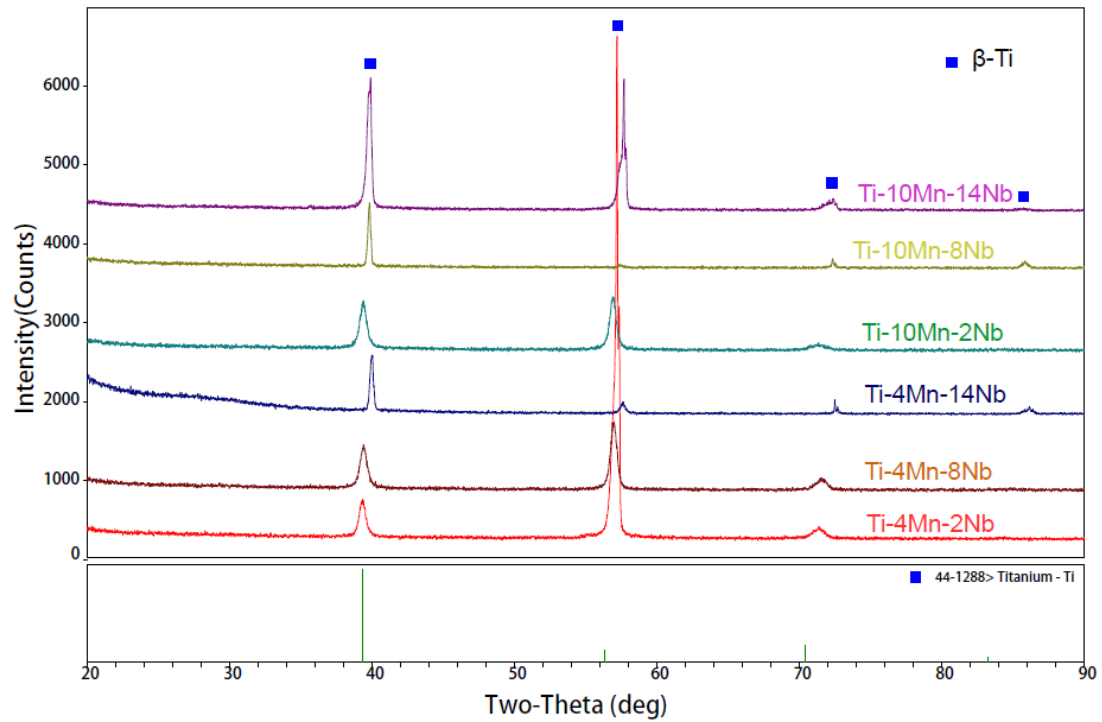


Fig. 5.3-1. XRD results for Ti-xMn-yNb (x=4, 10; y=2, 8, 14) alloys (arc-melting) after solution treatment.

After XRD analysis of the Ti-16Mn-yNb (y=2, 8, 14) alloy, the results are shown in Fig. 5.3-2. Diffraction peaks of two phases appear in the alloy. The matrix phase is β -titanium, and the other phase can be determined as the TiMn phase after comparison with the PDF standard card (#07-0132). The result is consistent with the microstructure in Fig. 5.1-2. It is indicated that the TiMn phase appears in the Ti-16Mn-yNb (y=2, 8, 14) alloy as the content of Mn increased to 16% (at.%).

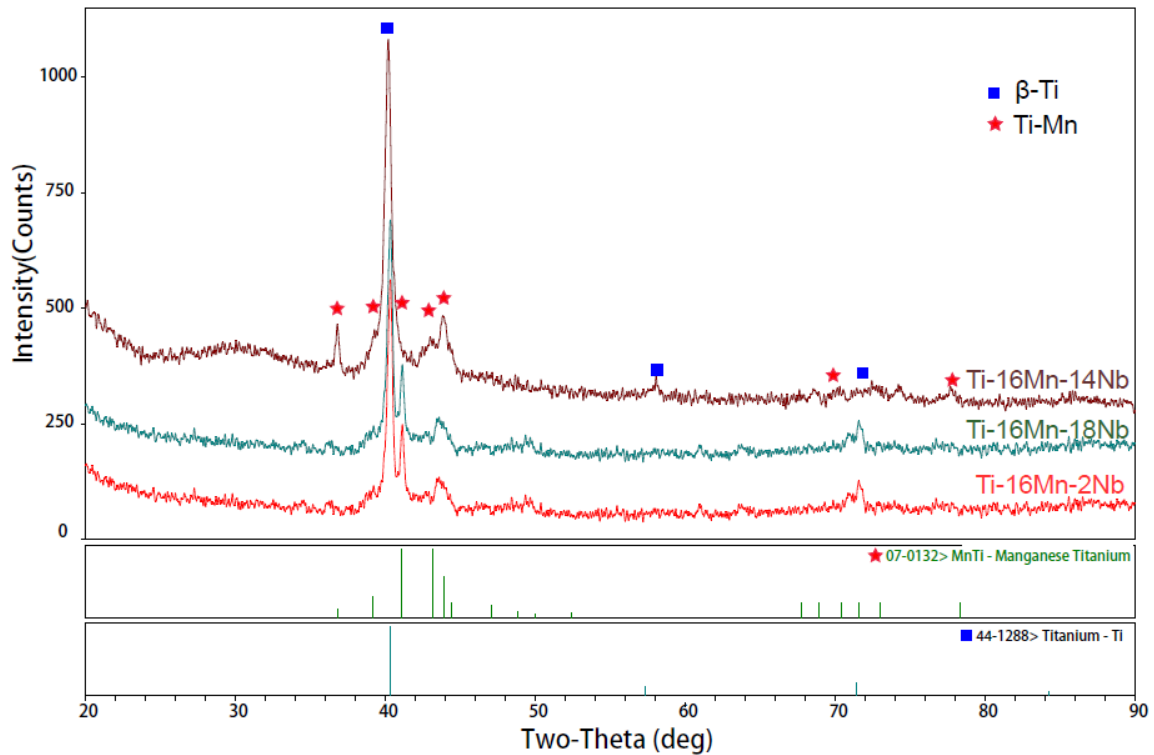


Fig. 5.3-2. XRD results for Ti-16Mn-yNb ($y=2, 8, 14$) alloy (arc-melting) after solution treatment.

Samples fabricated by MIM

In Fig. 5.3-3, the curves correspond from top to bottom to Ti-3Mn-1Nb, Ti-4Mn-2Nb, Ti-4Mn-4Nb, Ti-6Mn-2Nb, Ti-6Mn-4Nb, Ti-4Mn-2Nb-0.1Y, Ti-4Mn-2Nb-0.5Y, Ti-4Mn-14Nb and Ti-10Mn-14Nb all fabricated by MIM. The most pronounced peaks belong to α -Ti (indicated by red dots), while some other peaks can be identified as β -Ti, which are marked by blue squares. The small peaks appearing near 36° and 42° belong to the Ti_2C carbide phase (discussed in section 5.5). The peak intensity of the Ti_2C phase is very low due to its low relative amount.

5. Results

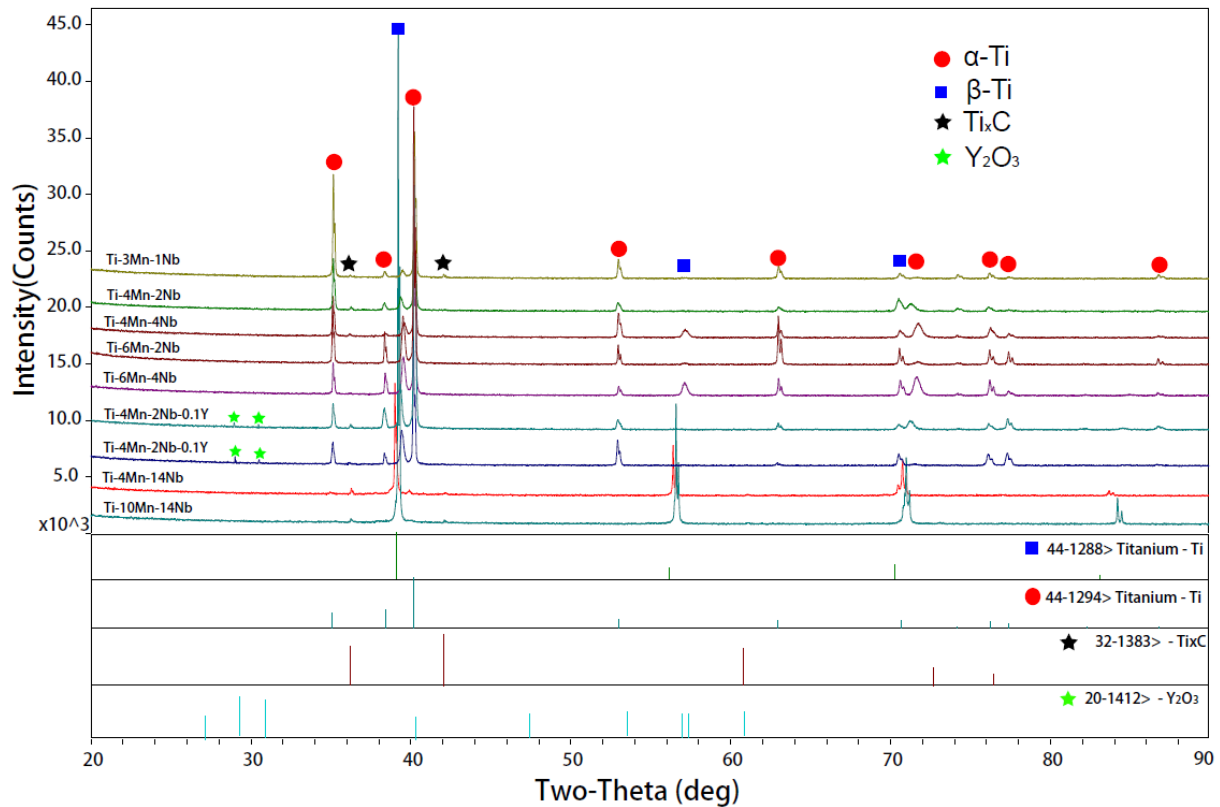


Fig. 5.3-3. XRD results of Ti-Mn-Nb alloy fabricated by MIM in this study

In the MIM process, an organic binder is used, which introduces some amount of carbon into the alloy. Although most of the binder was removed during the debinding and sintering process, the remaining carbon in the alloy reacts with titanium and forms carbides, if the carbon solubility in the alloy is exceeded. Meanwhile, as reported, the β stabilizers could reduce carbon solubility [107], thereby promoting the precipitation of carbides. Ti_2C as a precipitate is expected to affect the mechanical properties of Ti-alloys [87, 108, 109] the mechanical properties of the Ti-Mn-Nb alloys were investigated and the results of tensile tests are shown in section 5.4.3.

5.4 Mechanical properties

5.4.1 Hardness

Fabricated by arc-melting

After the Ti-Mn-Nb alloys fabrication by arc melting, completely dense specimens are formed. Then, the hardness of the alloy is related to the microstructure. Different Mn and Nb contents will result in different hardness. The Vickers hardness of $Ti-xMn-yNb$ ($x=4, 10, 16$; $y=2, 8, 14$) is shown as Fig. 5.4-1.

When the specimens consist of single β -phase, which is true for the first six alloys in Fig. 5.4-1, all atoms are dissolved in the alloy matrix. Ti-4Mn-2Nb reached the highest hardness of about 441 HV and Ti-10Mn-8Nb the lowest (341 HV). As the Nb content in the alloy increases while the Mn content remains constant, the hardness is decreasing. When Mn content is at 16% which is the case for the last three alloys, as the TiMn phase precipitated, overall, the hardness increased to about 400HV.

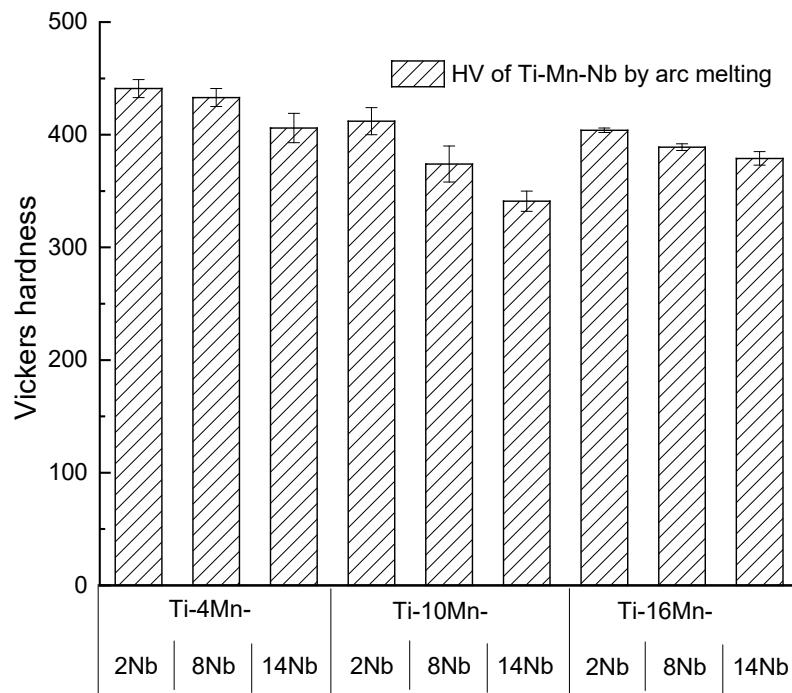


Fig. 5.4-1. Vickers hardness of Ti-xMn-yNb (x=4, 10, 16; y=2, 8, 14)

Fabricated by MIM

After the Ti-Mn-Nb alloys are fabricated by MIM, the specimens consisted of single β phase or lamellar $\alpha+\beta$ phase. Each alloy was tested at 12 positions, and the average was taken. The results are shown as Fig. 5.4-2. In the general, the Vickers hardness of as-sintered samples does not change much with the composition of the Mn and Nb content, but remains around 245 HV. Due to the fact that the specimens are not completely dense and in a kind of an annealed state after sintering, the hardness is lower than the average value of the Ti-Mn-Nb specimens (around 400 HV) produced by arc melting.

5. Results

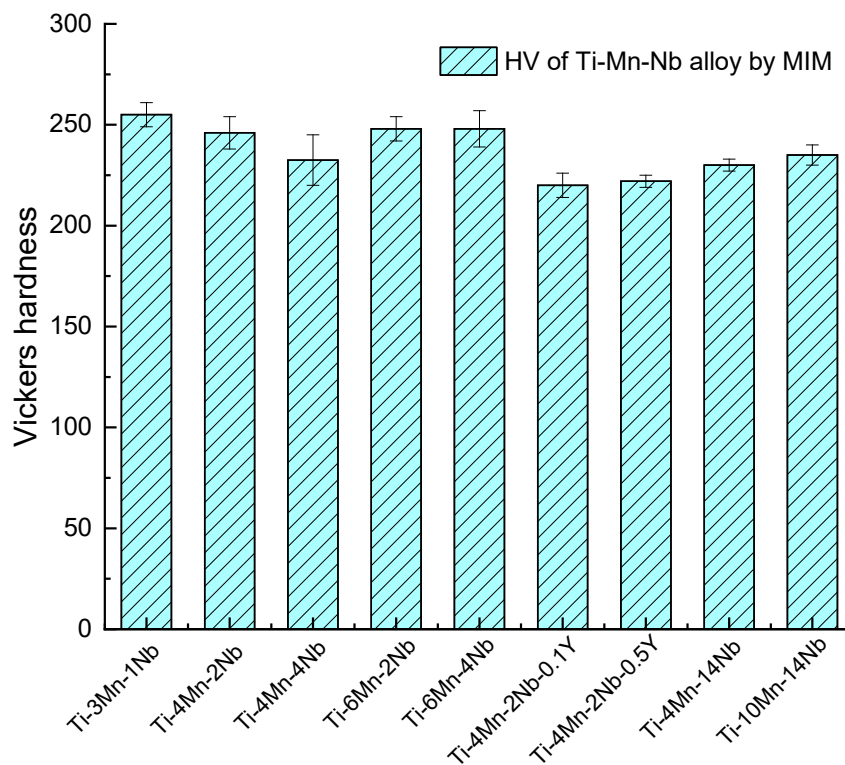


Fig. 5.4-2. Vickers hardness of Ti-Mn-Nb alloy as sintered

5.4.2 Tensile properties of samples fabricated by arc-melting

After heat treatment at 900 °C for 1 hour and subsequent water quenching to room temperature, the ultimate tensile strength and elongation were recorded. Fig. 5.4-3 shows the results. Grey columns represent the ultimate tensile strength while yield strength is displayed in hatched style. Meanwhile, blue squares indicate the corresponding values for plastic elongation.

The first six specimens of Ti-xMn-yNb (x=4, 10; y=2, 8, 14) alloys exhibited over 700 MPa UTS which is better than the last three alloys. When the Nb content is constant, UTS increases with increase of the Mn content. On the contrary, UTS is not sensitive to the change of Nb content when the Mn content is constant. The highest UTS is achieved by Ti-10Mn-yNb (y=2, 8, 14) alloys reaching about 760 MPa. Elongation is improved by increasing the Nb content, no matter if Mn content is 4% or 10%. The highest elongation (around 10.5%) is exhibited by Ti-4Mn-14Nb and Ti-10Mn-14Nb. Combined with the determined strength, Ti-10Mn-14Nb appears to show the best combination of both high UTS and elongation.

As manganese content increased to 16%, independent of the Nb content, the UTS of the last three compositions of alloys drops sharply and fail brittle under tensile load. In general, after preparation by arc melting, Ti-xMn-yNb (x=4, 10; y=2, 8, 14) alloys after 900 °C solution treatment exhibit good mechanical properties, including strength and hardness.

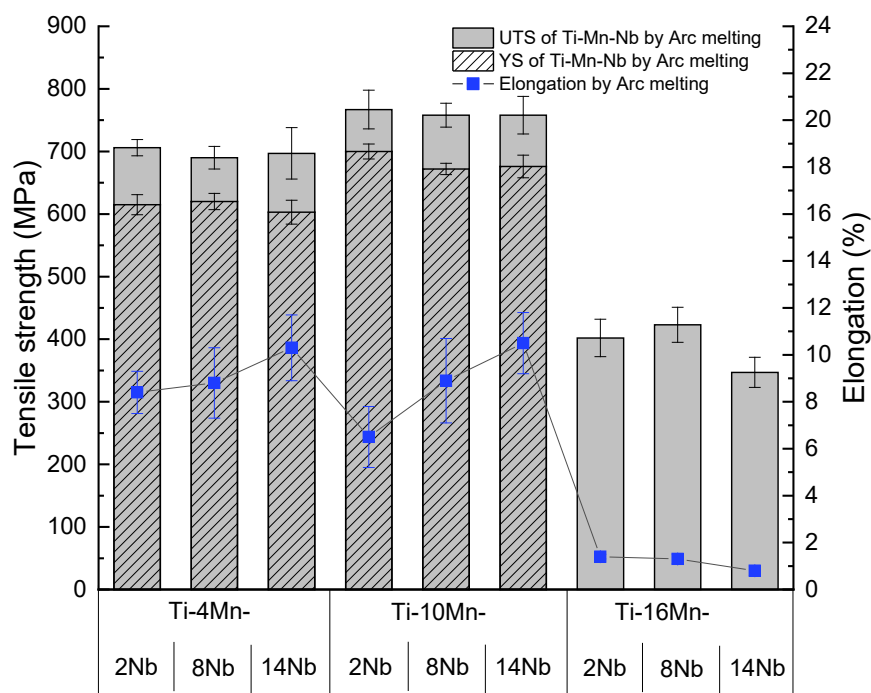


Fig. 5.4-3. Ultimate tensile strength (UTS), yield strength (YS) and elongation to fracture of Ti-Mn-Nb alloys after solution treatment.

5.4.3 Tensile properties of samples fabricated by MIM

Interstitial elements

Due to the uniqueness of the MIM method, oxygen, carbon and nitrogen as interstitial elements are inevitably introduced during the sintering process. These elements dissolve in the matrix of Ti and even form compounds with titanium [87, 110]. This leads to a change in mechanical properties. Thus, these interstitial elements need to be evaluated.

5. Results

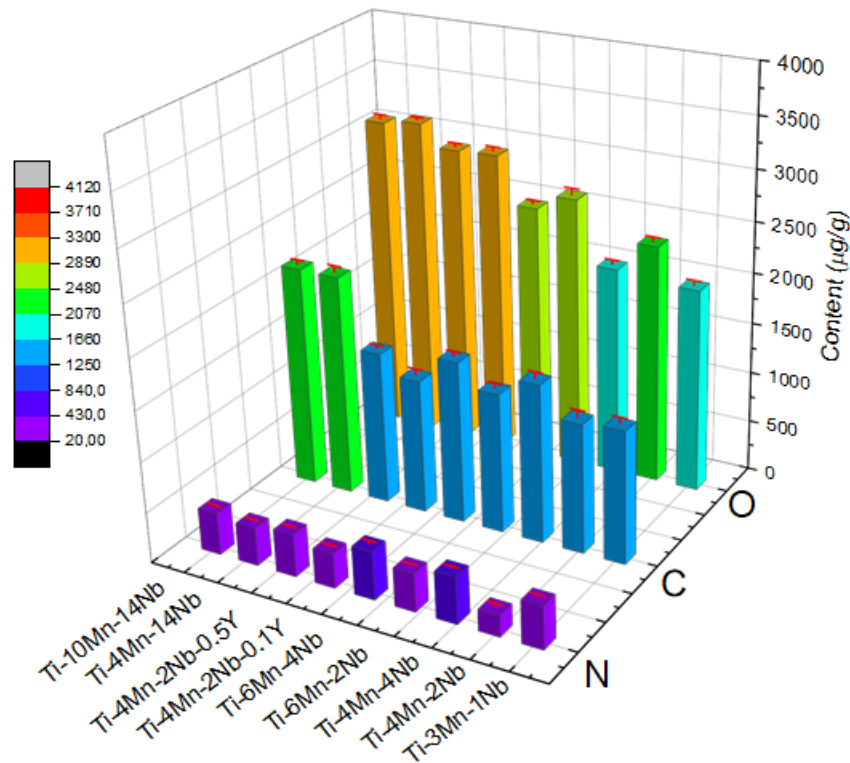


Fig. 5.4-4. Interstitial element levels of Ti-Mn-Nb specimens fabricated by MIM in this study.

The interstitial elements of the MIM-fabricated Ti-Mn-Nb specimens are shown in Fig. 5.4-4. The carbon content of these two compositions (Ti-10Mn-14Nb and Ti-4Mn-14Nb alloys) shows a bit higher than others. Except for these two alloys Ti-10Mn-14Nb and Ti-4Mn-14Nb, it can be seen that the content of carbon does not show significant differences. This may be caused by debinding or sintering process. The content of oxygen is very small difference in Ti-Mn-Nb alloys, being not higher than 3500 $\mu\text{g/g}$. These are relatively normal levels of $\alpha+\beta$ phase Ti alloys [111]. Due to Ti-10Mn-14Nb and Ti-4Mn-14Nb having more alloying elements (14% Nb and 4%, 10% Mn), the O content is slightly increased, but it is also in the normal range. For alloys containing Y, the rare earth element yttrium has a strong affinity to oxygen [112, 113] and, therefore, tends to introduce additional O into the alloy. Simultaneously forming a second phase containing a Y element, this may cause a change in the mechanical properties of the alloy. The mechanical properties of as-sintered Ti-Mn-Nb alloys are revealed in the following Fig. 5.4-5.

Tensile properties

In Fig. 5.4-5, grey columns and blue squares represent the ultimate tensile strength and elongation to fracture of the Ti-Mn-Nb alloys, respectively. Also yield strength is shown as hatched light blue on the

grey columns. The column at the right side (UTS=780 MPa) and the red triangle (A=10%) represent the ASTM (F2885 Grade 5 undensified) requirement for Ti-6Al-4V processed by MIM [114].

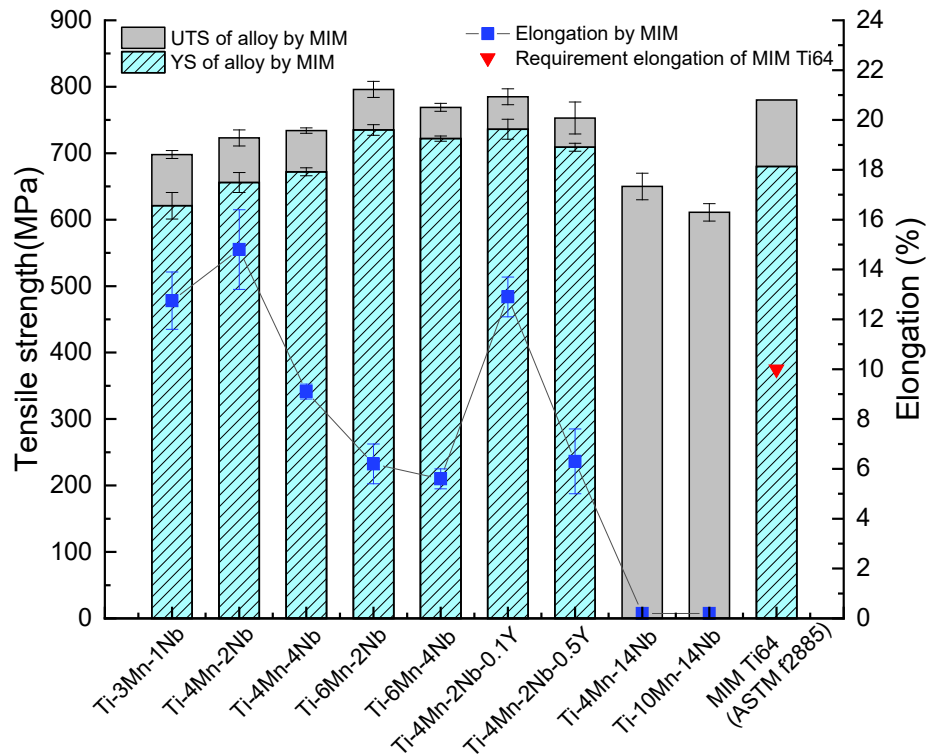


Fig. 5.4-5. Ultimate tensile strength (UTS), yield strength (YS) and elongation to fracture of Ti-Mn-Nb fabricated by MIM

The Ti-4Mn-2Nb alloy exhibits the best balance between strength and ductility: around 725 MPa (UTS), 642 MPa (YS) and 16% (elongation). Its Young's modulus is 92 GPa. Mn and Nb are both β -stabilizing elements and can dissolve into the Ti matrix and improve the tensile strength of the alloy by solid solution hardening. Thus, the UTS of Ti-4Mn-2Nb is higher than that of Ti-3Mn-2Nb. Accordingly, with the Mn content increasing, Ti-6Mn-2Nb does show an even higher tensile strength (around 790 MPa) than Ti-4Mn-2Nb (725 MPa). This behavior is typical as Mn is reported to be a solid solution strengthening element [14]. However, the elongation is reduced to 6.2%, which is much lower than the 16% elongation of Ti-4Mn-2Nb. The effect of an increasing Nb content is qualitatively similar but less pronounced at least when considering UTS. For Ti-4Mn-4Nb, UTS has increased to 750 MPa, but elongation is reduced to 9.8%.

With 0.1% and 0.5% (at.%) of yttrium addition, the tensile strength of Ti-4Mn-2Nb-0.1Y was significantly improved to 800 MPa with about 14% ductility. These mechanical performances have

5. Results

exceeded ASTM (F2885 Grade 5 undensified) requirement [60] for MIM Ti-6Al-4V which is shown in the right of Fig. 5.4-5. Meanwhile, the UTS of Ti-4Mn-2Nb-0.5Y is about 780 MPa, thus, also significantly improved compared to Ti-4Mn-2Nb, but the elongation was reduced from 16% to about 6%.

5.5 Fracture

Samples fabricated by arc-melting

To further understand the reasons for the differences in the mechanical properties of the Ti-Mn-Nb alloys fabricated by arc-melting, after tensile tests, the fracture surfaces were characterized by SEM (SE-mode). Micrographs of the fracture surfaces (Ti-xMn-yNb ($x=4, 10$; $y=2, 8, 14$)) are shown in Fig. 5.5-1.

For all alloys, characteristics of plastic fracture as e.g. dimples are well visible. With the Nb content increasing, shape and size of the dimples change, as Fig. 5.5-1 (a), (b) and (c) show. In Fig. 5.4-3 (section 5.4.2) it is visible, that while the Nb content changed from 2% to 14% and Mn is held at 4%, the elongation increased from 7.4% to 10.3%. Compared with Ti-4Mn-2Nb the dimples of Ti-4Mn-14Nb are larger and deeper. Similarly, when the Mn content is 10%, as shown in Fig. 5.5-1 (d), (e) and (f), the dimples become larger and deeper with increasing Nb content.

In case of alloys with same Nb content there is no obvious difference in the fracture morphology with increasing amount of Mn (cf. Fig. 5.5-1 (a) vs (d), (b) vs(e) and (d) vs (f)).

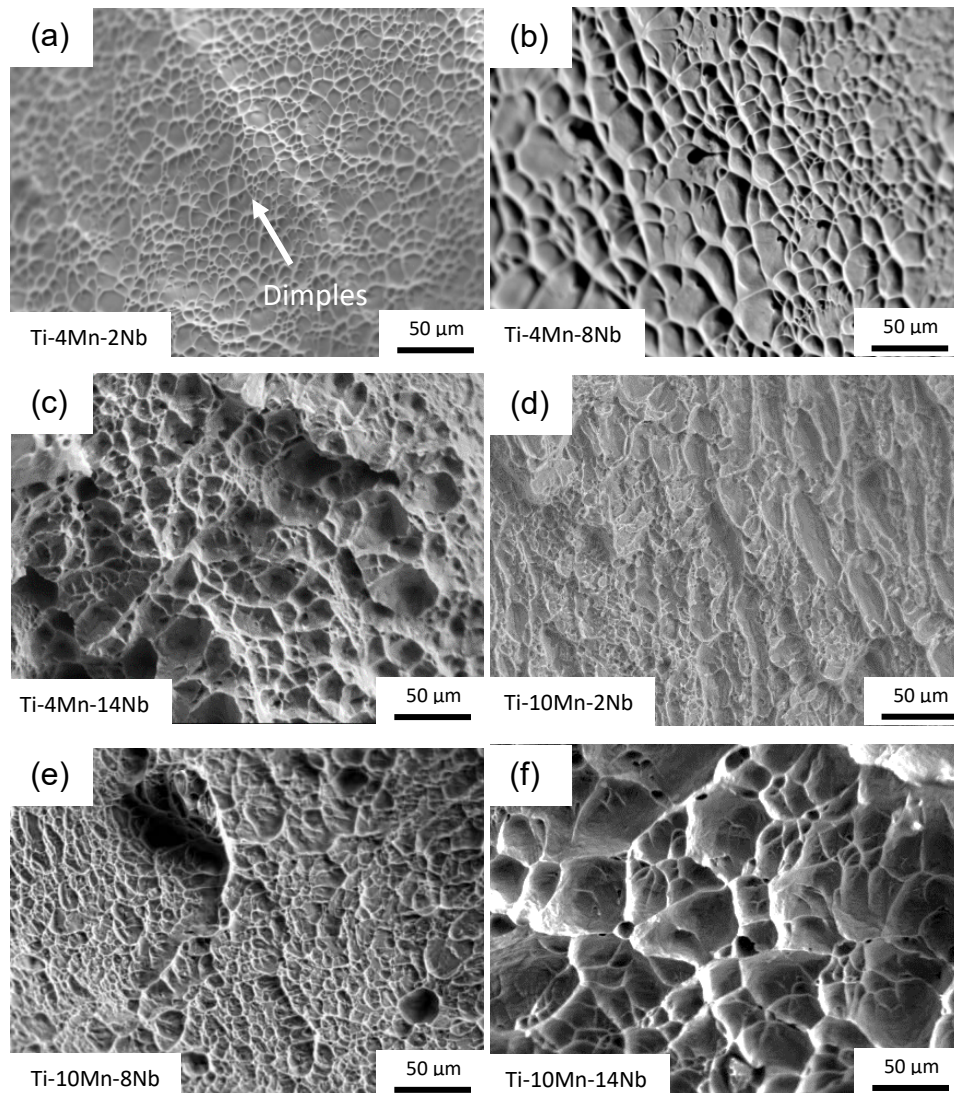


Fig. 5.5-1. SEM images of tensile fracture surfaces of Ti-xMn-yNb ($x=4, 10$; $y=2, 8, 14$) specimens after solution treatment. (a): Ti-4Mn-2Nb, (b): Ti-4Mn-8Nb, (c): Ti-4Mn-14Nb, (d): Ti-10Mn-2Nb, (e): Ti-10Mn-8Nb, (f): Ti-10Mn-14Nb.

After Mn is increased to 16%, independent on Nb content ranging from 2% to 14%, the fracture surfaces show cleavage-like feature, which are typically associated with brittle fracture. Fig. 5.5-2 shows completely different fracture morphologies compared to Fig. 5.5-1. Since Mn is increased to 16%, the brittle TiMn phase has formed at the grain boundaries and inside the grains as visible in Fig. 5.2-2. During tensile loading, cracks initiated from this brittle phase [115, 116]. Ti-16Mn-yNb ($y=2, 8, 14$) alloys almost exclusively have transgranular cleavage-like features, including river patterns. It shows that there is almost no ductility of the matrix.

5. Results

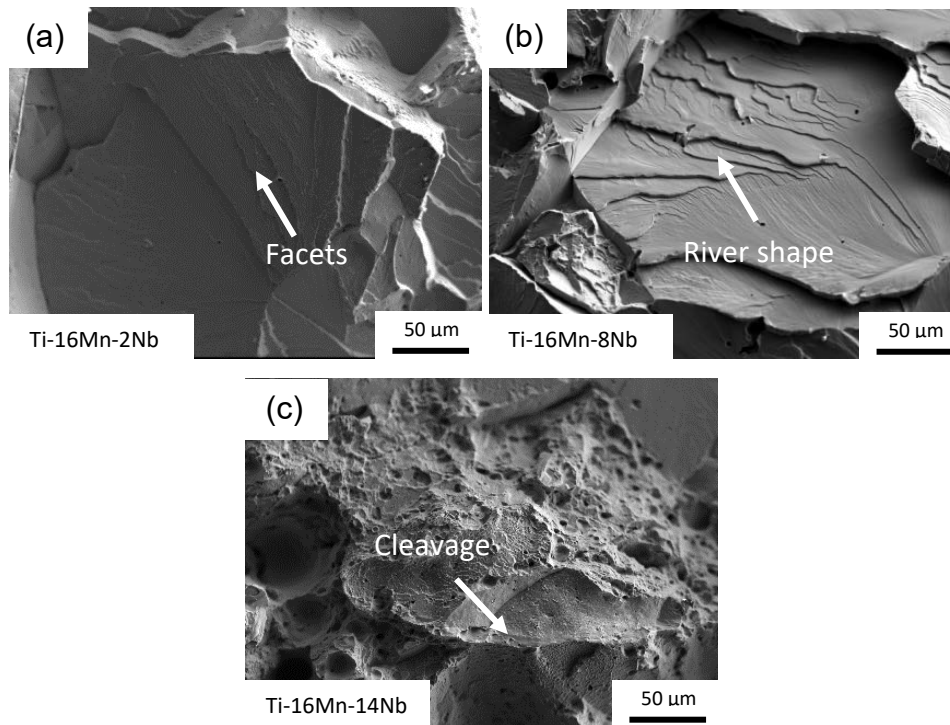


Fig. 5.5-2. SEM images of tensile fracture surfaces of Ti-16Mn-yNb(y=2,8,14) alloy after solution treatment. (a)-(c) refer to Ti-16Mn-2Nb, Ti-16Mn-8Nb and Ti-16Mn-14Nb, respectively.

Samples fabricated by MIM

The as-sintered Ti-10Mn-14Nb, Ti-4Mn-14Nb, and Ti-4Mn-2Nb specimens shown in Fig. 5.5-3 (a)-(c) have the same alloy composition as the specimens prepared by arc-melting (Fig. 5.5-1 (a), (c), (f)), but exhibit significantly different mechanical properties and fracture surface morphologies.

Fig. 5.5-3 (a) and (b) show both features of brittle fracture, as torn structures can be observed and a large number of pores appear on the fracture surface. The tearing has the characteristics of transgranular fracture. It indicates that the matrix of Ti-10Mn-14Nb and Ti-4Mn-14Nb is already very brittle. The Ti-4Mn-2Nb specimen in Fig. 5.5-3 (c) is an $\alpha+\beta$ two-phase structure. The fracture of Ti-4Mn-2Nb exhibits a large number of deep dimples. It is a typical plastic fracture surface corresponding with the achieved elongation of 16%.

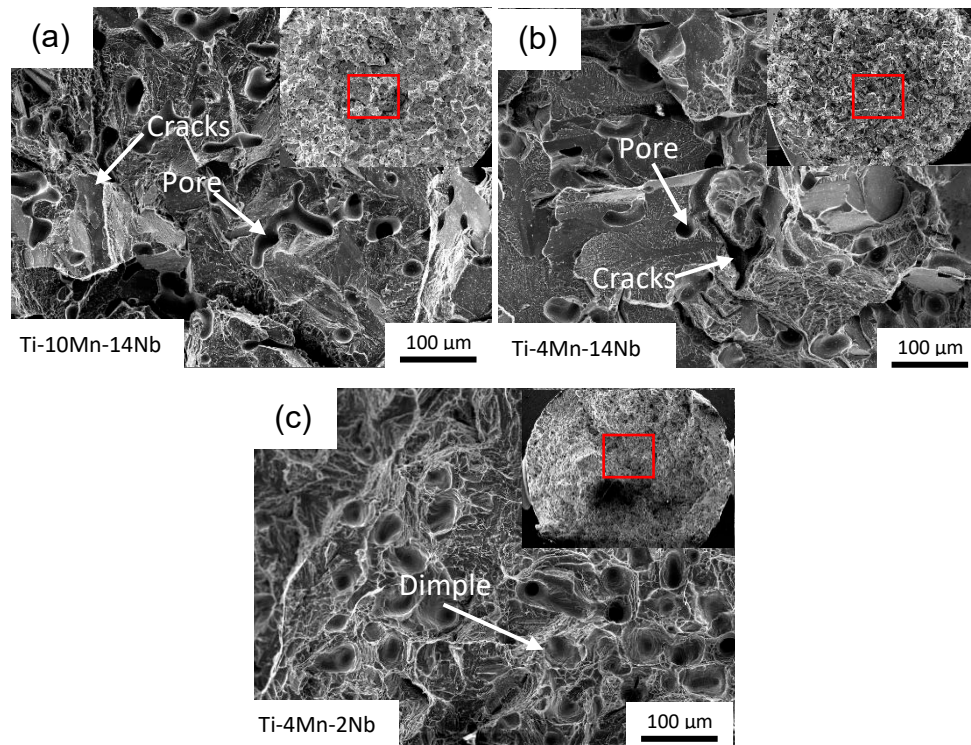


Fig. 5.5-3. SEM images of tensile fracture surfaces (SEM images) of Ti-Mn-Nb alloys fabricated by MIM after tensile failure. (a) Ti-10Mn-14Nb, (b) Ti-4Mn-14Nb, (c) Ti-4Mn-2Nb. The low-magnification image in the upper right corner of each micrograph shows the location of the micrograph with respect to the specimen cross section marked by a red rectangle.

From the appearance of the fracture surfaces (Fig. 5.5-4), they all belong to plastic fracture, well corresponding to the results from the tensile tests (Fig. 5.4-5). However, due to different Mn and Nb contents, there are some differences in the morphology of the fracture surfaces. In Fig. 5.5-4 (a) and (b) the fracture surface is almost exclusively covered by large and deep dimples indicating good ductility. With increasing Mn and Nb content, fine cracks appear as visible in Fig. 5.5-4 (c), (d) and (e). Probably, these cracks correspond to the location of former Ti_2C carbides. Due to the brittleness of the Ti_2C phase, the carbide particles are detached from the matrix during the tensile deformation and fell out after fracture. It can be assumed that the presence of a large amount of Ti_2C causes a decreased elongation of the specimens.

5. Results

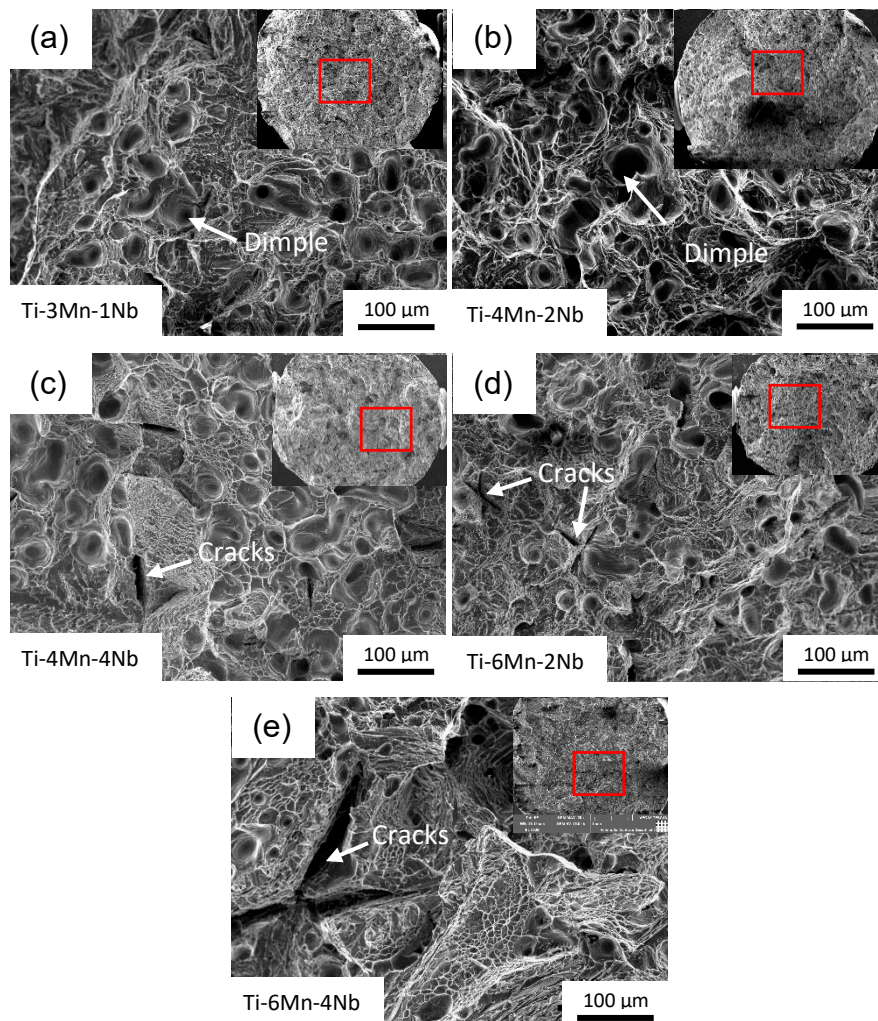


Fig. 5.5-4. SEM images of tensile fracture surfaces (SEM images) of Ti-Mn-Nb alloys fabricated by MIM after tensile failure. (a) - (e) show Ti-3Mn-1Nb; Ti-4Mn-2Nb; Ti-4Mn-4Nb; Ti-6Mn-2Nb and Ti-6Mn-4Nb, respectively. The low-magnification image in the upper right corner of each micrograph shows the location of the micrograph with respect to the specimen cross-section marked by a red rectangle.

In as-sintered Ti-4Mn-2Nb-xY ($x = 0.1, 0.5$) alloy, the morphology of the fracture surface did not change substantially, and it showed still typical features of plastic fracture as visible in Fig.5.4-4. However, on the fracture surfaces of Ti-4Mn-2Nb-0.1Y and Ti-4Mn-2Nb-0.5Y alloy, spherical granular Y_2O_3 particles (discussed in section 6.4) were found. The Y_2O_3 phase seems to exhibit a good bonding with the matrix and does not fall off at the fracture like the carbides

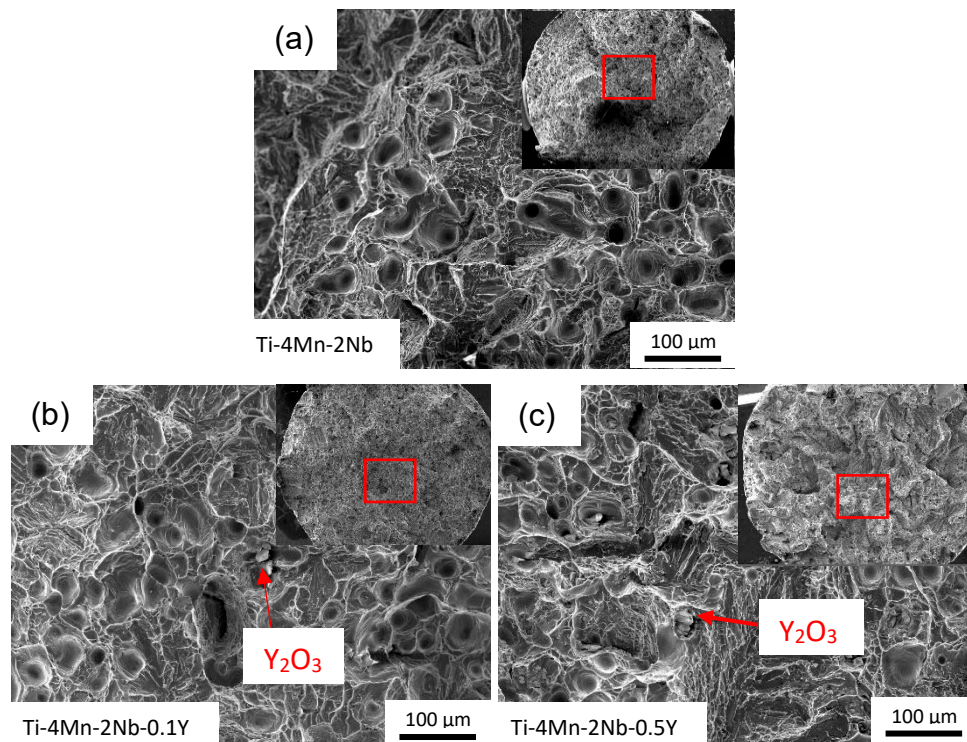


Fig. 5.5-5. SEM images of tensile fracture surfaces (SEM images) of Ti-4Mn-2Nb-xY alloys fabricated by MIM after tensile failure. (a) Ti-4Mn-2Nb, (b) Ti-4Mn-2Nb-0.1Y, (c) Ti-4Mn-2Nb-0.5Y. The low-magnification image in the upper right corner of each micrograph shows the location of the micrograph with respect to the specimen cross section marked by a red rectangle.

5.6 Transmission electron microscopy

Samples fabricated by arc-melting

In the section reporting the mechanical properties of arc-melted Ti-Mn-Nb specimens (Fig. 5.4-3), the elongation of Ti-10Mn-2Nb was significantly decreased compared to the other specimens. This needs to be further investigated. For this aim, TEM experiments were conducted.

5. Results

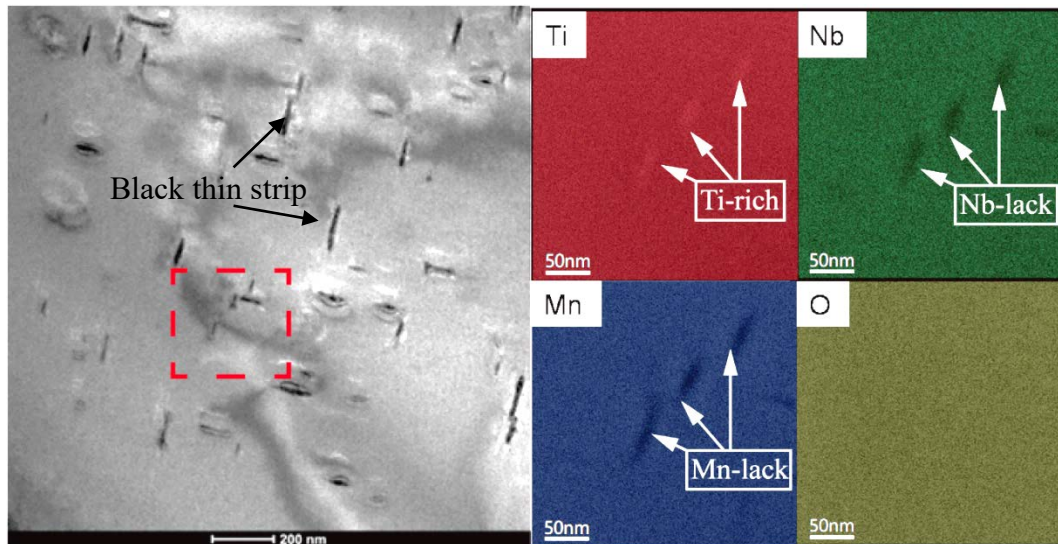


Fig. 5.6-1. Scanning transmission electron microscope (STEM) images of Ti-10Mn-2Nb alloy, with elemental maps (STEM-EDX) of Ti, Nb, Mn and O inside the red dashed lined area.

Fig. 5.6-1 is a STEM-EDX image of Ti-10Mn-2Nb. In the lower magnified overview picture, black thin stripes were observed in the β -Ti matrix. The length of the black stripes is between 100 nm to 200 nm. Due to their small size, they generate no detectable signal in the XRD results. With scanning inside the area enclosed by the red dashed lines, the elemental composition of the matrix and the black stripes of second-phase could be determined. The colors red, green, blue and yellow represent the four elements of titanium, niobium, manganese and oxygen. The brighter the color the higher is the element concentration.

The image of oxygen shows a very evenly distribution and no obvious segregation. This can prove that no formation of oxides occurs. In the STEM-EDX maps of Ti, Nb and Mn, significant segregation in the position of the black stripes of second phase is visible. Ti content is higher than in the matrix, while both Mn and Nb contents reveal lower values. This shows that the black stripes represent a titanium-rich phase with lack of Nb and Mn. In the matrix, the distribution of Ti, Nb and Mn is very even and no segregation can be observed.

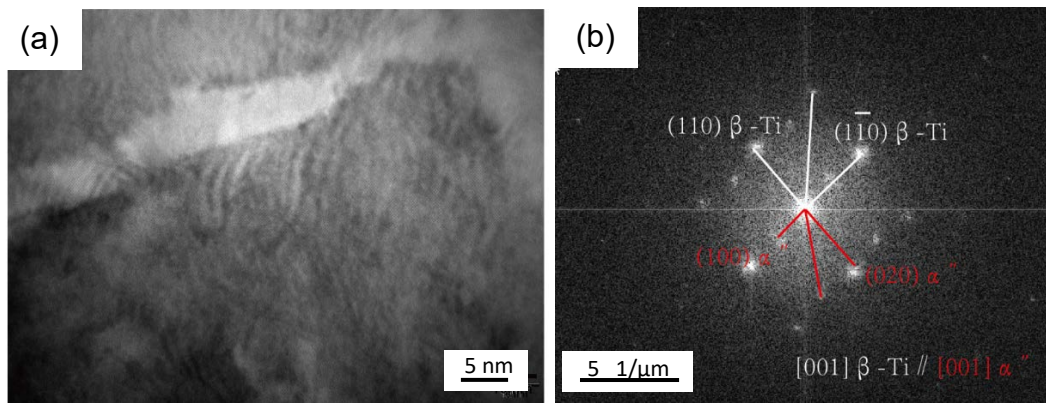


Fig. 5.6-2. TEM images of Ti-10Mn-2Nb alloy, (a) HRTEM image, (b) Fourier transform image.

The second-phase in Fig. 5.6-2 was observed by HRTEM mode and the results are shown in the Fig. 5.6-2 (a). The diffraction pattern shown in Fig. 5.6-2 (b) was obtained by Fourier transformation of Fig. 5.6-2 (a). The two patterns in Fig. 5.6-2 (b) belong to two kinds of structures, which represent β -phase and α'' phase, respectively. The α'' phase belongs to the orthorhombic crystal system, in which its lattice constants are: $a = 4.824 \text{ \AA}$, $b = 4.63 \text{ \AA}$, $c = 3.15 \text{ \AA}$, ($\alpha = \beta = \gamma = 90^\circ$) [14, 117]. It is found that α'' precipitates and β phase satisfy an orientation relationship of $[001]_{\beta\text{-Ti}} // [001]_{\alpha''}$.

Samples fabricated by MIM

In order to investigate the precipitates visible in the MIM material (Fig. 5.2-3 (c)), the as-sintered Ti-4Mn-2Nb (after tensile test, UTS=730 MPa, elongation= 16.2%) were characterized by high-resolution transmission electron microscopy (HRTEM). The bright-field image and HRTEM image are presented in Fig. 5.5-3 (a) and (b), respectively. In Fig.5.5-3 (a), the elongated precipitate (white arrow) is surrounded by the matrix (red arrow). At the junction of the matrix and the precipitate, there are some black stripes that are indicated by the yellow arrow and appear only in the matrix and terminate in the precipitate. High-resolution observation at the phase boundary was performed. In Fig. 5.6-3 (b), different contrasts of two phases can be observed: white matrix and precipitate. In order to determine the phase, three regions were selected to be analyzed which are marked as red frame for the matrix, black frame for the boundary, and white frame for the precipitate.

5. Results

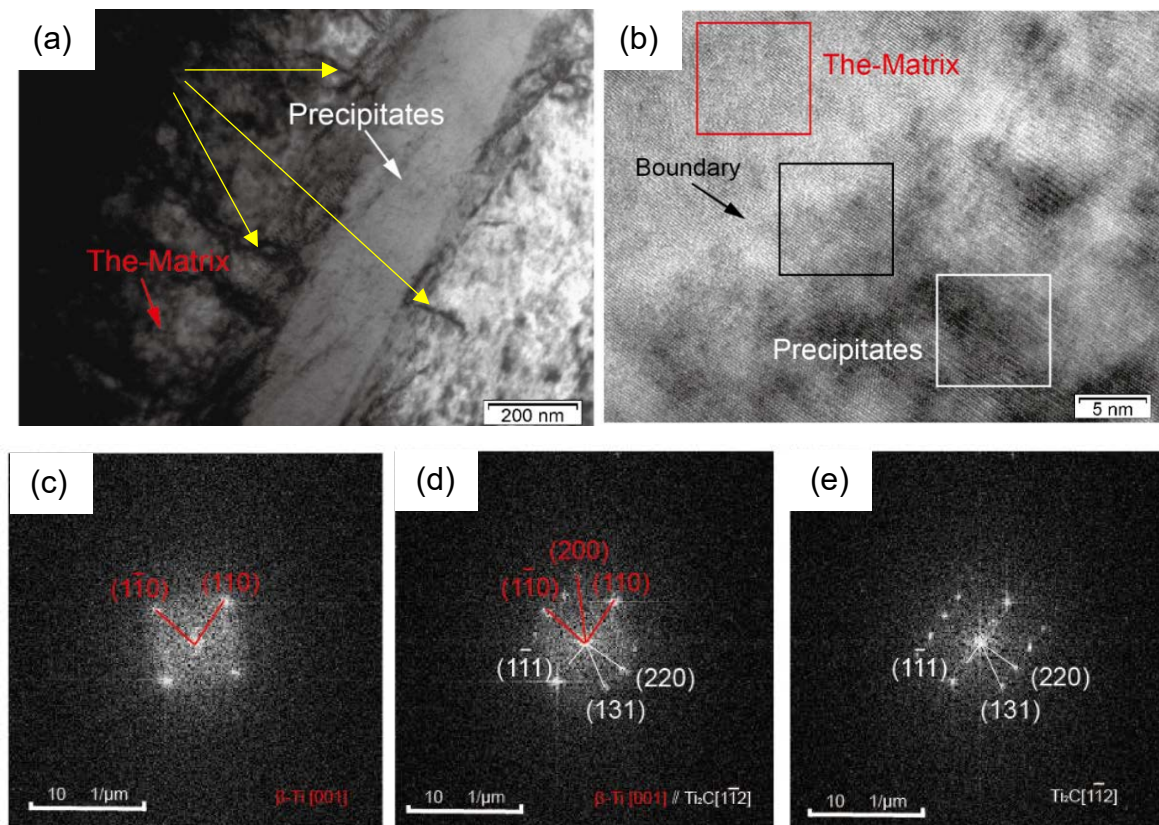


Fig. 5.6-3. TEM images of MIM Ti-4Mn-2Nb alloy; (a) bright-field image, (b) HRTEM image of precipitates, (c)-(e) Fourier transform of frame in Fig. 5.6-3 (b)

Fourier transform images are shown as Fig. 5.6-3 (c), (d) and (e). After calibration, the matrix (in Fig. 5.6-3 (c)) belongs to $\beta\text{-Ti } [001]$. By calibrating and analyzing of Fig. 5.6-3 (e), the image of the precipitate region, it can be determined that the precipitate is Ti_2C . The crystal type of Ti_2C is face-centered cubic (f.c.c.), space group: $Fd\text{-}3m\ O_2\ (227)$, and cell parameters are: $a=b=c=0.86\ \text{nm}$, $\alpha=\beta=\gamma=90^\circ$ [118]. At the boundary, there is an orientation relationship between Ti_2C and $\beta\text{-Ti}$: $[0\ 0\ 1]_{\beta\text{-Ti}} \parallel [1\ \bar{1}\ 2]_{\text{Ti}_2\text{C}}$. Fig. 5.6-3 (d) is a combined diffraction pattern of Ti_2C and $\beta\text{-Ti}$. No diffraction patterns of additional phases were found in the deformed structure of Ti-4Mn-2Nb (after the 16.2% extension,). Thus, the black stripes (yellow arrow) in Fig. 5.6-3 (a) are considered to be dislocation lines.

5.7 Cell biology assessment

In vitro cell culture test is important as a preliminary screening of biological materials [119]. Ti-Mn-Nb alloys could be used as potential implantable bone tissue materials. They are usually tested by osteoblasts such as MG63. MG63 are considered to be representative for osteoblasts [120, 121] and are readily available.

5.7.1 Live/Dead staining

Fig. 5.7-1 shows the viability of MG63 seeded on control groups of different materials. The control group with a cell culture on a glass plate is shown in Fig. 5.7-1 (a). Pure titanium as the best biocompatible metal material [122] [13, 123]. It is also used as a control group shown in Fig. 5.7-1 (b). After 5 days of culture, there are a few dead cells (indicated by red arrows) attached to the surface of the glass disc and pure Ti disc, but cell viability was still greater than 99% (discussed in section 6.5). Fig. 5.7-1 (c) and (d) represent Ti-4Mn and Ti-2Nb alloys, they were set as control groups to compare with the Ti-4Mn-2Nb alloy. The result (Ti-4Mn) as indicated in Fig. 5.7-1 (c) shows lower viability than Fig. 5.7-1 (a) and (b), revealing some dead cells which are dyed red. Fig. 5.7-1 (d) shows that the cell activity is higher than the cell activity in Fig. 5.7-1 (c).

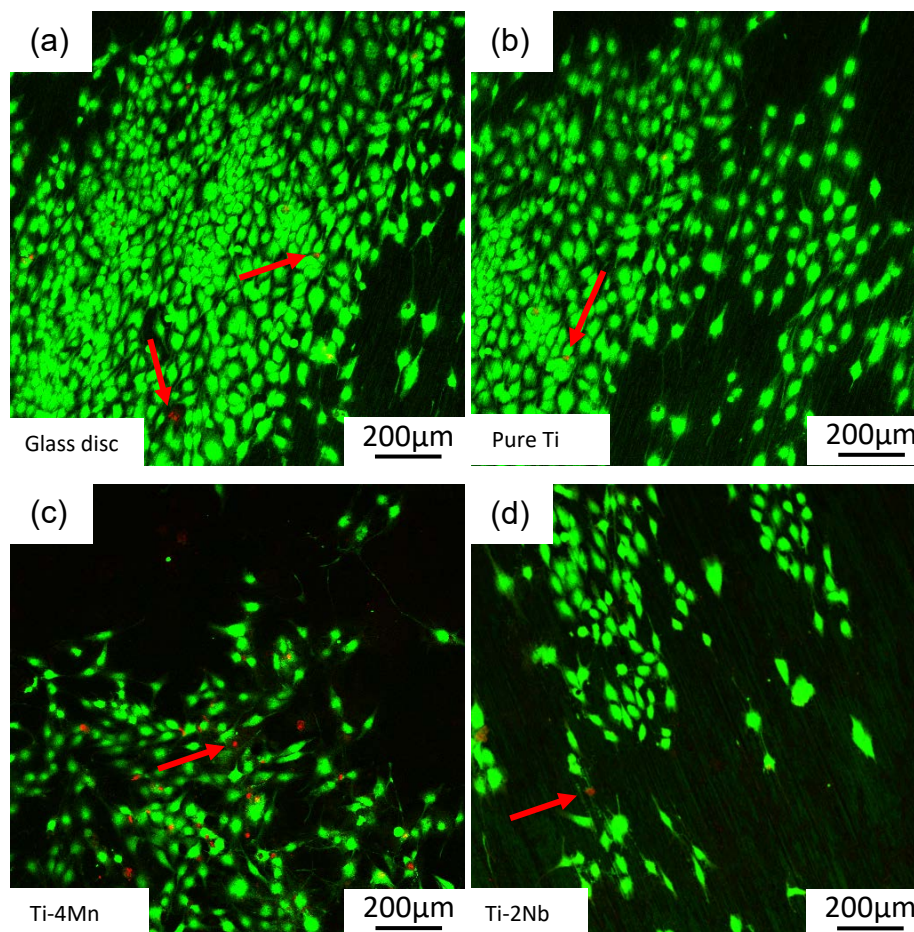
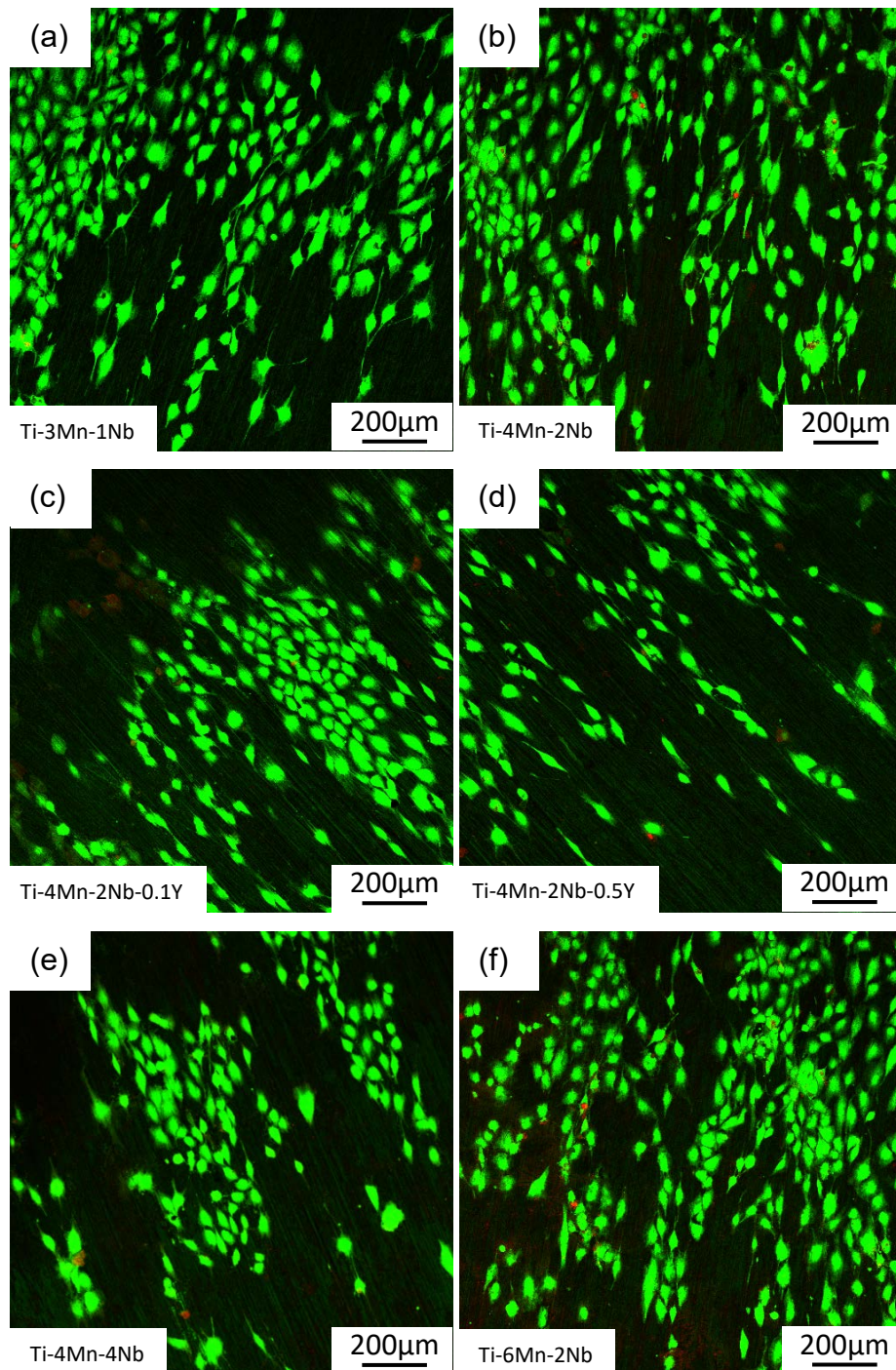


Fig. 5.7-1. Live/dead staining of MG63 on the control groups after 5 days, (a)-(d) representing MG63 cells cultured on a glass disc, pure Ti, Ti-4Mn alloy and Ti-2Nb alloy, respectively

Fig. 5.7-2 shows the images of live/dead stained MG63 cells attached to the surface of Ti-Mn-Nb specimens produced by MIM. MG63 osteoblast cells were cultured on the different Ti alloys to assess the adhesion and cell viability. No obvious difference in the number of viable cells (green) and dead

5. Results

cells (red) in Fig. 5.7-2 is visible at 5 days of culture. Viable cells adhered well to the alloy surface and exhibited normal, healthy osteoblastic spindle-like morphology. The results of live/dead staining show that most MG63 cells on Ti-Mn-Nb alloy (MIM) are alive, and indicate that Ti-xMn-yNb ($x=3, 4, 6$; $y=1, 2, 4$) and Ti-4Mn-2Nb-xY ($x=0.1, 0.5$) alloys are safe and suitable materials for the growth of osteoblasts. However, live/dead staining can only a qualitative but not a quantitative analysis. The supernatant and the cells adhering on the Ti-Mn-Nb alloy surface are still required analysis.



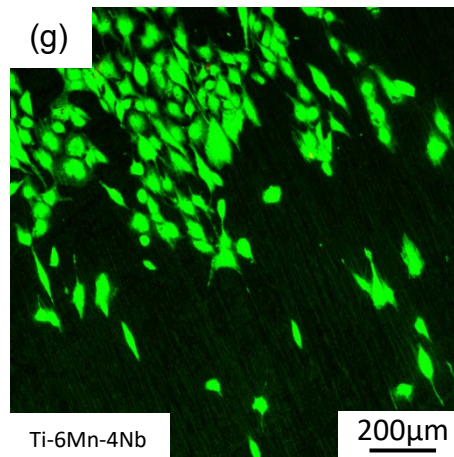


Fig. 5.7-2. Live/Dead staining of MG63 on Ti-Mn-Nb (MIM) specimens after 5 days, (a) representing MG63 cells cultured on Ti-3Mn-1Nb, (b) Ti-4Mn-2Nb, (c) Ti-4Mn-2Nb-0.1Y, (d) Ti-4Mn-2Nb-0.5Y, (e) Ti-4Mn-4Nb, (f) Ti-6Mn-2Nb and (g) Ti-6Mn-4Nb.

5.7.2 Osmolality and pH value

During cell culture, the pH values and osmolality in the supernatant change with cell proliferation and death [124, 125]. At the same time, different alloy ingredients release ions into the supernatant during cell culture, which affects pH and osmolality [126, 127]. Fresh medium (DMEM + 10% FBS) and medium without cell culture in the incubator after 5 days were tested, and the results are shown in the Fig. 5.7-3. They were set as a further control group together with cell control on glass, pure Ti, Ti-4Mn, and Ti-2Nb.

The osmolality indicates the concentration of all solutes [128]. The pH value reveals the concentration of OH^- ions in the supernatant [129, 130]. Both osmolality and pH are important indicators of biocompatibility [131, 132]. For osmolality in Fig. 5.7-3, it is obvious that for alloys comparing with pure medium, once the cell culture is carried out, the number of ions released into the supernatant increases. The highest value of osmolality is observed with Ti-4Mn. With the addition of Nb, the osmolality of the Ti-Mn-Nb ternary alloy is maintained between 0.34 and 0.39 osmol/kg, which is similar to the values of the pure Ti group and the cell control group.

The value of pH in the medium is 7.5 without alloys and cells. Due to the very low degradation rate of titanium alloys [3, 56], the value of pH change is related to cell reproduction and death during cell culture [133, 134]. The pH values of Ti-Mn-Nb ternary alloys are ranging between 7.7 and 8.1. For the Ti-4Mn-2Nb and Ti-4Mn-2N-0.1Y alloys compared with pure Ti group, osmolality and pH value are

5. Results

similar. This means that no factor adverse to cell growth was detected in the supernatant after cell culture.

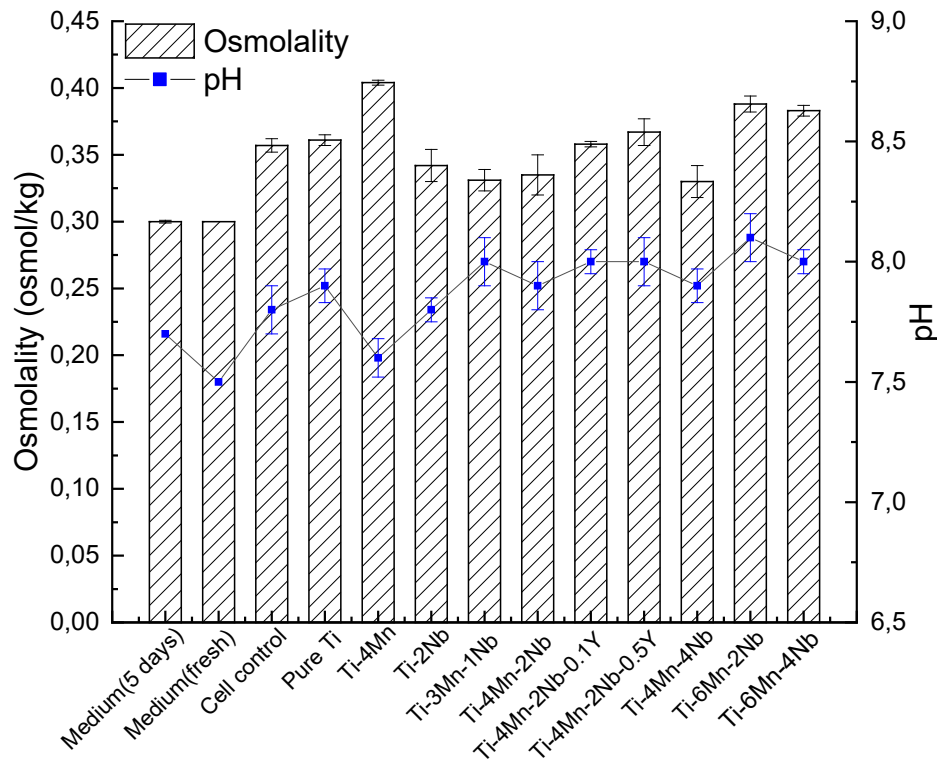


Fig. 5.7-3. Osmolality and pH values of the supernatant by MG63 cells cultured on Ti-Mn-Nb (MIM) alloy and control groups for 5 days

5.7.3 DNA isolation and LDH release

To investigate the cytotoxicity effect of Mn and Nb, respectively, in Ti alloys processed by MIM, the culture supernatants were harvested after incubation for 5 days. Subsequently, the cytotoxicity by different alloys was evaluated by the amount of LDH (lactate dehydrogenase) leakage into the medium. The red dots in Fig. 5.7-4 represent the LDH values (LDH release in cultures pure Ti was set as the control (100%), to which that of the culture with different compositions alloys was normalized.). LDH of Ti-4Mn reached the highest value (128.6%) of all investigated alloys (in Table 5.7-1). The LDH release of cell control is 103.6%. The data can be found in Table 5.7-1, the LDH values of Ti-4Mn-2Nb and Ti-4Mn-2N-0.1Y alloys are 102.7% and 100.1%, respectively. Both of them are similar to the pure Ti. This means, there is no large amount of LDH detected in the supernatant. Thus, it is indicated that the

amount of dead cells during cell culture were substantially identical to the situation on pure titanium. Thus, Ti-4Mn-2Nb and Ti-4Mn-2N-0.1Y alloys did not produce significant cytotoxicity.

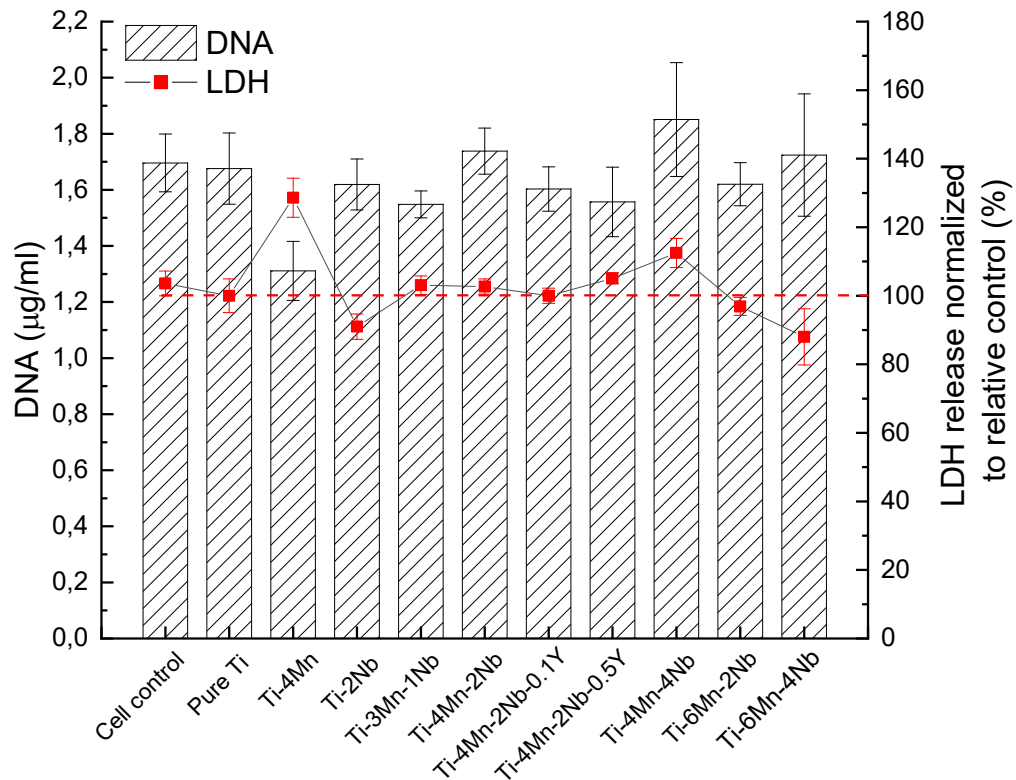


Fig. 5.7-4. Effect of different Ti-Mn-Nb alloys on DNA isolation and LDH assay after 5 days cultured.

LDH release in cultures pure Ti was set as the control (100%), to which that of the culture with different compositions alloys was normalized.

In addition to the analysis of the supernatant, MG63 attached to the surface of the alloy also needs to be investigated. The quantitative analysis of cells was performed by DNA isolation [135, 136]. The data obtained by DNA isolation are listed in Table 5.7-1. It can be clearly seen from Fig. 5.7-4 that the DNA content obtained on Ti-4Mn is the lowest one. Compared with the cell control and pure Ti control group, the DNA contents obtained by Ti-Mn-Nb ternary alloys are basically the same. This means that the number of viable cells adhering to the surface of the alloy for proliferation during cell culture is substantially the same as that for pure titanium.

5. Results

Table 5.7-1. Values of DNA isolation and LDH release (LDH release in cultures pure Ti was set as the control (100%), to which that of the culture with different compositions alloys was normalized).

Alloy	DNA ($\mu\text{g/ml}$)	STDEV ($\mu\text{g/ml}$)	LDH (%)	STDEV (%)
Cell control	1.696	0.103	103.6	3.6
Pure Ti control	1.676	0.127	100	4.9
Ti-4Mn	1.311	0.105	128.6	5.7
Ti-2Nb	1.619	0.091	91.0	3.7
Ti-3Mn-1Nb	1.548	0.048	103.1	2.7
Ti-4Mn-2Nb	1.738	0.082	102.7	2.2
Ti-4Mn-2Nb-0.1Y	1.603	0.079	100.1	2.2
Ti-4Mn-2Nb-0.5Y	1.557	0.124	105.1	1.6
Ti-4Mn-4Nb	1.851	0.203	112.5	4.26
Ti-6Mn-2Nb	1.62	0.077	96.9	2.6
Ti-6Mn-4Nb	1.724	0.218	88.1	8.2

5.8 Corrosion behavior

As a bio-implant material, the corrosion behavior of titanium alloys in body fluids also needs to be considered [137]. After the electrochemical study of the Ti-Mn-Nb (MIM) alloy in the Hanks' balanced salt solution (HBSS), pure titanium (MIM) and Ti-6Al-4V (MIM) were set as the control group for comparison. Pure titanium and Ti-6Al-4V are the first Ti alloys used as human implant materials due to a good corrosion resistance [56, 138, 139].

5.8.1 Potentiodynamic polarization

The results of the polarization measurements on the MIM processed Ti alloys are displayed in Fig. 5.8-1. The curve shows on the right of Fig. 5.8-1 is a schematic diagram of the Tafel region of the pure Ti curve. A distinct linear Tafel region can be observed in the cathodic and anodic regions. Two sets of linear equations are obtained by fitting the linear region, and the intersection point corresponds to the self-corrosion current [140, 141]. The corrosion current density obtained by the Tafel region can represent the corrosion performance of the alloy. The evaluation of all measurements is given in Table 5.8-1. Higher I_{corr} values indicate a less stable oxide layer of the material [142-144]. There are obvious differences between the polarization properties of the Ti-Mn-Nb alloys and the control group of pure titanium and Ti-6Al-4V. The corrosion current density (I_{corr}) is 78.5 nA/cm^2 for the pure Ti (MIM) and

90.3 nA/cm² for Ti-6Al-4V (MIM). The breakdown of the passivation film of the pure titanium is at a lower potential (about 1 V as shown in Fig. 5.8-1). Ti-Mn-Nb alloys and including Ti-6Al-4V did not show this phenomenon in the range from -500mV to 1500mV.

Among the Ti-Mn-Nb alloys, the corrosion current density is 9.9 nA/cm² for Ti-4Mn-2Nb and 19.0 nA/cm² and 29.8 nA/cm² for Ti-4Mn-14Nb and Ti-10Mn-14Nb alloys, respectively. Hence, the corrosion resistance of the Ti-Mn-Nb alloys fabricated by MIM is evidently higher than that of pure Ti and Ti-6Al-4V.

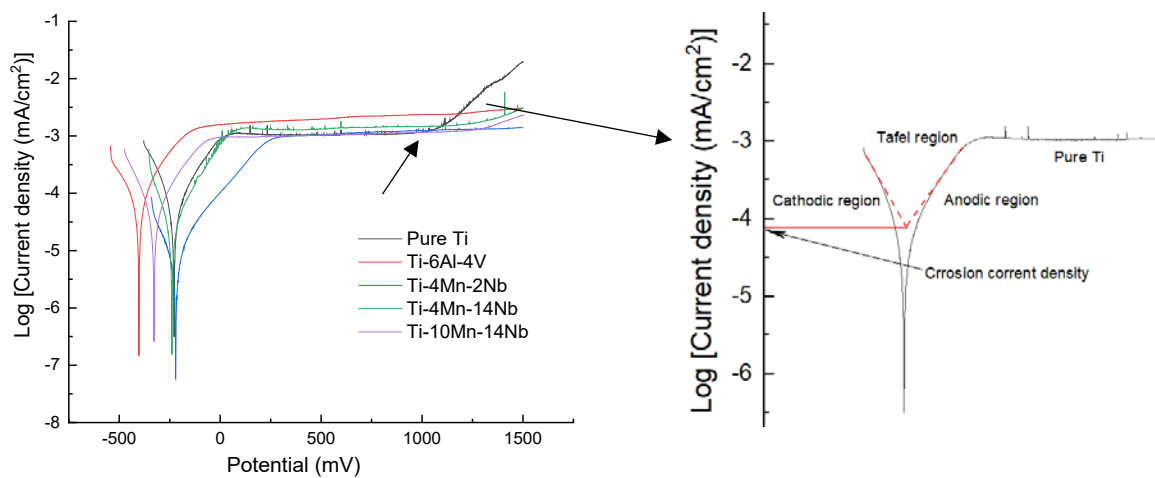


Fig. 5.8-1. Potentiodynamic polarization curves for the Ti-Mn-Nb alloys in HBSS at 37.0°C and schematic diagram of Tafel region of pure Ti curve.

Table 5.8-1. Electrochemical properties of the alloys (MIM) determined from potentiodynamic polarization measurements in HBSS at 37.0 °C

Alloy	Open circuit potential (mV)	Corrosion current (nA/cm ²)
Ti (MIM)	-224.3±13.2	78.5±6.2
Ti-6Al-4V (MIM)	-404.0±15.6	90.3±8.6
Ti-4Mn-2Nb	-221.1±19.5	9.9±5.2
Ti-4Mn-14Nb	-301.4±21.2	19.0±4.1
Ti-10Mn-14Nb	-101.7±11.5	29.8±3.9

The lowest corrosion current was found on Ti-4Mn-2Nb. For possible further improvement the content of Mn and Nb was varied in a certain range. Thus, Ti-xMn-yNb (x=3, 4, 6; y=1, 2, 4) were

5. Results

recorded by potentiodynamic polarization in HBSS at 37.0 °C (Fig. 5.8-2). It can be seen from Table 5.8-2 that the open circuit potential (OCP) calculated from the polarization curves are between 221 mV to 376 mV. Such a difference in the OCP of samples sintered at different temperatures, could be related to the different alloys or microstructure and resulting porosity [138, 145].

The value of the corrosion current was determined according to the Tafel slope evaluation. The corrosion current density was between 8.3 nA/cm² and 9.9 nA/cm². A significant change in the self-corrosion current is not observed within the investigated range of changes in the Mn and Nb contents. Moreover, the self-corrosion current density of Ti-xMn-yNb (x=3, 4, 6; y=1, 2, 4) alloys is smaller than that of pure Ti and Ti-6Al-4V alloy. This means that the MIM Ti-xMn-yNb (x=3, 4, 6; y=1, 2, 4) alloys produced have a better corrosion resistance than MIM pure Ti and MIM Ti-6Al-4V.

Combining the results of mechanical properties and biocompatibility testing, in general, the comprehensive performance of Ti-4Mn-2Nb is well suitable for usage as biomaterial.

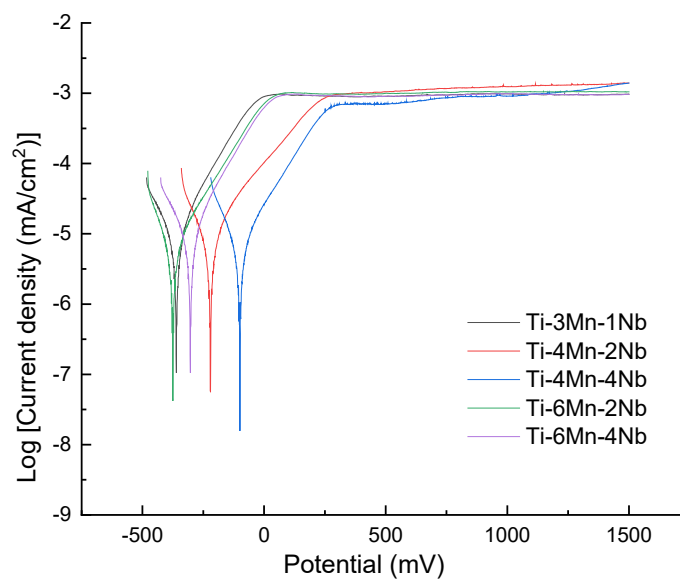


Fig. 5.8-2. Potentiodynamic polarization curves for the Ti-Mn-Nb (MIM) alloys in HBSS at 37.0°C

Table 5.8-2. Electrochemical properties of the Ti-Mn-Nb alloy (MIM) determined from potentiodynamic polarization measurements in HBSS at 37.0 °C

Alloy	Open circuit potential (mV)	Corrosion current (nA/cm ²)
Ti-3Mn-1Nb	-359.9±26.7	9.4±6.2
Ti-4Mn-2Nb	-221.1±19.5	9.9±5.2
Ti-4Mn-4Nb	-328.9±12.6	8.3±5.8
Ti-6Mn-2Nb	-376.9±13.2	9.8±6.3
Ti-6Mn-4Nb	-239.9±20.0	10.2±7.0

With respect to mechanical properties, a small amount of Y addition can improve the ultimate tensile strength and yield strength of the Ti-4Mn-2Nb alloy significantly. The polarization curves of Ti-4Mn-2Nb, Ti-4Mn-2Nb-0.1Y and Ti-4Mn-2Nb-0.5Y are shown in Fig. 5.8-3. Electrochemical parameters including OCP and corrosion current obtained from Tafel curves are presented in Table 5.8-3. The OCP of these three alloys ranged from about 220 mV to 260 mV. At the same time, the difference in corrosion current is also very small, from 7.3 nA/cm² to 9.9 nA/cm². However, as can be seen from Fig. 5.8-3, when the corrosion current is 39.8 nA/cm² (shown as green arrow), the Ti-4Mn-2Nb-0.5Y alloy already begins to passivate. This value is lower than for Ti-4Mn-2Nb and Ti-4Mn-2Nb-0.1Y.

The polarization curves of Ti-4Mn alloy (blue curve) is also shown in Fig. 5.8-3. It can be seen from Table 5.8-3 that the corrosion current (121 nA/cm²) of Ti-4Mn is higher than Ti-4Mn-2Nb (9.9 nA/cm²) alloy. Ti-4Mn alloy will be discussed in section 6.5 (biocompatibility).

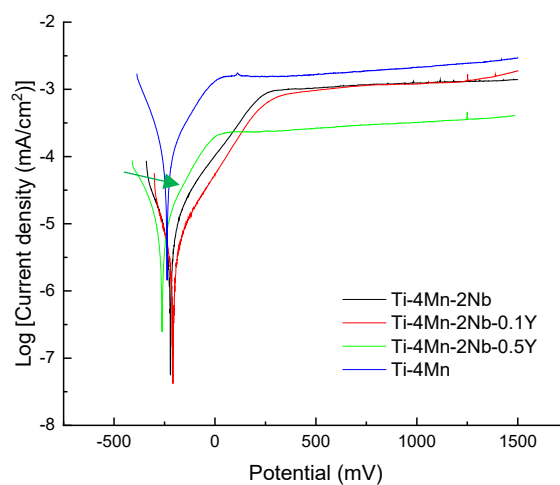


Fig. 5.8-3. Potential–current plots for the Ti-Mn-Nb (MIM) recorded by potentiodynamic polarization in HBSS at 37.0°C

5. Results

Table 5.8-3. Electrochemical properties of the Ti-Mn-Nb alloy (MIM) determined from potentiodynamic polarization measurements in HBSS at 37.0 °C

Alloy	Open circuit potential (mV)	Corrosion current (nA/cm ²)
Ti-4Mn-2Nb	-221.1±19.5	9.9±5.2
Ti-4Mn-2Nb-0.1Y	-260.1±23.6	7.3±3.9
Ti-4Mn-2Nb-0.5Y	-264.5±19.5	8.9±4.6
Ti-4Mn	-230.1±13.1	121.6±6.4

5.8.2 Electrochemical impedance spectroscopy

The results of electrochemical impedance spectroscopy (EIS) measurements are presented by Bode plots. These diagrams for the Ti alloys (MIM) immersed in HBSS at 37 °C for 24 h are shown in Fig. 5.8-4.

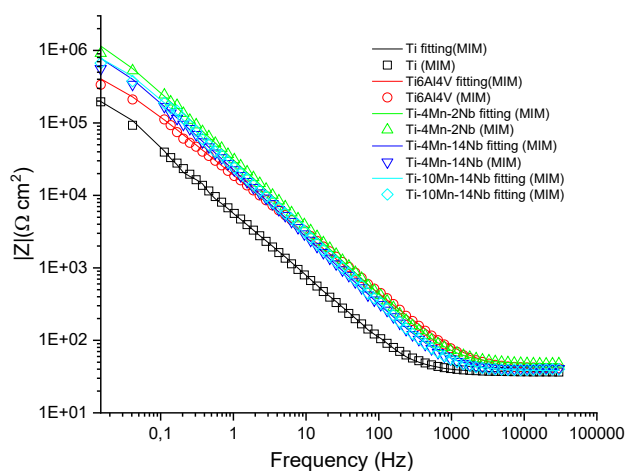


Fig. 5.8-4. Bode plots of Ti-Mn-Nb alloys and control groups (MIM) measured in HBSS at 37 °C after 24 hours immersion time. The solid line represents the fitting result.

In the corrosion process of titanium alloys in HBSS, a dense oxide film layer is formed on the surface in contact with the solution [146, 147], thereby preventing the corrosion from continuing, as shown in Fig. 5.8-5. Based on the EIS features, a simple equivalent circuit shown in Fig. 5.8-5 can be used to simulate this passivation state [148]. The model assumes that the oxide layer formed on titanium alloys consists of one barrier-like layer only.

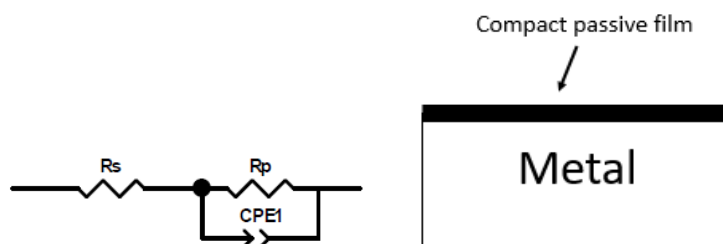


Fig. 5.8-5. Equivalent electrical circuit (for compact passive film) used for fitting modelling the impedance spectroscopy

A simple equivalent circuit with a parallel resistance-capacitance (R_p -CPE) in series with the resistance of solution (R_s) (Fig. 5.8-5) is used to simulate the electrical parameters of the surface. In this circuit, R_s represents the resistance of the electrolyte, R_p is the polarization resistance and CPE (constant phase element) is the specific double-layer capacitance at the working electrode/electrolyte interface [148]. The chi-square (χ^2) values in order of 10^{-3} indicate the good quality of fitting with the data well-adjusted to the proposed equivalent circuit (Table 5.8-4).

The R_p and CPE data are shown in Table 5.8-4. Higher R_p values indicate higher corrosion resistance [149, 150]. A constant phase element (CPE) was used to improve the fitting quality instead of the ideal capacitance due to the distribution of relaxation times originating from the surface heterogeneity [139]. The lower the CPE value the closer is the real situation to an ideal capacitor [151]. The electrochemical parameters obtained by fitting the EIS data are presented in Table 5.8-4, too. The good quality of fitting judged by the quite small chi-square values (χ^2) suggests the validity of the obtained parameters [152].

In Table 5.8-4, the R_p value of the simulated Ti-Mn-Nb alloy is significantly higher than that of pure titanium and Ti-6Al-4V. This is consistent with the conclusions drawn from the polarization curves in Fig. 5.8-4.

5. Results

Table 5.8-4. Fitting parameters for the MIM-produced Ti alloys measured in 37°C HBSS after 24 hours.

Alloy (MIM)	$R_s(\Omega \text{ cm}^2)$	$R_p(\Omega \text{ cm}^2)$	CPE-T(Fcm^{-2})	CPE-P(Fcm^{-2})	Chi-squared
Pure-Ti	39±0.3	4.2E5±1E4	8.0E-06 ±9E-08	0.92±0.002	0.0012
Ti-6Al-4V	37±0.6	6.8E5±3E4	1.0E-05 ±1E-07	0.82±0.003	0.0035
Ti-4Mn-2Nb	47±0.2	1.9E6±9E4	5.8E-06 ±1E-07	0.93±0.003	0.0038
Ti-4Mn-14Nb	43±0.6	1.1E6±9E4	8.5E-06 ±9E-08	0.92±0.003	0.0035
Ti-10Mn-14Nb	38±0.9	1.0E6±8E4	9.5E-06 ±9E-07	0.89±0.003	0.0046

In the study of the corrosion behavior of Ti-xMn-yNb ($x=3, 4, 6$; $y=1, 2, 4$) alloys, the simulation data of Bode plots are analyzed (Fig. 5.8-6). The value of Chi-square is approximately 10^{-3} (Table 5.8-5), indicating a good match between the simulated data and the experimental values. In terms of R_p value, Ti-xMn-yNb ($x=3, 4, 6$; $y=1, 2, 4$) alloys are in the order of 10^6 . This is a very high impedance value, which represents a very high film resistance of the alloy.

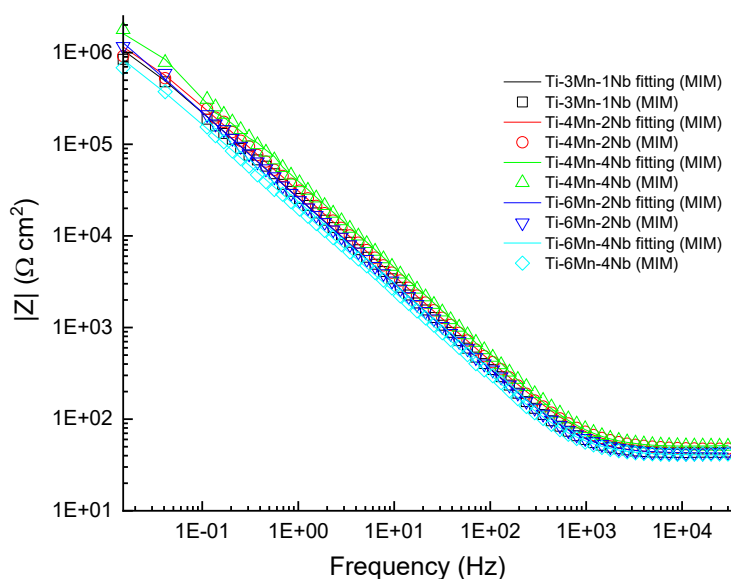


Fig. 5.8-6. Bode plots of Ti-xMn-yNb ($x=3, 4, 6$; $y=1, 2, 4$) measured in HBSS at 37 °C after 24 hours.

The solid line represents the fitting result

Table 5.8-5. Fitting parameters of Bode for the MIM-produced Ti-xMn-YNb (x=3, 4, 6; y=1, 2, 4) measured in 37 °C HBSS.

Alloy (MIM)	R_s (Ω cm ²)	R_p (Ω cm ²)	CPE-T (Fcm ⁻²)	CPE-P (Fcm ⁻²)	Chi-squared
Ti-3Mn-1Nb	41±0.6	1.9E6±9E4	7.0E-06 ±1E-07	0.91±0.003	0.0025
Ti-4Mn-2Nb	47±0.2	1.9E6±9E4	5.8E-06 ±1E-07	0.93±0.003	0.0038
Ti-4Mn-4Nb	43±0.4	3.7E6±1E5	6.9E-06 ±9E-08	0.94±0.002	0.0024
Ti-6Mn-2Nb	39±0.6	5.9E6±2E5	7.1E-06 ±2E-08	0.96±0.002	0.0019
Ti-6Mn-4Nb	38±0.7	2.2E6±1E5	9.1E-06 ±1E-07	0.90±0.003	0.0030

With the addition of Y, the performance of Ti-4Mn-2Nb-xY (x=0.1, 0.5) has not been significantly affected. In the Bode diagram, the curves are the same (Fig. 5.8-7), and the R_p value (Table 5.8-6) of the equivalent circuit is not much different (from 1.9E6 to 3.5E6). In general, this is consistent with the conclusions obtained from the polarization curve shown in Fig. 5.8-7.

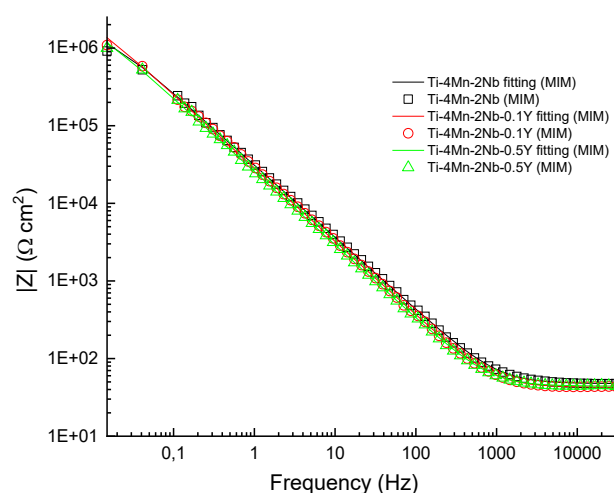


Fig. 5.8-7. Bode plots of Ti-4Mn-2Nb-xY (x=0.1, 0.5) measured in HBSS at 37 °C after 24 hours. The solid line represents the fitting result

Table 5.8-6. The fitting parameters of Bode for the MIM-produced Ti-4Mn-2Nb-xY (x=0.1, 0.5) measured in 37 °C HBSS after 24 hours.

Alloy (MIM)	R_s (Ω cm ²)	R_p (Ω cm ²)	CPE-T (Fcm ⁻²)	CPE-P (Fcm ⁻²)	Chi-squared
Ti-4Mn-2Nb	47±0.2	1.9E6±9E4	5.8E-06 ±1E-07	0.93±0.003	0.0038
Ti-4Mn-2Nb-0.1Y	43±0.3	3.5E6±2E5	8.2E-06 ±2E-07	0.92±0.003	0.0022
Ti-4Mn-2Nb-0.5Y	40±0.6	2.7E6±1E5	6.0E-06 ±3E-07	0.98±0.003	0.0042

6. Discussion

In order to obtain a low-cost bio-titanium alloy providing good mechanical properties, a new β -titanium alloy was developed by using the β -stabilizing elements manganese and niobium. Thus, Ti-Mn-Nb alloys were designed in this study and by two methods: arc-melting and metal injection moulding.

6.1 Determine suitable Ti-Mn-Nb alloy compositions by arc melting

Element Mn

Due to the arc-melting process the Ti-Mn-Nb specimens obtained are rapidly cooled from a high temperature of above 2000 °C and a large number of dendrites are generated inside the structure [153], which may cause instability of mechanical properties [154]. Therefore, prior to further studies, the alloy was heat treated at 900 °C for 1 hour with argon protection, and then rapidly cooled to room temperature, in order to obtain a single β -phase microstructure.

When the Mn content is 16%, the alloys (Ti-16Mn- γ Nb ($\gamma=2, 8, 14$) alloys) precipitate the TiMn phase (Fig. 5.2-2 and Fig. 5.3-2), which results in a brittle fracture of the specimens with its typical features of transgranular cleavage (exhibited in Fig. 5.5-2).

Fig. 6.1-1 shows the influence of 4% and 10% Mn on mechanical properties. The alloys exhibit single β -phase (confirmed in section 5.2 and 5.3) microstructures without other phases. There is no significant difference in grain size (shown in section 5.2.1). It can be seen that UTS and YS of alloys with 10% Mn are both higher than that of alloys containing 4% Mn, indicating that the effect of Mn on tensile strength is significant. The solid solution hardening effect of Mn is stronger than that of most other β stabilizing elements [155].

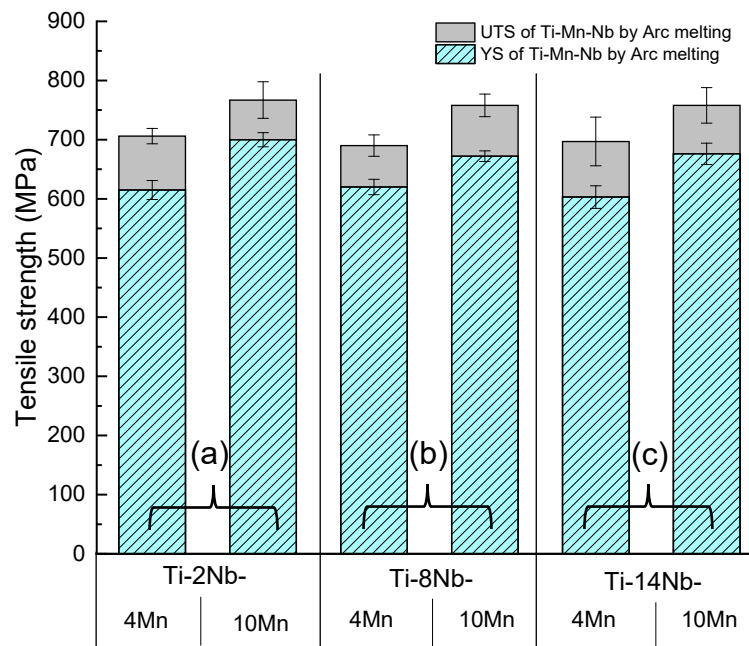


Fig. 6.1-1. Ultimate tensile strength (UTS) and yield strength (YS) of Ti-Mn-Nb alloys produced by arc-melting after solution treatment; Fig. 6.1-1 is divided into 3 parts: (a) Ti-xMn-2Nb (x=4, 10) alloy, (b) Ti-xMn-8Nb (x=4, 10) alloy, (c) Ti-xMn-14Nb (x=4, 10) alloy.

According to reports, the addition of Mn can significantly reduce the lattice constant of β -Ti [34, 156]. The Mn and Nb atoms do not act as interstitial atoms (due to their physical properties). Fig. 6.1-2 is a schematic diagram of the β -Ti (001) crystal plane after some Ti is replaced by Mn and Nb atoms. It can be seen from Fig. 6.1-2 that when the Mn atom is substituted for the Ti atom, the lattice shrinks due to the lattice distortion (shown by the red dotted line in Fig. 6.1-2). When deformation occurs, dislocations move, due to application of external stress. In the volumes of the crystal distorted by the atoms of Mn or Nb additional stresses act on the dislocations resulting in an increase in the strength of the alloy. However, this is not only related to the difference in atomic radius but also some other chemical and physical differences like the relative atomic valence between the elements [157].

6. Discussion

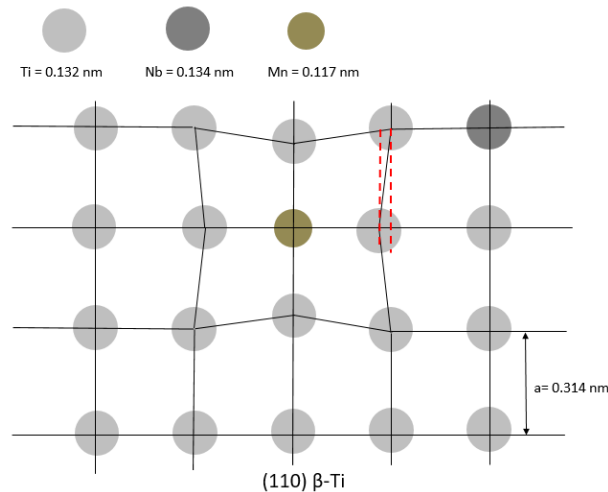


Fig. 6.1-2. Simulation schematic arrangement of Nb atoms and Mn atoms in β -Ti (001)

For elongation (Fig. 6.1-3), the effect of increasing Mn content is not obvious (stays at around 9%) with the same content of Nb. However, in a special case, the elongation of the Ti-10Mn-2Nb alloy is significantly reduced.

This phenomenon is quite special and needs to be further discussed. As result from section 5.5 (TEM result), α'' phase is observed in the Ti-10Mn-2Nb alloy. The transient α'' phase is usually produced during fast-cooling of near- β -Ti alloys and has an effect on the mechanical properties [18]. During the stretching by the tensile load, a large number of slip systems is activated and the alloy is deformed by the slip of the dislocations. However, when a large number of α'' particles appear, dislocation movement through α'' phase will be difficult. As the orthorhombic crystal structure of the α'' phase contains fewer slip systems than the bcc crystal structure of the β phase [158, 159], the stress required for the plastic deformation of the α'' phase is higher than that for the β matrix [160]. This causes the elongation of the alloy to decrease. Due to the large accumulation of dislocations, this can increase the tensile strength. However, a large number of dislocations may also cause the formation of cracks at α'' particle interfaces and reduces the elongation. Overall, the mechanical properties of the alloy show a significant decrease in elongation.

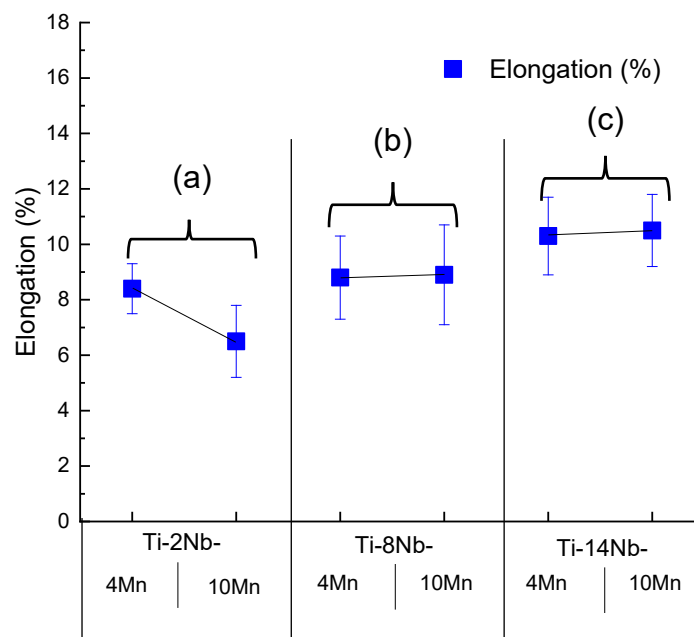


Fig. 6.1-3. Elongation of Ti-Mn-Nb alloy produced by arc-melting after solution treatment; Fig. 6.1-2 is divided into 3 parts: (a) Ti-xMn-2Nb ($x=4, 10$) alloy, (b) Ti-xMn-8Nb ($x=4, 10$) alloy, (c) Ti-xMn-14Nb ($x=4, 10$) alloy.

Element Nb

Fig. 6.1-4 shows the effect of changes in Nb content on the tensile properties of the Ti-Mn-Nb alloys, while the Mn content is kept constant. It can be clearly seen from Fig.6.1-3 that the effect of Nb on UTS and YS is not obvious for both contents of Mn. It can be seen from the microstructure and XRD (section 5.1 and 5.2) that the alloys obtained here have a β single-phase microstructure. As the Nb content increases, the grain size of the alloy does not change significantly. Since the radius of the Nb atom is nearly the same as the radius of the Ti atom [2, 46] and total dissolution in β -phase is possible [51] the Nb atom can easily replace the Ti atom in β -Ti without causing significant lattice distortion. Therefore, it has little effect on the tensile strength of the alloys.

6. Discussion

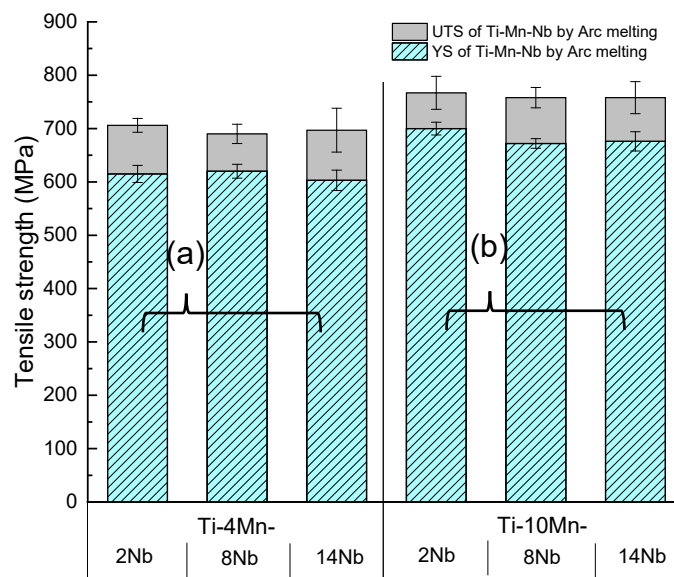


Fig. 6.1-4. Ultimate tensile strength (UTS) and yield strength (YS) of Ti-Mn-Nb alloys produced by arc-melting after solution treatment; Fig. 6.1-3 is divided into 2 parts: (a) Ti-4Mn-yNb (y=2, 8 and 14) alloy, (b) Ti-10Mn-yNb (y=2, 8 and 14) alloy.

However, Nb has a certain effect on the elongation, as shown in Fig. 6.1-5. When the Nb content increases, as shown in (a) and (b), the elongation tends to increase. The Nb atom is in solid-solution in the β -Ti matrix and does not cause lattice distortions [51], which is different from Mn. Therefore, the Nb element has little effect on the strength but can increase the elongation to some extent. The alloys belong to the β single-phase structure, and there is no obvious grain refinement phenomenon by Nb content increased. Thus, Nb seems to introduce new slip systems in Ti-Mn-Nb ternary alloys or activate them at least. Meanwhile, with the addition of Nb (with Mn held constant), the hardness of the alloy shows a downward trend in the hardness tests (Fig. 5.4-1). This also may cause an increase in elongation. Although this is not necessarily related, such an inverse correlation between hardness and elongation is frequently found.

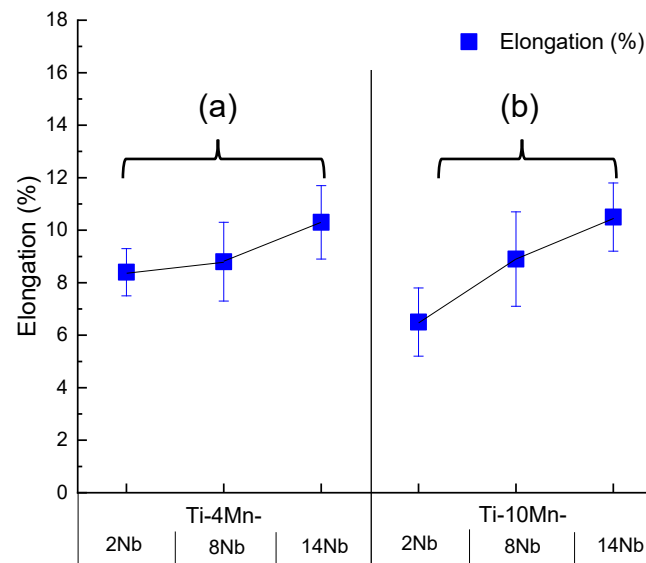


Fig. 6.1-5. Elongation of Ti-Mn-Nb alloys produced by arc-melting after solution treatment; Fig. 6.1-4 is divided into 2 parts: (a) Ti-4Mn-yNb ($y=2, 8,$ and 14) alloy, (b) Ti-10Mn-yNb ($y=2, 8,$ and 14) alloy.

In summary, by arc-melting, Ti-Mn-Nb alloys are fabricated. With the addition of Mn and Nb, the mechanical properties were analyzed and the effects of Mn and Nb in the Ti-Mn-Nb alloys were listed (Table 6.1-1). This can clearly demonstrate the effect (+: improve, 0: no effect, -: decrease) of Mn and Nb alloying elements on tensile strength and elongation.

The alloy group is screened by comparing the arc-melted specimens. Ti-xMn-yNb ($x=4, 10;$ $y=2, 8, 14$) alloys show good mechanical properties. Therefore, in the next study, the alloys in this composition range were prepared and analyzed by the MIM method.

Table 6.1-1. Effects of Mn and Nb elements in the Ti-Mn-Nb alloy

Mechanical property	Mn (at.%)		Nb (at.%) 2%, 8%, 14%
	4%, 10%	16%	
Performance of tensile strength	+	-	0
Performance of elongation	0	-	+

6.2 Analysis of sintered alloys

6.2.1 Density

After screening the alloy compositions by investing arc melted specimens, it was found that Ti-xMn-yNb ($x=4, 10$; $y=2, 8, 14$) alloys have good mechanical properties. The density of sintered Ti-Mn-Nb alloys (Nb content lower than 14%) was found to be about 97% (Fig. 5.2-7). However, the density of Ti-4Mn-14Nb and Ti-10Mn-14Nb alloys remained at around 94.5%.

During the sintering process, the state of the Mn powder is completely different from that of the Ti and Nb powders. The melting points of Ti (1668 °C) and Nb (2468 °C) are much higher than the sintering temperature of 1500 °C applied in this study. The melting point of Mn is 1244 °C and the boiling point (standard atmospheric pressure) is 1962 °C [65] which is shown in Fig. 6.2-1. At the sintering temperature (1500 °C) Mn is in a liquid state. However, the vapor pressure of the Mn is rather low: 0.1 kPa at 1269 °C and 1 kPa at 1439 °C [161]. That is much higher than the vapor pressures of Ti (0.1 kPa at 2160 °C) and Nb (0.1 kPa at 3260 °C) at 1269 °C (as shown in Fig. 6.2-1).

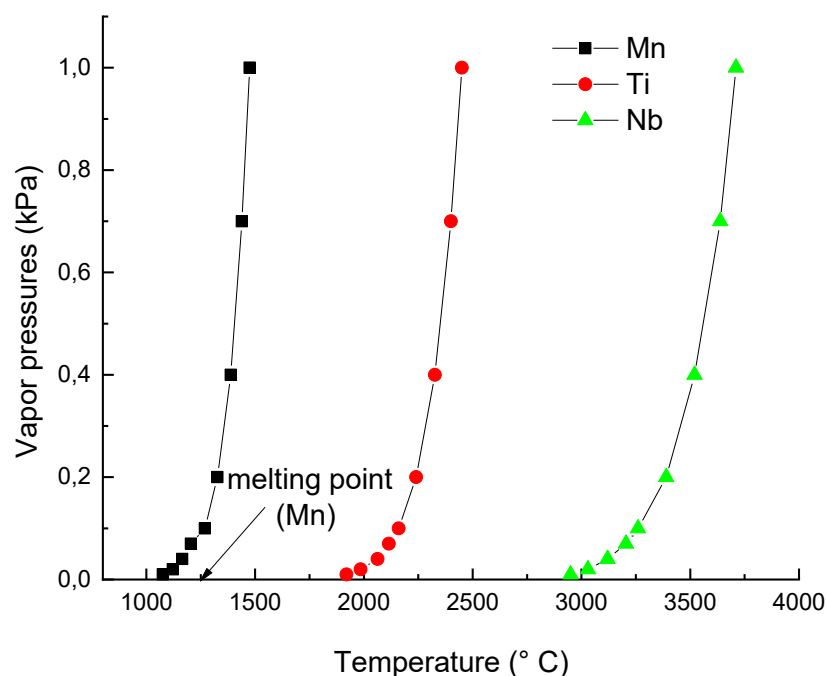


Fig. 6.2-1. Vapor pressures of Mn, Ti and Nb [65]

It can be assumed that transportation of Mn via the gas phase and liquid phase are the major diffusion mechanisms during sintering. The Mn atoms melt from the solid state to a liquid state when sintered at temperatures over 1244 °C. Next, when the temperature rises to 1269 °C, significant amounts of Mn begin to vaporize, this means Mn sublimates from the solid state to a gaseous state. Both gas and liquid have good diffusivity and liquidity. Therefore, Mn either in the form of liquid or gas will surround the Ti and Nb powder particles. It is advantageous for sintering, and the illustration schematic of heating process is as follows in Fig. 6.2-2.

When Nb content reaches 14% (at.%), due to the diffusion rate of Nb is slow [162, 163], it is not conducive to solid-state sintering. That is why the density of Ti-4Mn-14Nb and Ti-10Mn-14Nb is lower. With the addition of the Y element, the resulting Y_2O_3 particles have a high melting point[164], which hinders the sintering [165] of the alloy, but can reduce the grain size (discuss in section 6.4).

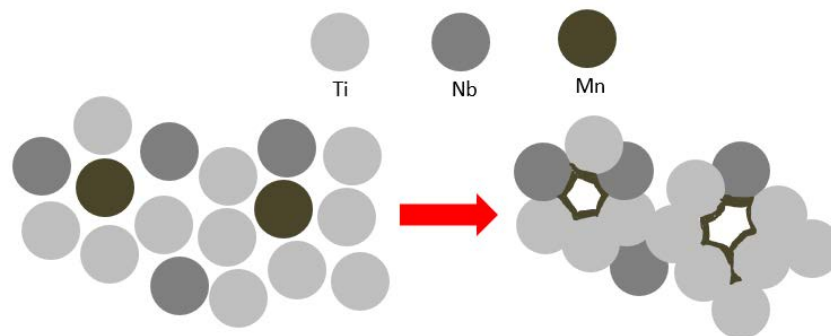


Fig. 6.2-2. Schematics of the heating process

6.2.2 Young's modulus

The sintered Ti-Mn-Nb alloys exhibit about 70-100 GPa Young's modulus which is shown in section 5.2.3. It is well known that Young's modulus is one of the intrinsic parameters of materials, because it is determined by the bonding force among atoms. This bonding force is not only related to the crystal structure but also to the distances among atoms, and it can be affected by alloying additions [166-168]. Furthermore, Young's modulus is not sensitive to the grain size [167, 169]. It is only related to the material. As reports that it is sensitive to the α/β ratio of titanium alloys[49, 170]. According to literature data, the β phase has the lowest Young's modulus in titanium alloys, followed by α'' , α , α' and ω , and the ω phase has the highest [149, 161, 162]. The trend of Young's modulus (Fig. 5.2-7) is related to the α/β fraction (Fig. 5.2-6).

6. Discussion

The density of β -Ti (b.c.c. structure) is 68%, and the density of α -Ti (h.c.p. structure) is 74% [18]. This means the interatomic bonding force of β -Ti is smaller than that of α -Ti [171]. When β -Ti is mechanically stressed, the distance between the atoms is modified with less force than for α -Ti. Before plastically yielding, the smaller force can produce a deformation. That is why β -Ti exhibits a lower Young's modulus. This also can be proved by d-electrons alloy theory [171, 172].

The lowest modulus is about 72 ± 5 GPa being the both of Ti-4Mn-14Nb and Ti-10Mn-14Nb alloys (shown in Fig. 5.2-7). This is due to the total amount of Mn and Nb in these alloys being higher than in other Ti-Mn-Nb alloys in this study. Mn and Nb belong to β stabilizing element in titanium alloys, which could cause retained β -phase at room temperature (in Fig. 5.2-6). Since the Young's modulus of the β -phase is lower than the α -phase [173, 174], the modulus of the other Ti-Mn-Nb alloys which consist of $\alpha+\beta$ are between 80 GP to 95 GPa. They are higher than Ti-4Mn-14Nb and Ti-10Mn-14Nb alloys, however, they are also lower than the one of the traditional biomaterial Ti-6Al-4V (110 GPa).

6.3 The influence of Mn and Nb content on microstructure and mechanical properties of Ti-Mn-Nb alloys

6.3.1 The influence on α/β phase and average grain size

In order to compare with the arc melted specimens the chosen alloy compositions of Ti-4Mn-2Nb, Ti-4Mn14Nb, and Ti-10Mn-14Nb are the same in case of the MIM fabricated samples. The sintered Ti-4Mn-2Nb alloy (slow cooled) exhibits an $\alpha+\beta$ structure and good mechanical properties (section 5.4.3). Slow and intermediate cooling rates lead to a diffusion-controlled nucleation and growth process of α -lamellae into the β -grains. High cooling rates result in a martensitic transformation of the β -phase [175, 176]. In general, at slower cooling rates, i.e. < 20 °C/s, during $\beta\rightarrow\alpha$ transformation diffusional α formation was confirmed [177].

In the beginning, α phase first precipitates at the β phase boundary. Then it precipitates from the β -matrix, in accordance with the Burgers orientation $(110)_\beta // (0002)_\alpha$, $[111]_\beta // [1120]_\alpha$ relationship between α - and β -Ti [178]. Titanium alloys with lamellar structured $\alpha+\beta$ phase can obtain different mechanical properties by adjusting the phase volume fraction of α/β . Therefore, the Mn and Nb contents should be adjusted to obtain Ti-Mn-Nb alloy with better mechanical properties. The important parameters for a lamellar structure with respect to mechanical properties are the β -grain size, size of the colonies of α -phase lamellae and the thickness of the α -lamellae.

Grain size is also an important parameter, which can affect the mechanical properties of alloys [175, 179]. The average of β grain size (AGS) of as-sintered alloys measured after etching is shown in Fig. 6.3-1. It is well known that in single-phase polycrystalline metallic alloys, the yield strength (σ_y) is related to the grain size (d) through the Hall-Petch (H-P) equation [180]: $\sigma_y = \sigma_0 + kd^{-1/2}$, where σ_0 is the starting stress for dislocation movement and k is the unpinning constant. There have been some efforts to apply the H-P relation, initially developed for single-phase alloys, to alloys containing two ductile phases such as various two-phase titanium alloys [180-182].

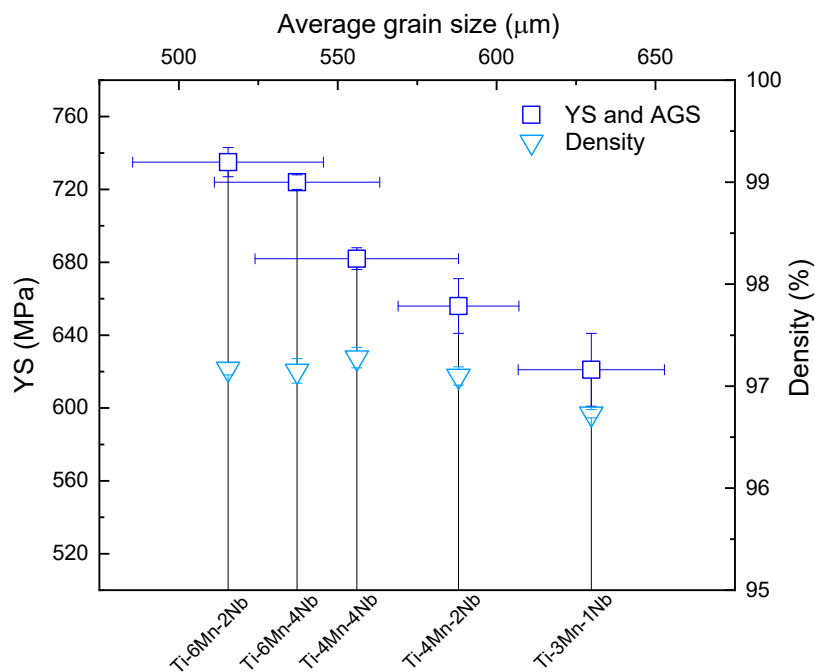


Fig. 6.3-1. Variation of yield strength (YS) versus average grain size (AGS) for Ti-Mn-Nb alloys showing Hall-Petch relationship and density of alloys.

Since the Ti-4Mn-14Nb and Ti-10Mn-14Nb alloys are brittle and could not be deformed up to the yield point in the mechanical tests, they will not be discussed here. Generally speaking, the density of sintered alloys also has an effect on the tensile strength. However, the density of the Ti-xMn-yNb ($x=3, 4, 6$; $y=1, 2, 4$) alloys is maintained at 97%, so the differences in density are negligible. It can be seen from Fig. 6.3-1, for Ti-xMn-yNb ($x=3, 4, 6$; $y=1, 2, 4$) alloys, that the average grain size of Ti-3Mn-1Nb is the largest (about 630 μm) and the one of Ti-6Mn-2Nb is the smallest (about 520 μm). The yield strength of alloys is increasing with decreasing grain size, this trend is consistent with the Hall-Petch relationship, where yield strength is in inverse proportion with grain size [183, 184].

6.3.2 The influence of interstitial elements on MIM Ti-Mn-Nb alloys

Ti-4Mn-2Nb, Ti-4Mn-14Nb and Ti-10Mn-14Nb alloys exhibit sound tensile strength (about 700 MPa to 750 MPa) and elongation (8%-11%) in the arc-melted and heat treated state. The microstructure of them all belongs to the single β -phase type. However, these three alloys fabricated by MIM exhibit different microstructures despite having the same composition as the arc melted variants. E.g. MIM Ti-4Mn-2Nb consists of lamellar α + β structure. Thus, the two fabrication methods can lead to totally different mechanical properties of the same alloy as shown in Fig. 6.3-2.

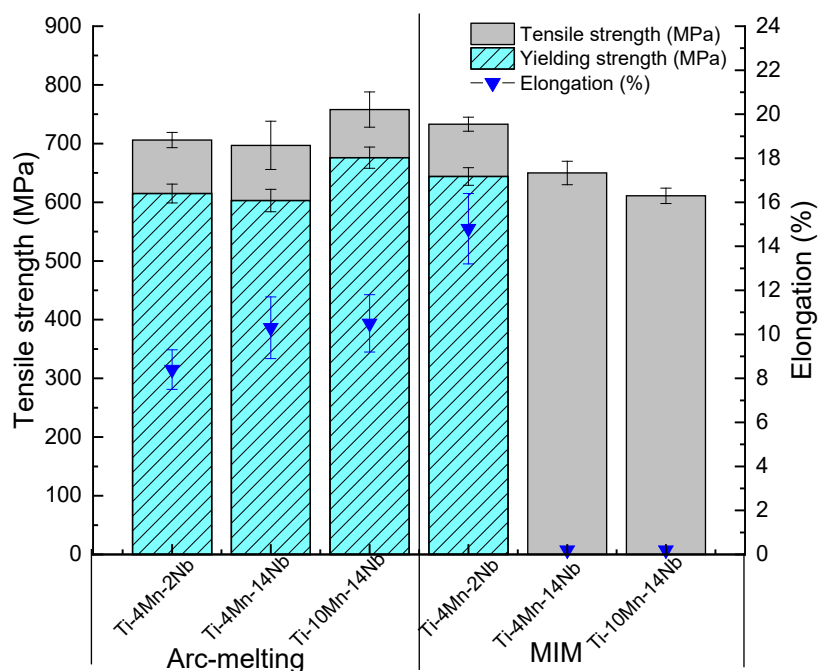


Fig. 6.3-2. Ultimate tensile strength (UTS), yield strength (YS) and elongation to fracture of Ti-4Mn-2Nb, Ti-4Mn-14Nb and Ti-10Mn-14Nb alloys fabricated by arc-melting and MIM

As visible in Fig. 6.3-2, there is no ductility of sintered Ti-4Mn-14Nb and Ti-10Mn-14Nb alloys. This is different from sintered Ti-4Mn-2Nb. Ti-4Mn-14Nb and Ti-10Mn-14Nb broke without yielding. In the MIM process, even the slow cooling rate cannot promote β -phase decomposition into α -phase when the amount of β -stabilizers is too high. Ti-4Mn-14Nb and Ti-10Mn-14Nb alloys show single- β -phase microstructure, which is the same as the ones fabricated by arc-melting (900 °C X 1 h WQ). However, mechanical performance is totally different. This is due to the interstitial elements introduced by the MIM processing. The interstitial elements, e.g. carbon, as a typical α stabilizer element, have a lower solubility in β -Ti than in α -Ti [108, 185]. This causes the interstitial elements to precipitate in the form

of compounds such as a Ti_2C (shown in Fig. 5.3-3 in section 5.3). Due to the brittleness of Ti_2C , the mechanical properties of the matrix are degraded [104].

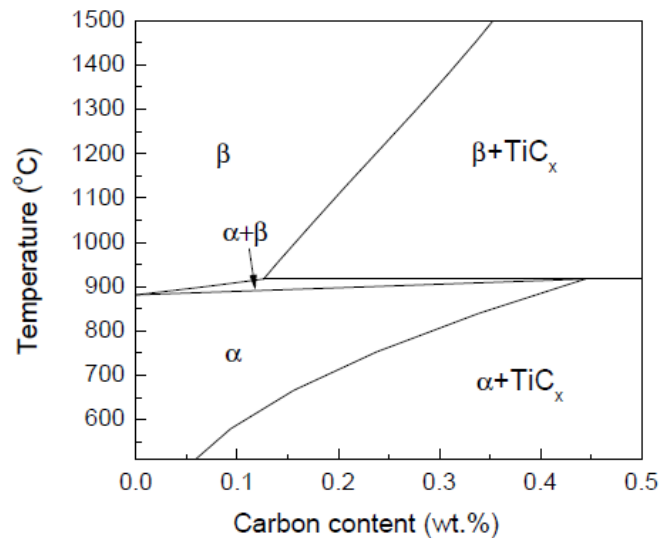


Fig. 6.3-3. Calculated binary phase diagram of Ti-C according to the thermodynamic data [186]

The solubility of carbon in α -Ti and β -Ti could be predicted with the CALPHAD (CALCulation of Phase Diagram) approach. The C-Ti system as shown in Fig. 6.3-3 was reported by Frisk [186]. Addition of Mn and Nb would effect some variations in the actual experimental phase diagram of the alloy, but we can find a general trend for the solubility of carbon in titanium.

Carbon in Ti-4Mn-14Nb and Ti-10Mn-14Nb alloy (Fig. 5.4-4) is around 2100 $\mu\text{g/g}$, this value is a bit higher than in other sintered Ti-Mn-Nb alloys (1500 $\mu\text{g/g}$). This may be caused in the debinding or sintering process. Oxygen and nitrogen contents do not differ very much from other Ti-Mn-Nb alloys. According to the C-Ti phase diagram, the solubility of carbon in the β phase decreases with falling temperature. From the microstructure of Ti-4Mn-14Nb and Ti-10Mn-14Nb alloys shown in Fig. 5.2-3 (a) and (b) it can be concluded that a large amount of Ti_2C precipitated from the β -Ti matrix during cooling. Ti_2C precipitates and interstitial elements can hinder the slip of dislocations during plastic deformation [187, 188]. This is the typical effect of solid solution hardening. Although this can increase the resistance of the alloy to deformation, the presence of a large number of Ti_2C precipitates causes the plasticity of the alloy to be lost. In addition, due to the brittleness of the Ti_2C phase [50], the carbide particles are split during the tensile deformation. It can be assumed that the presence of Ti_2C precipitates causes the elongation of the alloy to decrease, thus resulting in brittle fracture of Ti-4Mn-14Nb and Ti-10Mn-14Nb alloy.

6. Discussion

The $\alpha+\beta$ structure can dissolve more interstitial carbon (mainly in the α phase) than β single-phase, due to the higher carbon solubility of α phase. As Ti-4Mn-2Nb has a $\alpha+\beta$ structure, compared to the single β structure (Ti-4Mn-14Nb and Ti-10Mn-14Nb alloy), more carbon can be dissolved. Therefore, when the Ti-Mn-Nb alloys belong to $\alpha+\beta$ structure, the precipitation of a large amount of Ti_2C can be avoided and a better elongation (compared with β single-phase alloys) can be obtained.

6.3.3 TEM analysis

By TEM analysis of the deformed structure of the Ti-4Mn-2Nb alloy, it was found that there are dislocation lines (Fig. 5.5-3 yellow arrow) in the matrix. During the deformation process, the β phase, which has a b.c.c. structure, has 12 slip systems [18]. By external force, the slip systems are activated, dislocations are generated, and the dislocations move and cause deformation [184, 188]. However, when these dislocations encounter the Ti_2C phase, further movement is usually hindered due to the difference in the lattice. Ti_2C acts as a pinning point during the deformation process, causing the slip to not proceed smoothly, thereby increasing the strength of the alloy. However, if the dislocations accumulate at the Ti_2C phase boundary, the density of dislocation is increasing and energy for the formation of cracks is provided resulting in fracture. It also explains that the elongation decreases as the Ti_2C content increases.

6.4 Enhancement of mechanical properties with Y element addition

Considering its good tensile strength and elongation (shown in Fig. 5.4-5), Ti-4Mn-2Nb is the favorable alloy with suitable mechanical properties. The goal for mechanical properties in this study is to reach and exceed the requirement for Ti-6Al-4V (ASTM F2885 Grade 5 undensified) processed by MIM [99]. MIM Ti-4Mn-2Nb (UTS: 725 MPa, YS: 642 MPa and Elongation: 16%) is not good enough compared to MIM Ti-6Al-4V (UTS: 780MPa, YS: 680MPa, Elongation: 10%). The next step is to increase the UTS and YS, therefore, the rare earth element yttrium was used as an addition to the alloy for reinforcement.

As Fig. 6.4-1 shows, when the trace amount increases to 0.1% and 0.5 Y% (at.%), respectively, the mechanical properties of the alloy show significant differences. The column on the right in the figure represents the mechanical properties requirement of Ti-6Al-4V (ASTM F2885 Grade 5 undensified). When the Y content is 0.1%, tensile strength (UTS) of Ti-4Mn-2Nb-0.1Y alloy is increased from 725 MPa to 785 MPa (YS increased from 656MPa to 736MPa) while maintaining an elongation of 12.9%. This has already exceeded Ti-6Al-4V (the right column in Fig. 6.4-1). It is considered that the addition of yttrium resulting in a YS and UTS enhancement of Ti-4Mn-2Nb-0.1Y and Ti-4Mn-2Nb-0.5Y alloy.

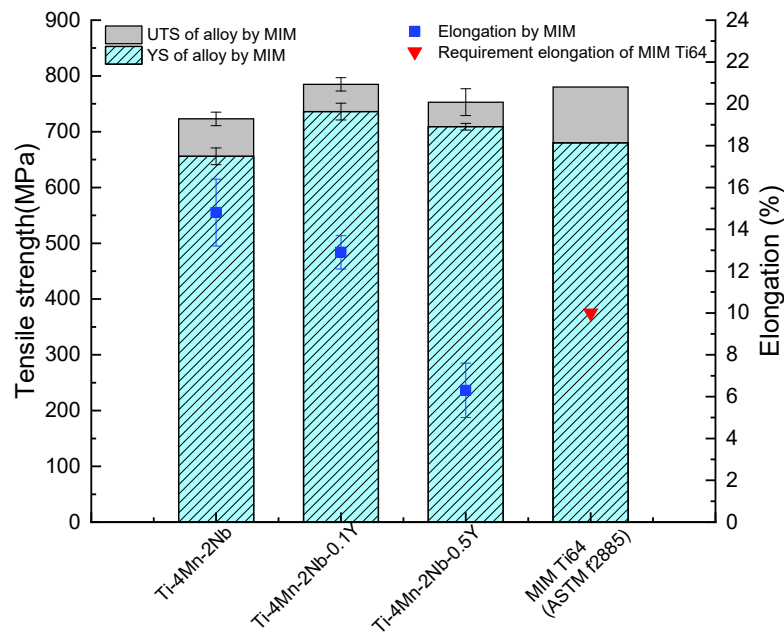


Fig. 6.4-1. Ultimate tensile strength (UTS), yield strength (YS) and elongation of Ti-4Mn-2Nb-xY ($x=0.1, 0.5$) fabricated by MIM and requirement of Ti-6Al-4V (ASTM F2885 Grade 5 undensified)

From Fig. 5.2-5 (section 5.2) and Fig. 5.3-3 (section 5.3), it can be concluded that by adding yttrium, Y_2O_3 particles are precipitated in the Ti-4Mn-2Nb alloys. The average grain size of Y_2O_3 is around 15 μm (Fig. 5.2-5). After deformation (for example, in tensile test), the Y_2O_3 particles can be observed on the fracture surface. After the tensile fracture, it is found that fine particles are present on the fracture surface (Fig. 6.4-2).

According to the EDS analysis, it can be concluded that the particles found in the dimple are Y_2O_3 . Below 900 °C, yttrium has almost no solubility in Ti [189], and it has a strong attraction with oxygen and can react with the interstitial element O in the Ti matrix, to form a rare earth oxide (Y_2O_3). This precipitation occurs through nucleation and growth processes, and fluctuations in solute concentration provide clusters of atoms in a small crystal lattice as a core of the precipitate [190].

6. Discussion

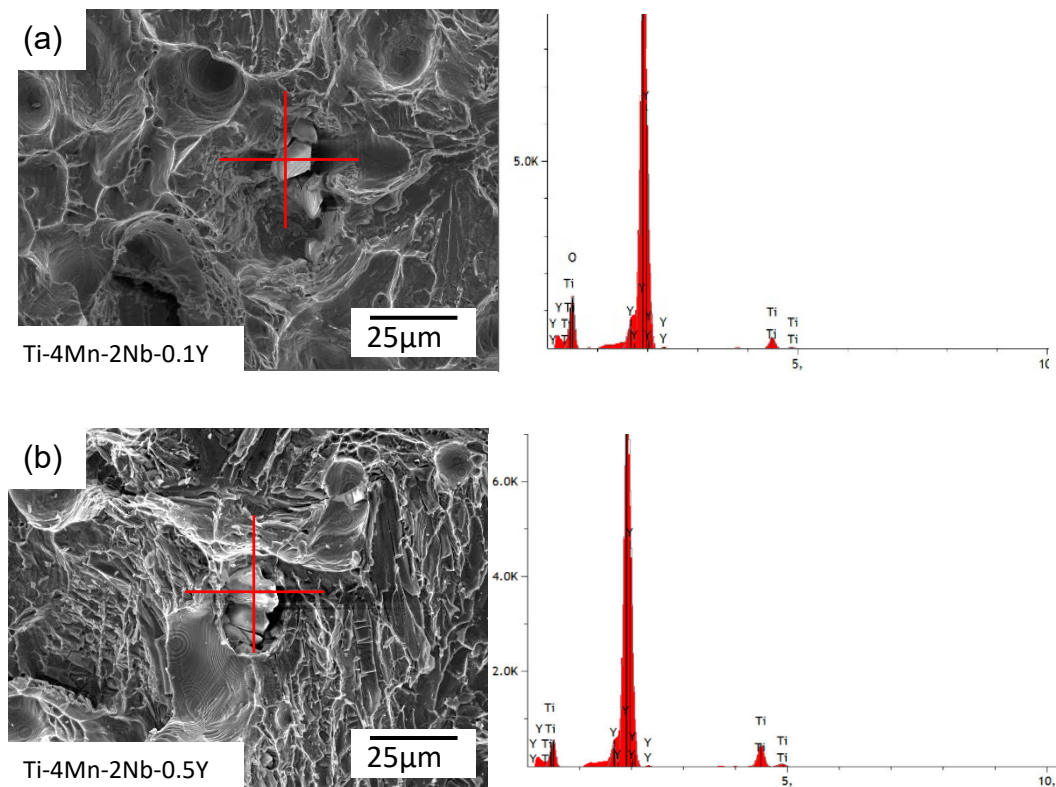


Fig. 6.4-2. EDS analysis of particles on the fracture surfaces of Ti-4Mn-2Nb-0.1Y and Ti-4Mn-2Nb-0.5Y

In-sintered Ti-Mn-Nb-xY ($x=0, 0.1, 0.5$), a grain size reduction with increasing Y content can be clearly found (Fig. 6.4-3). The reduced grain size can change the mechanical properties of the alloys. The theory of fine-grain strengthening has already been mentioned in section 6.3.1. After the addition of rare earth Y, the grain size of the alloy is reduced by approximately 43% (from 570 µm to 325 µm). By the Hall-Petch effect, the strength will increase with decreasing grain size.

Furthermore, from the energy point of view, during the sintering process, the lattice parameter of Y_2O_3 particles [191] is different from that of the Ti matrix (whether α -Ti or β -Ti) [192], so that the interface of the Y_2O_3 particles can act as nucleation site during the sintering. It can be considered that this mismatch can provide energy for nucleation growth or grain boundary formation. This leads to an increase in the number of grains and grain boundaries, which refine the grains.

However, the addition of Y not only affects the grain size but also small increases the interstitial element O in the entire alloys (revealed in Fig. 5.4-4). The increased oxygen content may result from oxidized Y powder. However, it is confirmed that slightly increasing the content of the interstitial element O can promote the strength of the titanium alloy [110, 193].

Another important indicator of the mechanical properties of MIM Ti-Mn-Nb alloys is density. When the density changes greatly, the strength of the alloys is affected by the presence or absence of pores (e.g. Ti-4Mn-2Nb-0.1Y and Ti-4Mn-2Nb-0.5Y in Fig.6.4-3). The density dropped from 97.5% (Ti-4Mn-2Nb) to around 95% (Ti-4Mn-2Nb-0.1Y and Ti-4Mn-2Nb-0.5Y). However, yield strength is still significantly improved. This is the result of the combined effect of precipitates, grain size, interstitials and porosity with the addition of the Y element.

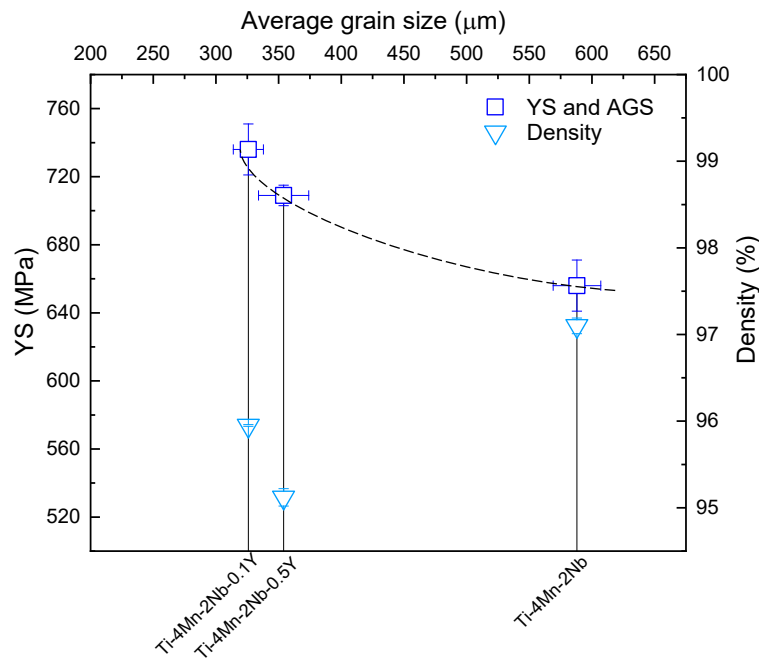


Fig. 6.4-3. Variation of yield strength (YS) versus average grain size (AGS) for Ti-Mn-Nb-xY (x=0, 0.1, 0.5) alloys and density of alloys.

When the content of the Y is 0.1%, as shown in Fig. 6.4-1, the UTS and elongation of the Ti-4Mn-2Nb-0.1Y alloy are already higher than Ti-10Mn-14Nb produced by arc-melting and are also exceeding the requirement of Ti-6Al-4V by ASTM F2885. The expectations for mechanical properties have been successfully completed in the study. Compared with Ti-10Mn-14Nb alloy produced by arc-melting, the content of Mn in Ti-4Mn-2Nb-0.1Y is decreased by 59.06%, and Nb content is reduced by 84.05%. This will greatly reduce the cost of alloy.

6.5 Biocompatibility of Ti-Mn-Nb alloy fabricated by MIM

As discussed, the Ti-4Mn-2Nb alloy fabricated by MIM provides sufficiently good mechanical properties and due to its reduced content of alloying elements (Mn and Nb) qualifies itself as a low-cost alloy. However, as a biomaterial, biological properties have to be investigated [194]. If in vitro

6. Discussion

experiments would show Ti-4Mn-2Nb to be highly toxic, so cells cannot grow on the alloy surface, the alloy is useless for medical purpose even if it possess good mechanical properties.

In biological experiments, we used pure titanium and glass plates as the main reference group. These two materials have been proven harmless to cells [32, 195, 196]. There are also Ti-2Nb (without Mn) and Ti-4Mn alloy (without Nb) as control groups to compare the effects of Mn and Nb on cell culture in titanium alloys. This can give us insight which elements may affect the cell culture experiments of Ti-Mn-Nb alloys. As revealed in section 5.7 (Fig. 5.7-1 and Fig. 5.7-2), Ti-Mn-Nb ternary alloys (including Ti-4Mn-2Nb-0.1Y and Ti-4Mn-2Nb-0.5Y) fabricated by MIM show very high activity results. When Mn is in the range of 3% to 6%, Nb is in the range of 1% to 4%, and Y is in the range of 0.1% to 0.5%, the MG63 cell culture experiment result shows no significant cell death. However, an unusual behavior was found in the control group. In Fig. 5.7-1 (c), after 5 days cultured, some dead cell were observed on the Ti-4Mn alloy. According to report, it was proved that the increase in Mn content will precipitate more Mn ions [44]. The remaining 3 control groups (Fig. 5.7-1 (a), (b) and (d)) behaved completely normal.

Also in the subsequent analysis of the culture supernatant (section 5.6.2) and the analysis of cells attached to the surface of the alloys (section 5.6.3), the same results were obtained, and the biological properties of the Ti-Mn-Nb ternary alloy performed well in the 5-day culture and no toxicity occurred. Only the binary Ti-4Mn alloy exhibited a different results than other alloys. Fig. 6.5-2 shows a summary of the cell activity assessment tests. Cells adhesion, spreading and migration are the first sequential reactions when coming into contact with a material surface, which is crucial for cells survival [197]. The bars (green as control groups and grey as experiment alloys) represent the ratio of red dead cells to green living cells (calculated by Image J software of Fig. 5.7-1 and Fig. 5.7-2). This ratio clearly shows that the mortality of the Ti-4Mn alloy is much higher than that of other alloys. In Ti-4Mn binary alloy, the effect of Mn on cell activity is greater than that of Ti. Although Mn is a necessary trace element in the human body, high valence Mn ions are also toxic to cells [198]. According to research reports, the increase of Mn content leads to an increase in Mn ion precipitation [44]. In the Ti-2Nb binary alloy, the biocompatibility of the alloy is the same as that of the Ti-4Mn-2Nb alloy and pure Ti control groups (Fig. 6.5-2). Regardless of the ratio, the amount of DNA, or LDH assay, is better than that of Ti-4Mn binary alloy. The cell activities of Pure Ti, Ti-4Mn-2Nb and Ti-2Nb alloys were consistent. Only Ti-4Mn alloy has low cell viability. According to research reports, in the Ti-Mn binary alloy, the increase of Mn content leads to an increase in Mn ion precipitation [44]. It can be considered that Mn ions are released into the liquid, which leads to a decrease in cell viability, and the addition of Nb can suppress this phenomenon. When 0.1% Y was added, the biocompatibility of the Ti-4Mn-2Nb-0.1Y alloy exhibits

about the same level as Ti-4Mn-2Nb. Both Ti-4Mn-2Nb and Ti-4Mn-2Nb-0.1Y are equivalent to pure titanium. This indicates that for MG63 alloy, cells can adhere well to the surface of the alloy and proliferate.

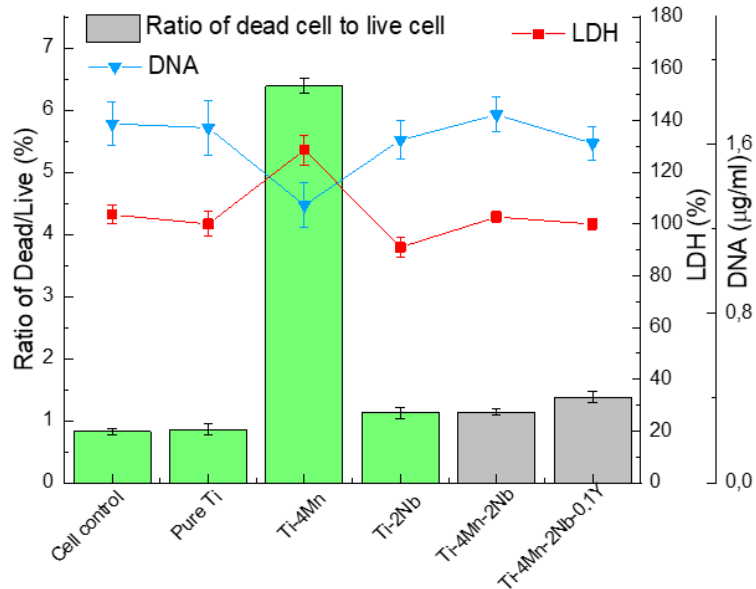


Fig. 6.5-2. Cell culture activity assessment (Green as control groups and grey as experiment alloys)

Fig. 6.5-3 is a comparison of the polarization curves of the Ti-4Mn alloy with pure titanium and the Ti-4Mn-2Nb alloy. It can be clearly seen from the figure that the self-corrosion current of the Ti-4Mn alloy is greater (121.6 nA/cm^2) than that of pure titanium (78.5 nA/cm^2) and Ti-4Mn-2Nb (9.9 nA/cm^2). This revealed that in HBSS, the Ti-4Mn alloy is more susceptible to corrosion. It can be assumed that ions or corrosion products are formed during the 5 days of cell culture, which adversely affect the cells attached on the surface of the Ti-4Mn binary alloy and even cause cell death. However, the self-corrosion current of Ti-4Mn-2Nb alloy is very low, which is effected by only 2% (at.%) Nb addition to Ti-4Mn. The experimental results (Fig. 6.5-3) prove that after the addition of Nb, the corrosion resistance of the alloy is improved significantly. Thereby, the biocompatibility of the Ti-4Mn-2Nb alloy is improved.

6. Discussion

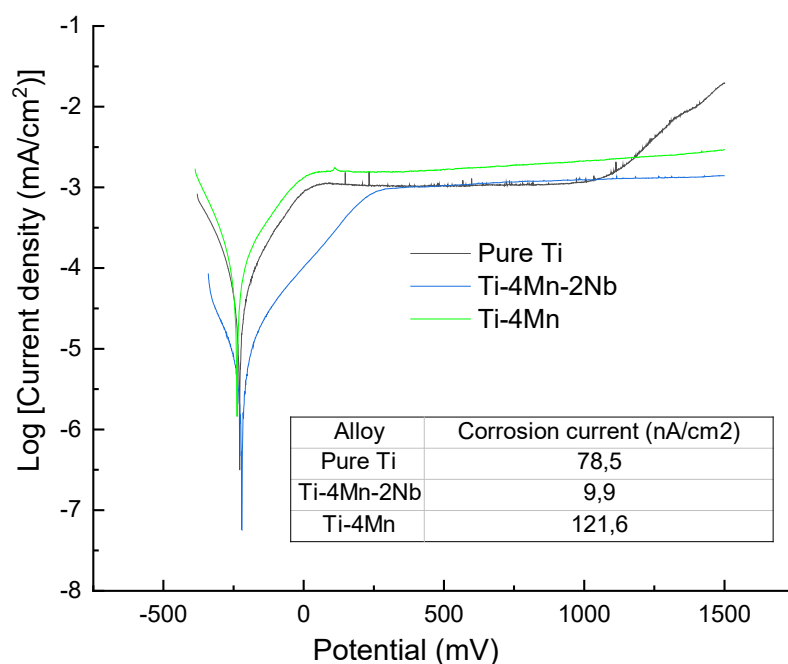


Fig. 6.5-3. Potential–current plots for Ti-4Mn, Ti-4Mn-2Nb and Pure Ti recorded by potentiodynamic polarization in HBSS at 37.0°C

6.6 Corrosion behavior of samples fabricated by MIM

When applied to bone as an implant material, it is also important to study the corrosion behavior of Ti alloys in the human body environment. From the above research results, it is found that the Ti-4Mn-2Nb alloy and the Ti-4Mn-2Nb-0.1Y alloy not only have good mechanical properties but also good biocompatibility in biological performance evaluation.

In the subsequent corrosion behavior test, the corrosion current results are shown in Table 6.6-1. Here we can see that when Mn is between 4% and 6% and Nb between 2% and 4%, the corrosion current of the alloys does not change much (8.3 nA/cm² - 10.3 nA/cm²). It is noteworthy that the corrosion current is already in the order of nA/cm², which is much smaller than the mA/cm² of normal metals (e.g. Al, Mg and iron). Only when the Mn content is increased to 10% or the Nb content is increased to 14%, the self-corrosion current of the alloy is increased to 19 nA/cm² and 29 nA/cm². In the Table 5.8-3 (section 5.8.2), it is also shown that with addition of 0.1% and 0.5% Y, the corrosion current (7.3 nA/cm² and 8.9 nA/cm²) does not change much (compared with Ti-6Al-4V 90 nA/cm²). It is not only an order of magnitude lower than for pure Ti (78 nA/cm²) but also for Ti-6Al-4V (90.3 nA/cm²). Ti-6Al-4V

and pure Ti have been reported to have good corrosion properties [199, 200], especially as implant materials.

Table 6.6-1. Corrosion current of different Mn and Nb content in Ti-Mn-Nb alloys

Mn (at.%) \ Nb (at.%)	4	6	10
2	9.9 nA/cm ²	9.8 nA/cm ²	
4	8.3 nA/cm ²	10.3 nA/cm ²	
14	19.0 nA/cm ²		29.8 nA/cm ²

Figure 6.6-1 shows the fits to the Bode plot and the phase angles of the titanium alloys fabricated by MIM immersed in HBSS for 24 h at 37 °C. The phase angles approach -90° at around 100 Hz, and only one time-constant was found. It is considered that a highly stable film formed on the titanium surface during immersion [201]. This is consistent with the Bode curve. Based on the EIS features, the simple equivalent circuit shown on the right side can be used to simulate the passivation process. The model assumes that one layer of passive film formed on titanium alloys and this film is a compact film[200]. In the equivalent electrical circuit, R_s corresponds to the resistance of the solution, R_p to the resistance of compact passive film and the constant phase element (CPE) was used as capacitance in simulating the process in order to simplify fitting.

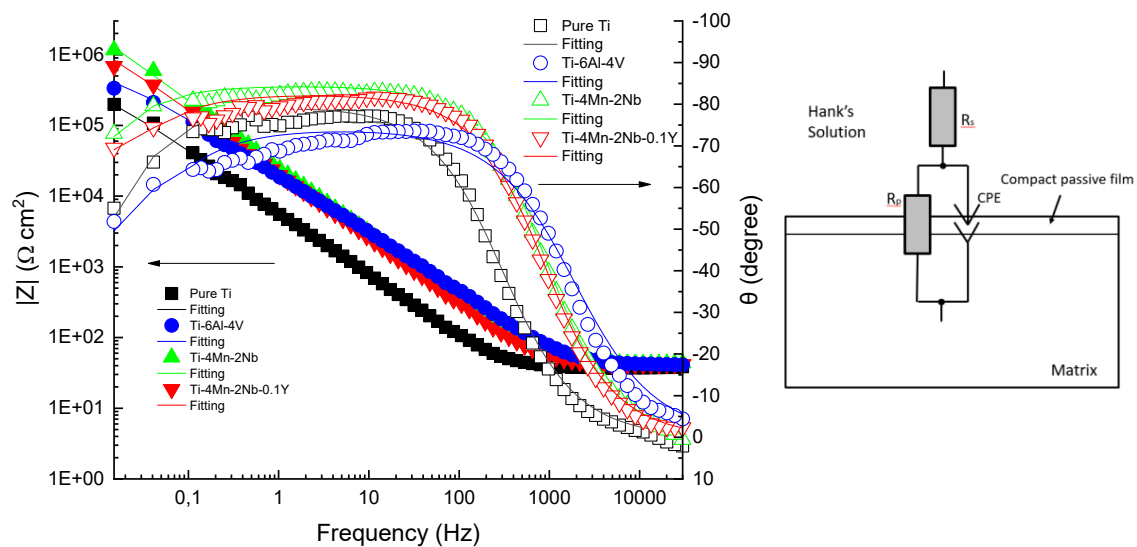


Fig. 6.6-1. Fitted Bode impedance spectra of Ti-4Mn-2Nb alloy and Ti-4Mn-2Nb-0.1Y alloy with pure Ti and Ti-6Al-4V control groups (MIM) measured in HBSS at 37°C after 24 hours. The solid lines represent the fitting results. Equivalent electrical circuit (for compact passive film) used to Bode plots as shown on the right side

6. Discussion

The value of the R_p reflects the corrosion resistance of the alloy in HBSS [202]. The R_p values of Ti-Mn-Nb alloys are higher than pure titanium and Ti-6Al-4V. A higher R_p represents a higher resistance value of the passive film. Therefore, in the analog circuit (Fig. 6.6-1), the film attached to the surface of the alloy will give the substrate a good protection against dissolution and further corrosion of the substrate. This is consistent with the self-corrosion current measurement in the polarization experiments (in section 5.8.1), which further demonstrates that the Ti-4Mn-2Nb and Ti-4Mn-2Nb-0.1Y alloy designed in this work have better corrosion performance than the conventional Ti-6Al-4V and pure titanium in HBSS at 37° C.

Moreover, due to the appearance of a compact passive film, in the biological evaluation of the alloy, the cells have very good adaptability to the film, which is beneficial to cell adhesion and proliferation.

7. Summary and conclusions

In this study, a novel type of ternary Ti-Mn-Nb alloys is prepared. The alloys are fabricated by arc-melting and metal injection moulding. By analyzing the tensile properties of the alloys, the mechanical properties of Ti-Mn-Nb alloys prepared by these two different methods are investigated and compared. Since the Ti-Mn-Nb alloys were newly developed, and there is no standard for Ti-Mn-Nb alloy, the analysis relies mainly on cross-comparison within the group of investigated alloys. In addition, pure titanium and the alloy Ti-6Al-4V are used as control groups. Ti-Mn-Nb alloys are tested in vitro biocompatibility. Cell culture experiments are carried out on the surface of Ti-Mn-Nb alloys by using osteoblast MG63, and the biocompatibility is evaluated by cell activity. Meanwhile, the corrosion performances of the alloys are determined in a simulated human body fluid environment.

The ultimate objective of this study is to obtain a low-cost titanium alloy with good mechanical properties and biocompatibility for human implant materials. The results and analysis obtained from those investigations lead to the following conclusions:

1. By arc-melting, Ti-xMn-yNb (x=4, 10; y=2, 8, 14) alloys are fabricated. After heat treatment at 900 °C for 1 hour and subsequent water quench to room temperature, the single β phase structure of Ti-xMn-yNb (x=4, 10; y=2, 8, 14) alloys are obtained. These alloys have good mechanical properties: UTS is 700 MPa to 760 MPa; YS is 601MPa to 692MPa; elongation is 6% to 10.5%. When the Mn content reaches 16%, the Ti-16Mn-yNb (y=2, 8, 14) alloys exhibit brittle fracture.
2. For Ti-xMn-yNb (x=4, 10; y=2, 8, 14) fabricated by arc-melting, results indicate that the contribution of Mn to improve tensile strength is significant. Meanwhile, niobium contributes to the increase in elongation of Ti-Mn-Nb alloys. Thus, Ti-10Mn-14Nb (at.%) (Ti-10Mn-23.7Nb (wt.)) is the optimal alloy considering tensile strength (760MPa) and elongation (10.5%).
3. By metal injection moulding, a density between 96% and 97% could be achieved for sintered Ti-xMn-yNb (x=3, 4, 6; y=1, 2, 4) alloys. Moreover, young's modulus of MIM Ti-Mn-Nb alloys is in the range of 80 GPa to 100 GPa which is also lower than that of the traditional biomaterial Ti-6Al-4V (110 GPa).
4. The MIM method inevitably introduces interstitial elements. Interstitial element C is α stabilizer. The sintered Ti-4Mn-14Nb and Ti-10Mn-14Nb (both β single-phase structure) specimens exhibit the lowest mechanical properties (compared with the other sintered alloys) due to the high amounts of Ti_2C precipitates.

7. Summary and conclusions

5. Sintered Ti-xMn-yNb (x=3, 4, 6; y=1, 2, 4) alloys have the $\alpha+\beta$ phase structure and exhibit good mechanical properties with UTS of around 700 MPa to 800 MPa, and also 6% to 16% elongation. Among them, a very good combination of mechanical properties is achieved for MIM processed Ti-4Mn-2Nb (at.%) (Ti-4.5Mn-3.8Nb (wt.%)), namely a YS of 642 MPa, UTS of 725 MPa and a high ductility of 16% elongation to fracture.

6. By metal injection moulding, when the yttrium content is 0.1% (at.%), the tensile strength of Ti-4Mn-2Nb-0.1Y (at.%) (Ti-4.5Mn-3.8Nb-0.18Y (wt.%)) is increased from 725 MPa (MIM Ti-4Mn-2Nb) to 785 MPa while maintaining an elongation of 12.9%. These mechanical properties already exceed Ti-6Al-4V (ASTM F2885 Grade 5 undensified).

7. Compared with the Ti-10Mn-14Nb alloy produced by arc melting, the content in weight of Mn in MIM Ti-4Mn-2Nb-0.1Y is decreased by 59.06%, and of Nb by 84.05%. The UTS and elongation not only exceeded the ones of Ti-10Mn-14Nb (arc melting), but also the cost of the alloy is greatly reduced.

8. In the in vitro evaluation, in comparison with pure titanium, human osteoblasts MG63 adhered as well and proliferated on the surface of MIM Ti-Mn-Nb specimens. In the supernatant after cell culture, the Ti-Mn-Nb alloy shows similar osmolality and pH value results as pure titanium. The Ti-Mn-Nb alloys are not found to be toxic to MG63 cells.

9. In the study of corrosion behavior in Hanks' balanced salt solution (HBSS) at 37 °C, the self-corrosion current density as well as the impedance of MIM Ti-Mn-Nb alloys are all better than those of pure titanium and even better than those of MIM Ti-6Al-4V alloy.

In summary, compared to arc melting, Ti-4Mn-2Nb and Ti-4Mn-2Nb-0.1Y fabricated by MIM exhibit very good mechanical properties. As a bio-implanted alloy, its performance is similar to pure titanium in cell biological tests. Meanwhile, it performs excellent in corrosion behavior. The results presented in this study demonstrate the feasibility of low-cost MIM Ti-Mn-Nb alloys as biomedical material.

References:

1. Cotton, F.A., et al., *Advanced inorganic chemistry*. Vol. 6. 1988: Wiley New York.
2. Weeks, M.E., *The discovery of the elements. XI. some elements isolated with the aid of potassium and sodium: zirconium, titanium, cerium, and thorium*. Journal of Chemical Education, 1932. **9**(7): p. 1231.
3. Cao, W. and L.L. Hench, *Bioactive materials*. Ceramics international, 1996. **22**(6): p. 493-507.
4. Geetha, M., et al., *Ti based biomaterials, the ultimate choice for orthopaedic implants—a review*. Progress in materials science, 2009. **54**(3): p. 397-425.
5. Niinomi, M., et al., *Development of low rigidity β -type titanium alloy for biomedical applications*. Materials Transactions, 2002. **43**(12): p. 2970-2977.
6. Perl, D.P., *Relationship of aluminum to Alzheimer's disease*. Environmental health perspectives, 1985. **63**: p. 149-153.
7. Atsdr, U., *Agency for toxic substances and disease registry*. Case Studies in environmental medicine. 1997.
8. Domingo, J.L., *Vanadium and tungsten derivatives as antidiabetic agents*. Biological Trace Element Research, 2002. **88**(2): p. 97-112.
9. Kim, J.-W., et al., *Effect of manganese on the microstructure, mechanical properties and corrosion behavior of titanium alloys*. Materials Chemistry and Physics, 2016. **180**: p. 341-348.
10. Niinomi, M., M. Nakai, and J. Hieda, *Development of new metallic alloys for biomedical applications*. Acta biomaterialia, 2012. **8**(11): p. 3888-3903.
11. Erdmann, L. and T.E. Graedel, *Criticality of non-fuel minerals: a review of major approaches and analyses*. Environmental science & technology, 2011. **45**(18): p. 7620-7630.
12. Chu, S., *Critical materials strategy*. 2011: DIANE Publishing.
13. Van Noort, R., *Titanium: the implant material of today*. Journal of Materials Science, 1987. **22**(11): p. 3801-3811.
14. Zhang, H., et al., *The clarification of α " phase precipitate from β phase in Ti-15Mn alloy by mismatch theory*. Materials Letters, 2017. **202**: p. 138-141.
15. Hashmi, S., *Comprehensive materials finishing*. 2016: Elsevier.
16. Sigel, H., *Metal ions in biological systems: volume 37: manganese and its role in biological processes*. 2000: CRC press.
17. Zagrebelnyy, D.V., *Modeling macrosegregation during the Vacuum Arc Remelting of Ti-10v-2Fe-3Al alloy*. 2007.

References

18. Leyens, C. and M. Peters, *Titanium and titanium alloys: fundamentals and applications*. 2003: John Wiley & Sons.
19. Ferri, O., T. Ebel, and R. Bormann, *High cycle fatigue behaviour of Ti-6Al-4V fabricated by metal injection moulding technology*. *Materials Science and Engineering: A*, 2009. **504**(1-2): p. 107-113.
20. Ebel, T., et al., *Ti-6Al-4V-0.5 B—A modified alloy for implants produced by metal injection molding*. *Advanced Engineering Materials*, 2011. **13**(12): p. B440-B453.
21. Malinauskas, M., et al., *3D microporous scaffolds manufactured via combination of fused filament fabrication and direct laser writing ablation*. *Micromachines*, 2014. **5**(4): p. 839-858.
22. McIlroy, C. and P. Olmsted, *Disentanglement effects on welding behaviour of polymer melts during the fused-filament-fabrication method for additive manufacturing*. *Polymer*, 2017. **123**: p. 376-391.
23. Niinomi, M., *Metals for biomedical devices*. 2019: Woodhead publishing.
24. Lütjering, G. and J. Williams, *Titanium Springer-Verlag Berlin Heidelberg*. New York, 2003. **48**.
25. Oosthuizen, S., *Titanium: the innovators' metal-Historical case studies tracing titanium process and product innovation*. *Journal of the Southern African Institute of Mining and Metallurgy*, 2011. **111**(11): p. 781-786.
26. Adell, R., et al., *A long-term follow-up study of osseointegrated implants in the treatment of totally edentulous jaws*. *International Journal of Oral & Maxillofacial Implants*, 1990. **5**(4).
27. Haag, P. and K. Nilner, *Bonding between titanium and dental porcelain: A systematic review*. *Acta Odontologica Scandinavica*, 2010. **68**(3): p. 154-164.
28. Kim, D.-H., et al., *Characterization of diamond-like carbon films deposited on commercially pure Ti and Ti-6Al-4V*. *Materials Science and Engineering: C*, 2002. **22**(1): p. 9-14.
29. Osathanon, T., et al., *Ti-6Al-7Nb promotes cell spreading and fibronectin and osteopontin synthesis in osteoblast-like cells*. *Journal of Materials Science: Materials in Medicine*, 2006. **17**(7): p. 619-625.
30. Miura-Fujiwara, E., T. Okumura, and T. Yamasaki, *Frictional and wear behavior of commercially pure ti, ti-6al-7nb, and sus316l stainless steel in artificial saliva at 310 k*. *Materials transactions*, 2015. **56**(10): p. 1648-1657.
31. Elias, L., et al., *Microstructural and mechanical characterization of biomedical Ti-Nb-Zr (-Ta) alloys*. *Materials Science and Engineering: A*, 2006. **432**(1-2): p. 108-112.
32. Gepreel, M.A.-H. and M. Niinomi, *Biocompatibility of Ti-alloys for long-term implantation*. *Journal of the mechanical behavior of biomedical materials*, 2013. **20**: p. 407-415.

33. Niinomi, M., *Biologically and mechanically biocompatible titanium alloys*. Materials transactions, 2008. **49**(10): p. 2170-2178.
34. Santos, P.F., et al., *Fabrication of low-cost beta-type Ti–Mn alloys for biomedical applications by metal injection molding process and their mechanical properties*. Journal of the mechanical behavior of biomedical materials, 2016. **59**: p. 497-507.
35. Nag, S., et al., *Comparison of microstructural evolution in Ti–Mo–Zr–Fe and Ti–15Mo biocompatible alloys*. Journal of Materials Science: Materials in Medicine, 2005. **16**(7): p. 679-685.
36. Nitta, K., *Ni-free Ti–Nb–Sn shape memory alloys*. Structural Biomaterials for 21st Century, 2001: p. 25-34.
37. Daimatsu, Y., et al., *Shape memory characteristics of Ti–Mo–Ga for biomedical applications*. Proc. Fall Meet. Jpn Inst. Met, 2001. **401**.
38. Hosoda, H., A. Yamamoto, and S. Miyazaki, *Mechanical properties of Ti–Mo–Ge shape memory alloy for biomedical applications*. Proc. Fall Meet. Jpn Inst. Met, 2001. **401**.
39. Hiromoto, H., et al., *Polarization behavior of Ti–Mo–Al shape memory alloy in simulated body liquid*. Proc. Annu. Meet. Jpn Inst. Met, 2002. **443**.
40. Ikeda, M., Y. Nakamura, and N. Takahama, *Effect of Zr contents on heat treatment behaviors and phase constitution of Ti–50 mass% Ta–Zr alloy*. Proc. Annu. Meet. JIM, 2003. **130**.
41. Maeshima, T., et al., *Development of Ti–Sc–Mo shape memory alloy*. Annu. Meet. JIM, 2003: p. 134.
42. Niinomi, M., *Recent titanium R&D for biomedical applications in Japan*. Jom, 1999. **51**(6): p. 32-34.
43. Cho, K., et al., *Improvement in mechanical strength of low-cost β -type Ti–Mn alloys fabricated by metal injection molding through cold rolling*. Journal of Alloys and Compounds, 2016. **664**: p. 272-283.
44. Santos, P.F., et al., *Microstructures, mechanical properties and cytotoxicity of low cost beta Ti–Mn alloys for biomedical applications*. Acta biomaterialia, 2015. **26**: p. 366-376.
45. Ikeda, M., et al., *Isothermal aging behavior of beta titanium–manganese alloys*. Materials transactions, 2009. **50**(12): p. 2737-2743.
46. Samsonov, G., *Mechanical properties of the elements, in Handbook of the Physicochemical Properties of the Elements*. 1968, Springer. p. 387-446.
47. Matsuno, H., et al., *Biocompatibility and osteogenesis of refractory metal implants, titanium, hafnium, niobium, tantalum and rhenium*. Biomaterials, 2001. **22**(11): p. 1253-1262.
48. Donato, T.A., et al., *Cytotoxicity study of some Ti alloys used as biomaterial*. Materials Science and Engineering: C, 2009. **29**(4): p. 1365-1369.

References

49. Miura, K., et al., *The bone tissue compatibility of a new Ti–Nb–Sn alloy with a low Young's modulus*. Acta biomaterialia, 2011. **7**(5): p. 2320-2326.
50. Zhao, D., et al., *Microstructure and mechanical behavior of metal injection molded Ti–Nb binary alloys as biomedical material*. Journal of the mechanical behavior of biomedical materials, 2013. **28**: p. 171-182.
51. Murray, J.L., *The Nb–Ti (Niobium-Titanium) system*. Bulletin of Alloy Phase Diagrams, 1981. **2**(1): p. 55-61.
52. Tane, M., et al., *Low Young's modulus in Ti–Nb–Ta–Zr–O alloys: Cold working and oxygen effects*. Acta Materialia, 2011. **59**(18): p. 6975-6988.
53. Martins, D.Q., et al., *Effects of Zr content on microstructure and corrosion resistance of Ti–30Nb–Zr casting alloys for biomedical applications*. Electrochimica Acta, 2008. **53**(6): p. 2809-2817.
54. Brailovski, V., et al., *Bulk and porous metastable beta Ti–Nb–Zr (Ta) alloys for biomedical applications*. Materials Science and Engineering: C, 2011. **31**(3): p. 643-657.
55. Sakaguchi, N., et al., *Relationships between tensile deformation behavior and microstructure in Ti–Nb–Ta–Zr system alloys*. Materials Science and Engineering: C, 2005. **25**(3): p. 363-369.
56. Ito, A., et al., *In vitro biocompatibility, mechanical properties, and corrosion resistance of Ti/Zr/Nb/Ta/Pd and Ti/Sn/Nb/Ta/Pd alloys*. Journal of biomedical materials research, 1995. **29**(7): p. 893-899.
57. Narayan, R., *Fundamentals of medical implant materials*. ASM handbook, 2012.
58. Hollemann-Wiberg, L.d.A.C., *Chemie 91-100. Auflage*. 1985, Walter de Gruyter, Berlin.
59. Lide, D.R., *CRC handbook of chemistry and physics: a ready-reference book of chemical and physical data*. 1995: CRC press.
60. Ebel, T., et al. *Metal injection moulding of titanium and titanium-aluminides*. in *Key Engineering Materials*. 2012. Trans Tech Publ.
61. Aschner, M., et al., *Manganese: recent advances in understanding its transport and neurotoxicity*. Toxicology and applied pharmacology, 2007. **221**(2): p. 131-147.
62. Gilca, M., et al., *The oxidative hypothesis of senescence*. Journal of postgraduate medicine, 2007. **53**(3): p. 207.
63. Baruthio, F., et al., *Determination of manganese in biological materials by electrothermal atomic absorption spectrometry: a review*. Clinical chemistry, 1988. **34**(2): p. 227-234.
64. Bock, N.A., et al., *Cerebrospinal fluid to brain transport of manganese in a non-human primate revealed by MRI*. Brain research, 2008. **1198**: p. 160-170.
65. Murray, J.L., *The Mn–Ti (Manganese-Titanium) system*. Bulletin of Alloy Phase Diagrams, 1981. **2**(3): p. 334-343.

66. Zhu, K., et al., *The Development of the low-cost titanium alloy containing Cr and Mn alloying elements*. Metallurgical and Materials Transactions A, 2014. **45**(4): p. 1761-1766.
67. He, G. and M. Hagiwara, *Ti alloy design strategy for biomedical applications*. Materials Science and Engineering: C, 2006. **26**(1): p. 14-19.
68. Schmid, H. and W. Mader, *Oxidation states of Mn and Fe in various compound oxide systems*. Micron, 2006. **37**(5): p. 426-432.
69. Metalary.com. Available from: <https://www.metalary.com>.
70. German, R.M., *STATUS OF METAL POWDER INJECTION MOLDING OF TITANIUM*. International Journal of Powder Metallurgy, 2010. **46**(5).
71. German, R.M., *Powder injection molding*. 1990.
72. Eisen, W., et al., *Powder metal technologies and applications*. 1998.
73. Thian, E., et al., *Effects of debinding parameters on powder injection molded Ti-6Al-4V/HA composite parts*. Advanced Powder Technology, 2001. **12**(3): p. 361-370.
74. Loh, N., S. Tor, and K. Khor, *Production of metal matrix composite part by powder injection molding*. Journal of Materials Processing Technology, 2001. **108**(3): p. 398-407.
75. Liu, Z., et al., *Binder system for micropowder injection molding*. Materials Letters, 2001. **48**(1): p. 31-38.
76. Liu, Z., et al., *Characterization of powder injection molding feedstock*. Materials characterization, 2002. **49**(4): p. 313-320.
77. Heaney, D., *Designing for metal injection molding (MIM)*, in *Handbook of Metal Injection Molding*. 2012, Elsevier. p. 29-49.
78. Goodship, V., *Troubleshooting injection moulding*. Vol. 15. 2004: iSmithers Rapra Publishing.
79. Zhang, J.-G., M.J. Edirisinghe, and J.R. Evans, *A catalogue of ceramic injection moulding defects and their causes*. Industrial Ceramics, 1989. **9**: p. 72-82.
80. Pan, J., et al., *A model for the sintering of spherical particles of different sizes by solid state diffusion*. Acta materialia, 1998. **46**(13): p. 4671-4690.
81. WALKER, R.F., *Mechanism of material transport during sintering*. Journal of the American Ceramic Society, 1955. **38**(6): p. 187-197.
82. Herring, C., *Diffusional viscosity of a polycrystalline solid*. Journal of applied physics, 1950. **21**(5): p. 437-445.
83. Herring, C., *Effect of change of scale on sintering phenomena*. Journal of Applied Physics, 1950. **21**(4): p. 301-303.
84. Fang, Z.Z., *Sintering of advanced materials*. 2010: Elsevier.

References

85. Ebel, T., et al., *Metal injection molding of titanium*, in *Titanium powder metallurgy*. 2015, Elsevier. p. 337-360.
86. You, S.H., J.H. Lee, and S.H. Oh, *A Study on Cutting Characteristics in Turning Operations of Titanium Alloy used in Automobile*. *International Journal of Precision Engineering and Manufacturing*, 2019. **20**(2): p. 209-216.
87. Zhao, D., et al., *Sintering behavior and mechanical properties of a metal injection molded Ti-Nb binary alloy as biomaterial*. *Journal of Alloys and Compounds*, 2015. **640**: p. 393-400.
88. Hon, Y.-H., J.-Y. Wang, and Y.-N. Pan, *Composition/phase structure and properties of titanium-niobium alloys*. *Materials Transactions*, 2003. **44**(11): p. 2384-2390.
89. Kafkas, F. and T. Ebel, *Metallurgical and mechanical properties of Ti-24Nb-4Zr-8Sn alloy fabricated by metal injection molding*. *Journal of Alloys and Compounds*, 2014. **617**: p. 359-366.
90. Endo, E., H. Nakayama, and H. Kyogoku. *Effect of Sintering Conditions on Microstructures and Mechanical Properties of Ti-29Nb-13Ta-4.6 Zr Alloy Fabricated by MIM Process*. in *European Congress and Exhibition on Powder Metallurgy. European PM Conference Proceedings*. 2016. The European Powder Metallurgy Association.
91. Santos, P.F., et al., *Improvement of microstructure, mechanical and corrosion properties of biomedical Ti-Mn alloys by Mo addition*. *Materials & Design*, 2016. **110**: p. 414-424.
92. Bania, P., *Beta titanium alloys in the 1990's*, ed. by D. Elylon, RR Boyer and DA Koss,(TMS, Warrendale, PA, 1993) pp, 1993: p. 3-14.
93. Birol, Y., *Production of Al-Ti-B master alloys from Ti sponge and KBF₄*. *Journal of alloys and compounds*, 2007. **440**(1-2): p. 108-112.
94. Sato, H., et al., *Mechanical properties of cast Ti-Hf alloys*. *Journal of Biomedical Materials Research Part B: Applied Biomaterials: An Official Journal of The Society for Biomaterials, The Japanese Society for Biomaterials, and The Australian Society for Biomaterials and the Korean Society for Biomaterials*, 2005. **72**(2): p. 362-367.
95. Liu, X., et al., *Thermodynamic assessment of the aluminum-manganese (Al-Mn) binary phase diagram*. *Journal of phase equilibria*, 1999. **20**(1): p. 45.
96. Qi, H., M. Azer, and A. Ritter, *Studies of standard heat treatment effects on microstructure and mechanical properties of laser net shape manufactured Inconel 718*. *Metallurgical and Materials Transactions A*, 2009. **40**(10): p. 2410-2422.
97. Nastac, L., et al., *Advances in investment casting of Ti-6Al-4V alloy: a review*. *International Journal of Cast Metals Research*, 2006. **19**(2): p. 73-93.
98. Migliori, A., et al., *Resonant ultrasound spectroscopic techniques for measurement of the elastic moduli of solids*. *Physica B: Condensed Matter*, 1993. **183**(1-2): p. 1-24.

99. G.T., *China metal material room temperature tensile test method [S]*. 2002.
100. Bagchi, D., et al., *In vitro and in vivo generation of reactive oxygen species, DNA damage and lactate dehydrogenase leakage by selected pesticides*. *Toxicology*, 1995. **104**(1-3): p. 129-140.
101. Legrand, C., et al., *Lactate dehydrogenase (LDH) activity of the number of dead cells in the medium of cultured eukaryotic cells as marker*. *Journal of biotechnology*, 1992. **25**(3): p. 231-243.
102. Waterstrat, R., B. Das, and P.A. Beck, *Phase Relationships in Titanium-Manganese System*. *Transactions of the Metallurgical Society of AIME*, 1962. **224**(3): p. 512-&.
103. Villars, P. and L. Calvert, *Pearson's Handbook*. 1997.
104. Zhao, D., et al., *Titanium carbide precipitation in Ti–22Nb alloy fabricated by metal injection moulding*. 2014, Taylor & Francis.
105. Ahmed, T. and H. Rack, *Phase transformations during cooling in α + β titanium alloys*. *Materials Science and Engineering: A*, 1998. **243**(1-2): p. 206-211.
106. Ferri, O., T. Ebel, and R. Bormann, *Influence of surface quality and porosity on fatigue behaviour of Ti–6Al–4V components processed by MIM*. *Materials Science and Engineering: A*, 2010. **527**(7-8): p. 1800-1805.
107. Zhao, D.-p., et al., *Trace carbon in biomedical beta-titanium alloys: recent progress*. *JOM*, 2015. **67**(10): p. 2236-2243.
108. Ebel, T., et al., *Reduction of the embrittlement effect of binder contamination in MIM processing of Ti alloys*. *Powder Metallurgy*, 2017. **60**(3): p. 157-166.
109. Ebel, T. and O.M. Ferri. *Pm lightweight materials: processing of Ti-15V-3Al-3Sn-3Cr by metal injection moulding*. in *European Congress and Exhibition on Powder Metallurgy. European PM Conference Proceedings*. 2011. The European Powder Metallurgy Association.
110. Limberg, W., et al., *Influence of the sintering atmosphere on the tensile properties of MIM-processed Ti 45Al 5Nb 0.2 B 0.2 C*. *Materials Science and Engineering: A*, 2012. **552**: p. 323-329.
111. Hidalgo, A.A., et al. *Fundamental Understanding of the Influence of Oxygen on the Fatigue behaviour of Ti-6Al-7Nb Alloys*. in *European Congress and Exhibition on Powder Metallurgy. European PM Conference Proceedings*. 2016. The European Powder Metallurgy Association.
112. Liu, Y., et al., *Microstructures evolution and mechanical properties of a powder metallurgical titanium alloy with yttrium addition*. *Materials and Manufacturing Processes*, 2010. **25**(8): p. 735-739.
113. Niu, H., et al., *High temperature deformation behaviors of Ti-45Al-2Nb-1.5 V-1Mo-Y alloy*. *Intermetallics*, 2011. **19**(12): p. 1767-1774.
114. Sidambe, A., *Biocompatibility of advanced manufactured titanium implants—A review*. *Materials*, 2014. **7**(12): p. 8168-8188.

References

115. Evans, A., *The strength of brittle materials containing second phase dispersions*. Philosophical Magazine, 1972. **26**(6): p. 1327-1344.
116. Zhang, J. and A. Alpas, *Delamination wear in ductile materials containing second phase particles*. Materials Science and Engineering: A, 1993. **160**(1): p. 25-35.
117. Ohmori, Y., et al., *Effects of ω -phase precipitation on $\beta \rightarrow \alpha$, α'' transformations in a metastable β titanium alloy*. Materials Science and Engineering: A, 2001. **312**(1-2): p. 182-188.
118. Goretzki, H., *Neutron diffraction studies on titanium - carbon and zirconium - carbon alloys*. physica status solidi (b), 1967. **20**(2): p. K141-K143.
119. Bhatia, S.K. and A.B. Yetter, *Correlation of visual in vitro cytotoxicity ratings of biomaterials with quantitative in vitro cell viability measurements*. Cell biology and toxicology, 2008. **24**(4): p. 315-319.
120. Saldaña, L., et al., *In search of representative models of human bone-forming cells for cytocompatibility studies*. Acta Biomaterialia, 2011. **7**(12): p. 4210-4221.
121. Clover, J. and M. Gowen, *Are MG-63 and HOS TE85 human osteosarcoma cell lines representative models of the osteoblastic phenotype?* Bone, 1994. **15**(6): p. 585-591.
122. Niinomi, M., *Recent metallic materials for biomedical applications*. Metallurgical and materials transactions A, 2002. **33**(3): p. 477.
123. Assad, M., et al., *Comparative in vitro biocompatibility of nickel - titanium, pure nickel, pure titanium, and stainless steel: genotoxicity and atomic absorption evaluation*. Bio-medical materials and engineering, 1999. **9**(1): p. 1-12.
124. DeZengotita, V.M., A.E. Schmelzer, and W.M. Miller, *Characterization of hybridoma cell responses to elevated pCO₂ and osmolality: intracellular pH, cell size, apoptosis, and metabolism*. Biotechnology and bioengineering, 2002. **77**(4): p. 369-380.
125. Halestrap, A., et al., *Mitochondria and cell death*. 2000, Portland Press Limited.
126. Rand, P.W., et al., *pH and blood viscosity*. Journal of applied physiology, 1968. **25**(5): p. 550-559.
127. Walker, J., et al., *The in vitro and in vivo evaluation of the biocompatibility of Mg alloys*. Biomedical Materials, 2013. **9**(1): p. 015006.
128. Clarkson, M.R., B.M. Brenner, and C. Magee, *Pocket Companion to Brenner and Rector's The Kidney E-Book*. 2010: Elsevier Health Sciences.
129. Ozturk, S.S. and B.O. Palsson, *Chemical decomposition of glutamine in cell culture media: effect of media type, pH, and serum concentration*. Biotechnology progress, 1990. **6**(2): p. 121-128.
130. Barão, V.A., et al., *Stability of cp - Ti and Ti - 6 Al - 4 V alloy for dental implants as a function of saliva pH - an electrochemical study*. Clinical oral implants research, 2012. **23**(9): p. 1055-1062.

131. Steinemann, S.G., *Titanium—the material of choice?* Periodontology 2000, 1998. **17**(1): p. 7-21.
132. Li, X., et al., *Novel bio-functional magnesium coating on porous Ti6Al4V orthopaedic implants: in vitro and in vivo study.* Scientific reports, 2017. **7**: p. 40755.
133. Ozturk, S.S. and B.O. Palsson, *Growth, metabolic, and antibody production kinetics of hybridoma cell culture: 2. Effects of serum concentration, dissolved oxygen concentration, and medium pH in a batch reactor.* Biotechnology progress, 1991. **7**(6): p. 481-494.
134. Jakoby, W.B. and I.H. Pastan, *Cell culture.* 1979: Academic Press New York:.
135. Herrmann, B.G. and A.-M. Frischauf, *Isolation of genomic DNA.* Methods Enzymol.;(United States), 1987. **152**.
136. Kapanen, A., et al., *Behaviour of nitinol in osteoblast-like ROS-17 cell cultures.* Biomaterials, 2002. **23**(3): p. 645-650.
137. Hansen, D.C., *Metal corrosion in the human body: the ultimate bio-corrosion scenario.* The Electrochemical Society Interface, 2008. **17**(2): p. 31.
138. Seah, K., et al., *A comparison between the corrosion behaviour of sintered and unsintered porous titanium.* Corrosion Science, 1995. **37**(9): p. 1333-1340.
139. Jüttner, K., *Electrochemical impedance spectroscopy (EIS) of corrosion processes on inhomogeneous surfaces.* Electrochimica Acta, 1990. **35**(10): p. 1501-1508.
140. Rybalka, K., L. Beketaeva, and A. Davydov, *Estimation of corrosion current by the analysis of polarization curves: Electrochemical kinetics mode.* Russian Journal of Electrochemistry, 2014. **50**(2): p. 108-113.
141. Mansfeld, F., *The polarization resistance technique for measuring corrosion currents, in Advances in corrosion science and technology.* 1976, Springer. p. 163-262.
142. Chang, J.C., et al., *Electrochemical study on microbiology - related corrosion of metallic dental materials.* Bio-medical materials and engineering, 2003. **13**(3): p. 281-295.
143. Revie, R.W., *Corrosion and corrosion control: an introduction to corrosion science and engineering.* 2008: John Wiley & Sons.
144. Tamilselvi, S., R. Murugaraj, and N. Rajendran, *Electrochemical impedance spectroscopic studies of titanium and its alloys in saline medium.* Materials and Corrosion, 2007. **58**(2): p. 113-120.
145. Dabrowski, B., et al., *Highly porous titanium scaffolds for orthopaedic applications.* Journal of Biomedical Materials Research Part B: Applied Biomaterials, 2010. **95**(1): p. 53-61.
146. Okazaki, Y., et al., *Corrosion resistance, mechanical properties, corrosion fatigue strength and cytocompatibility of new Ti alloys without Al and V.* Biomaterials, 1998. **19**(13): p. 1197-1215.

References

147. Oliveira, N. and A.C. Guastaldi, *Electrochemical stability and corrosion resistance of Ti–Mo alloys for biomedical applications*. Acta Biomaterialia, 2009. **5**(1): p. 399-405.
148. Dehghan-Manshadi, A., et al., *Porous titanium scaffolds fabricated by metal injection moulding for biomedical applications*. Materials, 2018. **11**(9): p. 1573.
149. Hong, T., T. Ogushi, and M. Nagumo, *The effect of chromium enrichment in the film formed by surface treatments on the corrosion resistance of type 430 stainless steel*. Corrosion Science, 1996. **38**(6): p. 881-888.
150. Bastos, I.N., et al., *Effect of microstructure on corrosion behavior of superduplex stainless steel at critical environment conditions*. Scripta Materialia, 2007. **57**(10): p. 913-916.
151. Jorcin, J.-B., et al., *CPE analysis by local electrochemical impedance spectroscopy*. Electrochimica Acta, 2006. **51**(8-9): p. 1473-1479.
152. Pan, J., D. Thierry, and C. Leygraf, *Electrochemical impedance spectroscopy study of the passive oxide film on titanium for implant application*. Electrochimica Acta, 1996. **41**(7-8): p. 1143-1153.
153. Kac, S. and J. Kusiński, *SEM and TEM microstructural investigation of high-speed tool steel after laser melting*. Materials Chemistry and Physics, 2003. **81**(2-3): p. 510-512.
154. Al-Bermani, S., et al., *The origin of microstructural diversity, texture, and mechanical properties in electron beam melted Ti-6Al-4V*. Metallurgical and materials transactions a, 2010. **41**(13): p. 3422-3434.
155. Hammond, C. and J. Nutting, *The physical metallurgy of superalloys and titanium alloys*. Metal science, 1977. **11**(10): p. 474-490.
156. Kusano, Y., et al. *Phase constitution and mechanical properties of Ti-(Cr, Mn)-Sn biomedical alloys*. in *Materials Science Forum*. 2010. Trans Tech Publ.
157. Raynor, G.V., *Progress in the theory of alloys*. Progress in metal physics, 1949. **1**: p. 1-76.
158. Ehtemam-Haghighi, S., et al., *Influence of Nb on the $\beta \rightarrow \alpha''$ martensitic phase transformation and properties of the newly designed Ti – Fe – Nb alloys*. Materials Science and Engineering: C, 2016. **60**: p. 503-510.
159. Zeng, L. and T. Bieler, *Effects of working, heat treatment, and aging on microstructural evolution and crystallographic texture of α , α' , α'' and β phases in Ti – 6Al – 4V wire*. Materials Science and Engineering: A, 2005. **392**(1-2): p. 403-414.
160. Ren, Y., et al., *Mechanical response and effects of β -to- α'' phase transformation on the strengthening of Ti–10 V–2 Fe–3 Al during one-dimensional shock loading*. Materials Science and Engineering: A, 2013. **562**: p. 137-143.
161. Nesmeyanov, A.N., *Vapor pressure of the chemical elements*. 1963.

162. Pontau, A.E. and D. Lazarus, *Diffusion of titanium and niobium in bcc Ti-Nb alloys*. Physical Review B, 1979. **19**(8): p. 4027.
163. Zhang, Y., H. Liu, and Z. Jin, *Thermodynamic assessment of the Nb-Ti system*. Calphad, 2001. **25**(2): p. 305-317.
164. Swamy, V., N. Dubrovinskaya, and L. Dubrovinsky, *High-temperature powder x-ray diffraction of yttria to melting point*. Journal of materials research, 1999. **14**(2): p. 456-459.
165. Pan, Y., et al., *Effects of Y₂O₃ on the microstructure and mechanical properties of spark plasma sintered fine-grained W-Ni-Mn alloy*. Journal of Rare Earths, 2017. **35**(11): p. 1149-1155.
166. Lee, Y. and G. Welsch, *Young's modulus and damping of Ti-6Al-4V alloy as a function of heat treatment and oxygen concentration*. Materials Science and Engineering: A, 1990. **128**(1): p. 77-89.
167. Zhou, Y.L., M. Niinomi, and T. Akahori, *Effects of Ta content on Young's modulus and tensile properties of binary Ti-Ta alloys for biomedical applications*. Materials Science and Engineering: A, 2004. **371**(1-2): p. 283-290.
168. Mack, D., *YOUNG'S MODULUS-ITS METALLURGICAL ASPECTS*. Transactions of the American Institute of Mining and Metallurgical Engineers, 1946. **166**: p. 68-84.
169. Hao, Y., et al., *Young's modulus and mechanical properties of Ti-29Nb-13Ta-4.6 Zr in relation to α'' martensite*. Metallurgical and Materials Transactions A, 2002. **33**(10): p. 3137-3144.
170. Afonso, C., et al., *Influence of cooling rate on microstructure of Ti-Nb alloy for orthopedic implants*. Materials Science and Engineering: C, 2007. **27**(4): p. 908-913.
171. You, L. and X. Song, *A study of low Young's modulus Ti-Nb-Zr alloys using d electrons alloy theory*. Scripta Materialia, 2012. **67**(1): p. 57-60.
172. Morinaga, M., et al. *Theoretical design of titanium alloys*. in *Sixth World Conference on Titanium. III*. 1988.
173. Zhou, Y.L., M. Niinomi, and T. Akahori. *Mechanical properties of binary Ti-Ta alloys for biomedical applications*. in *Materials Science Forum*. 2004. Trans Tech Publ.
174. Zhao, X., et al., *Beta type Ti-Mo alloys with changeable Young's modulus for spinal fixation applications*. Acta biomaterialia, 2012. **8**(5): p. 1990-1997.
175. Filip, R., et al., *The effect of microstructure on the mechanical properties of two-phase titanium alloys*. Journal of Materials Processing Technology, 2003. **133**(1-2): p. 84-89.
176. Kim, T.-H., et al., *The effects of heat treatments on the microstructure and mechanical properties of the Ti-2.19 Al-2.35 Zr alloy*. Nuclear Engineering and Design, 2008. **238**(6): p. 1286-1294.

References

177. Sha, W. and S. Malinov, *Titanium alloys: modelling of microstructure, properties and applications*. 2009: Elsevier.
178. Burgers, W., *On the process of transition of the cubic-body-centered modification into the hexagonal-close-packed modification of zirconium*. *Physica*, 1934. **1**(7-12): p. 561-586.
179. Lütjering, G., *Influence of processing on microstructure and mechanical properties of (α + β) titanium alloys*. *Materials Science and Engineering: A*, 1998. **243**(1-2): p. 32-45.
180. Paradkar, A., et al., *On the validity of Hall–Petch equation for single-phase β Ti–Al–Nb alloys undergoing stress-induced martensitic transformation*. *Materials Science and Engineering: A*, 2009. **520**(1-2): p. 168-173.
181. Dimiduk, D.M., et al., *The role of grain size and selected microstructural parameters in strengthening fully lamellar TiAl alloys*. *Metallurgical and Materials Transactions A*, 1998. **29**(1): p. 37-47.
182. Jung, J., et al., *Hall—petch relation in two-phase TiAl alloys*. *Materials Science and Engineering: A*, 1996. **220**(1-2): p. 185-190.
183. Hall, E., *The deformation and ageing of mild steel: III discussion of results*. *Proceedings of the Physical Society. Section B*, 1951. **64**(9): p. 747.
184. Van Swygenhoven, H., *Grain boundaries and dislocations*. *Science*, 2002. **296**(5565): p. 66-67.
185. Uebing, C., *On the ordering of interstitials in bcc metals and bct martensites: A lattice gas approach*. *Scripta metallurgica et materialia*, 1994. **30**(9): p. 1183-1188.
186. Frisk, K., *A revised thermodynamic description of the Ti–C system*. *Calphad*, 2003. **27**(4): p. 367-373.
187. Geng, F., M. Niinomi, and M. Nakai, *Observation of yielding and strain hardening in a titanium alloy having high oxygen content*. *Materials Science and Engineering: A*, 2011. **528**(16-17): p. 5435-5445.
188. Naka, S., et al., *The low-temperature plastic deformation of α -titanium and the core structure of a-type screw dislocations*. *Philosophical Magazine A*, 1988. **57**(5): p. 717-740.
189. Okamoto, H. and T. Massalski, *Guidelines for binary phase diagram assessment*. *Journal of phase equilibria*, 1993. **14**(3): p. 316-335.
190. Reed-Hill, R.E., R. Abbaschian, and R. Abbaschian, *Physical metallurgy principles*. 1973.
191. Hanic, F., et al., *Real structure of undoped Y2O3 single crystals*. *Acta Crystallographica Section B: Structural Science*, 1984. **40**(2): p. 76-82.
192. Oh, J.-M., et al., *Oxygen effects on the mechanical properties and lattice strain of Ti and Ti-6Al-4V*. *Metals and Materials International*, 2011. **17**(5): p. 733-736.

193. Limberg, W. and T. Ebel. *Metal Injection Moulding of Ti-6Al-4V with Yttrium addition*. in *Key Engineering Materials*. 2016. Trans Tech Publ.
194. Bruneel, N. and J.A. Helsen, *In vitro simulation of biocompatibility of Ti - Al - V*. Journal of biomedical materials research, 1988. **22**(3): p. 203-214.
195. Ratner, B.D., *A perspective on titanium biocompatibility*, in *Titanium in medicine*. 2001, Springer. p. 1-12.
196. Xie, K.Y., et al., *Nanocrystalline β -Ti alloy with high hardness, low Young's modulus and excellent in vitro biocompatibility for biomedical applications*. Materials Science and Engineering: C, 2013. **33**(6): p. 3530-3536.
197. Wu, L., et al., *Effects of extracellular magnesium extract on the proliferation and differentiation of human osteoblasts and osteoclasts in coculture*. Acta biomaterialia, 2015. **27**: p. 294-304.
198. Crossgrove, J. and W. Zheng, *Manganese toxicity upon overexposure*. NMR in Biomedicine: An International Journal Devoted to the Development and Application of Magnetic Resonance In Vivo, 2004. **17**(8): p. 544-553.
199. Kim, T.-I., et al., *New titanium alloys for biomaterials: a study of mechanical and corrosion properties and cytotoxicity*. Bio-medical materials and engineering, 1997. **7**(4): p. 253-263.
200. Hsu, R.W.-W., et al., *Electrochemical corrosion properties of Ti-6Al-4V implant alloy in the biological environment*. Materials Science and Engineering: A, 2004. **380**(1-2): p. 100-109.
201. Gonzalez, J. and J. Mirza-Rosca, *Study of the corrosion behavior of titanium and some of its alloys for biomedical and dental implant applications*. Journal of Electroanalytical Chemistry, 1999. **471**(2): p. 109-115.
202. Revie, R.W., *Uhlig's corrosion handbook*. Vol. 57. 2011: John Wiley & Sons.

Abbreviations

MIM	Metal injection moulding
FFF	Fused filament fabrication
at.%	Atomic ratio
wt.%	Weight ratio
h.c.p	Hexagonal close-packed
b.c.c	Body-centered cubic
Mo _{eq}	Molybdenum equivalent
Ti64	Ti-6Al-4V
TEM	Transmission electron microscopy
STEM	Scanning transmission electron microscopy
eV	Electron volt
L	Length
H	Height
W	Width
OM	Optical microscopes
SE	Secondary electrons
SEM	Scanning electron microscope
EPMA	Electron probe microanalysis
EDX	Energy dispersive X-ray spectroscopy
RUS	Resonant ultrasound spectroscopy
Fig.	Figure
ASTM	American Society for Testing and Materials
MPa	Megapascal
GPa	Gigapascal
UTS	Ultimate tensile strength
YS	Yield strength
HV	Vickers hardness
WQ	Water quench
Ar	Argon
C	Carbon
O	Oxygen
S	Sulfur

N	Nitrogen
Y	Yttrium
Ti	Titanium
Mn	Manganese
Nb	Niobium
Ag	Silver
TiC	Titanium carbide
Y ₂ O ₃	Yttrium oxide
e.g.	exempli gratia
etc.	etcetera
MG63	Human osteoblasts
Osmol	Osmolality
pH	Pouvoir Hydrogène
DMEM	Dulbecco's modified Eagle-medium Glut Amax-I
FBS	Foetal bovine serum
LDH	lactate dehydrogenase
DNA	Deoxyribonucleic acid
CE	Counter electrode
RE	Reference electrode
HBSS	Hanks' balanced salt solution
I _{corr}	Corrosion current
V	Volt
A	Ampere
OCP	Open-circuit potential
EIS	Electrochemical impedance spectroscopy
STDEV	Standard deviation
R _s	Resistance of solution
R _p	Resistance of polarization
CPE	Constant phase element

Acknowledgement

This research was fund by Xiamen University, China Scholarship Council and Helmholtz-Zentrum Geesthacht. Upon the completion of this thesis, I am grateful to those who have offered me encouragement and support during the course of my study.

First, I am grateful to Prof. Dr. Sabine Weiß and Prof .Dr. Florian Pyczak for being the reviewer of my thesis, also to Prof. Dr. Markus Bambach for being the chairman of my thesis defense and examination.

Secondly, a special acknowledgement is given to my respectable supervisors - Dr. Thomas Ebel, Prof. Dr. Florian Pyczak, Prof. Dr. Xingjun Liu, and Prof. Dr. Cuiping Wang. The patient instruction and constructive suggestions are beneficial to me a lot. During the preparation of the doctoral thesis, I have received a lot of invaluable help from many people –Peng Xu, Anke Schuster, Dr. Carsten Blawert, Dr. Pei Wang, Wolfgang Limberg, Dr. Frank Feyerabend and my colleagues. Their comments and advice contribute to the accomplishment of the thesis. I also want to thank all the authors whose books and articles have inspired me in the entire process of finishing the thesis.

Finally, I want to express my heartfelt thanks to mother Yanling Li, father Shaoliang Zhang, My parents in law Juying Huang and Bingda Wang. My wife Xiaoyu Wang is also most important for me. My lovely daughter Cynthia Zhang, she is an angel for me. I also want to thank all family members. It is your help that encourages me. I can't make this without your support. I love all of you. Meanwhile, my tributes to my friends (Lei Zhang, Fei Wang, etc.) wherever you are.